

Master Thesis

Transparent Glass Fiber-Reinforced Polymers and Their Applications

Chek Hei Vincenzo Man

Master Thesis

Transparent Glass Fiber-Reinforced Polymers and Their Applications

by

Chek Hei Vincenzo Man

to obtain the degree of Master of Science
at the Delft University of Technology,
to be defended publicly on Wednesday November 27, 2024 at 13:00.

Student number:	4810015	
Project duration:	February 26, 2024 – November 27, 2024	
Supervisors:	Dr. B. (Baris) Caglar, Dr. O. (Onur) Yüksel,	Responsible Daily
Thesis committee:	Dr. B. (Baris) Caglar, Dr. O.K. (Otto) Bergsma, Ir. P.P. (Prem) Sundaramoorthy,	TU Delft, Supervisor TU Delft, Chair TU Delft, External

An electronic version of this thesis is available at <http://repository.tudelft.nl/>.



Preface

To assess my experience with this thesis, I will briefly recap how this topic came to be. Since my bachelor's degree at TU Eindhoven was mostly online due to COVID-19, I always felt that I lacked the experimental and practical experiences. When I came to TU Delft to pursue a master's degree, one of the courses I enjoyed the most was Trinity, where I learned about the basics of fabrication and testing of composite materials. In the second year of my master's, I made it a goal to discover what I would like to pursue in the future, as I am a firm believer in trying out different things to see what you enjoy.

Therefore, I decided to choose an internship focused primarily on simulations, and for my thesis, I selected an experimental topic. My search for experimental topics led me to transparent glass fiber-reinforced polymers under the supervision of Dr. Baris Caglar. After a short but very enjoyable meeting, I was immediately convinced of the topic. Shortly afterward, I met my daily supervisor, Dr. Onur Yüksel, and we conducted our first experiment, which did not go as planned but was enjoyable nonetheless.

My experience working on this master's thesis was the best I could have hoped for. I gained extensive knowledge, not only about the thesis topic itself, which involved composite manufacturing, testing, and visualization techniques, but also valuable experience in project management, such as planning, managing material logistics, ensuring equipment availability, and finding the right people for training or access to specific tools.

While it took me quite some time to get the manufacturing parameters right, I was fortunate to receive a lot of help and advice from others working in the labs. Now that the thesis is finished, I can safely say it was a challenging but enjoyable journey. I met great people and gained deeper knowledge in the field. Overall, I am incredibly proud of the work, and it feels like a fitting conclusion to my master's degree.

I would like to take this opportunity to thank several people. First, my parents, who raised me and left their country to provide me with opportunities they never had. My friends from Nijmegen and the Randstad, who always kept in touch to make sure I was doing well, encouraged me to have fun, and pushed me to step out of my comfort zone during my student life. My friends from Eindhoven and Delft, who shared many late-night library sessions with me and helped me through the most difficult assignments. A special thank you to Joost Pieters, because without him, I would not have considered moving from Eindhoven to Delft to pursue my master's degree.

I would also like to thank my supervisor, Baris Caglar, for the opportunity to work on this thesis topic, for the interesting yet fun discussions, the valuable feedback during meetings, and for integrating me into the research group. I would also like to thank everyone in the research group who always made me feel welcome by asking about my project, offering help, and inviting me to social gatherings.

Lastly, I want to express my deepest appreciation to my daily supervisor, Dr. Onur Yüksel, who always made time in his busy schedule to provide incredible support. He gave me indispensable knowledge, skills, and feedback to successfully complete this thesis. Experiments that took hours felt like spending time with a good friend. I will definitely miss the fun conversations we had in the lab about games, food, and life. I wish you all the best in the future!

Abstract

Stiff and transparent materials are essential across industries such as aerospace, defense, and consumer electronics. Traditional materials like glass and ceramics, while effective, have limitations due to brittleness, high density, and low impact resistance. Consequently, there is a demand for lightweight, durable materials with favorable optical properties. Fiber-reinforced polymers (FRPs) offer high strength-to-weight ratios and greater impact resistance than glass and ceramics. Given the low light absorption of glass fibers in the visible spectrum, transparent glass fiber-reinforced polymers (TGFRPs) show promise as replacements for traditional transparent materials.

This thesis explores two main aspects: (1) optimizing TGFRP transparency through manufacturing parameters and (2) leveraging TGFRP transparency for damage detection and stress analysis. In the first phase, findings demonstrate that achieving high surface smoothness and maximizing light transmission within the green spectrum (520–600 nm) are crucial for enhancing TGFRP transparency. This is best controlled via post-curing, a more stable approach than adding methyl methacrylate (MMA) as suggested in existing literature. Sizing was also found to play a critical role in transparency, ensuring optimal bonding between glass fibers and the matrix. Additionally, minimizing the number of glass fiber fabric layers improved transparency by reducing transmission losses across visible wavelengths.

The second phase investigated the transparency of TGFRP for visualizing internal damage and stress distributions. Confocal microscopy was used to observe cracks at various depths within TGFRP samples, while image processing techniques, such as thresholding, were employed to calculate crack density. The results indicate that a higher crack density corresponds to reduced light transmittance across the visible range. However, some limitations were encountered, as cracks and scratches on the upper layers cast shadows on the lower layers, complicating the detection of deeper damage.

During tensile testing of open-hole specimens, significant opacity changes were observed in high-strain regions, suggesting that opacity correlates with localized stress. Digital image correlation (DIC) and grayscale histogram analysis provided insights into the strain thresholds at which opacity changes begin. Future work could build on this by examining the extent to which opacity changes are due to refractive index variations alone, independent of crack formation, using these strain levels as a baseline.

Furthermore, verifying the reversibility of opacity changes through post-test spectrophotometry could position TGFRPs as highly effective materials for developing innovative and reliable non-destructive testing, damage detection, and stress visualization methods in glass fiber-reinforced polymer composites.

Contents

Preface	i
Abstract	iv
List of Figures	vii
List of Tables	x
List of Abbreviations	xi
1 Introduction	1
1.1 Composite materials	1
1.2 Glass fiber-reinforced composites	1
1.3 Key to achieving transparency	2
1.4 TGFRPs and damage detection.	2
1.5 Project goals and report outline	3
2 Literature Review	5
2.1 Fiber-reinforced polymers	5
2.2 Matrix materials	6
2.3 Fiber materials	7
2.4 Transparency	8
2.5 Fabrication processes	14
2.5.1 Bag molding	14
2.5.2 Compression molding	14
2.5.3 Liquid molding processes	14
2.6 TGFRPs in damage detection	16
2.7 Potential applications	16
3 Problem Statement	19
4 Materials and Methodology	21
4.1 Materials	21
4.1.1 Glass fiber material	21
4.1.2 Resin	22
4.1.3 Methyl methacrylate	22
4.2 Vacuum infusion process	22
4.3 Sample preparation	23
4.3.1 Composite cutting machine	23
4.3.2 Tapping materials	23
4.4 Measurement equipment and techniques	24
4.4.1 Refractive index measurement	24
4.4.2 Transmission measurement	24
4.4.3 Confocal microscope	24
4.5 Mechanical testing	24

4.5.1	Testing machine and specimen dimensions	24
4.5.2	Digital image correlation	24
4.5.3	Photoelasticity setup	25
5	Results and Discussion: Manufacturing and Parameter Studies	27
5.1	Vacuum infusion	27
5.2	The influence of MMA on the refractive index and light transmission of GFRPs	30
5.3	Spectrophotometer measurements: pure resin samples	31
5.4	Spectrophotometer measurements: TGFRP samples	32
5.5	Spectrophotometer measurements: varying layers	34
5.6	Spectrophotometer measurements: varying resin batches	37
5.7	Spectrophotometer measurements: post-curing	38
5.8	Sizing experiment	40
5.9	Initial microscopy result	43
6	Results and Discussion: Applications of TGFRPs in Damage and Stress Analysis	45
6.1	Mechanical testing	45
6.2	Cracks in TGFRP specimens from tensile testing	48
6.2.1	Through-thickness microscopy measurement	49
6.2.2	Crack density determination	52
6.3	Opacity change	56
6.3.1	TGFRP sample	56
6.3.2	Photoelasticity	59
6.3.3	Reversibility of transparency	61
6.3.4	Pure resin samples	62
7	Conclusions	65
7.1	Answers to sub-questions	65
7.2	Conclusion to the main research question	68
8	Recommendations for Future Work	69
	References	71
A	Modified Vacuum Infusion Process	73
A.1	Materials and equipment	73
A.2	Vacuum assisted resin transfer molding (VARTM) process	74
B	Abbe Refractometer Sample Preparation and Measurement	79
B.1	Sample preparation	80
B.2	Measurement	80
C	Tensile Testing Preparations	82
C.1	Materials and equipment	82
D	All Transmission Data	85
D.1	Transmission data - varying MMA percentages by weight (pure resin samples)	85
D.2	Transmission data - varying MMA percentages by weight (TGFRP samples)	87
D.3	Transmission data - layers	89
D.4	Transmission data - post-curing	90
D.5	Transmission data - crack density	92

List of Figures

2.1	Types of fibers (Campbell, 2003).	6
2.2	Types of matrices: thermoset vs. thermoplastic (Villegas, 2022).	7
2.3	Properties of different fiber materials (Osorio, Trujillo, Vuure, & Verpoest, 2011).	8
2.4	Refraction of light through two mediums (Snell’s law).	9
2.5	Visible light spectrum, colors, and associated wavelengths (Ailioaie & Litscher, 2020).	10
2.6	Colorful fringe pattern of transparent safety glasses between two polarizer filters.	12
2.7	Sources leading to loss of transparency (Caydamli et al., 2021).	12
2.8	Surface defects (Zobeiry, Lee, & Mobuchon, 2020): (a) orange peel, (b) print-through at inter-tow regions, and (c) surface micro-cracks.	13
2.9	Overview of resin transfer molding (RTM) (Villegas, 2022).	15
2.10	Overview of vacuum infusion process (VIP) (Villegas, 2022).	15
4.1	Schematic of 8-harness satin weave glass fiber fabric (Hosur, Jeelani, Vaidya, Wosu, & Kelkar, 2003).	21
4.2	Modified vacuum infusion process for fabricating TGFRPs.	23
4.3	Top view of the mechanical testing setup for DIC and photoelasticity.	25
5.1	Influence of the mold’s surface quality on the transparency of the TGFRP panels.	27
5.2	TGFRP panel produced using the modified VIP with resin from R&G.	28
5.3	Average light transmission results for pure resin and TGFRP samples.	29
5.4	Pure resin vs. TGFRP sample directly on top of the TU Delft logo.	29
5.5	Pure resin sample (left) vs. TGFRP sample (right) at a distance from the TU Delft logo.	30
5.6	Manufactured GFRP panels with varying weight percentages of MMA. From left to right: 10% MMA, 7.5% MMA, and 0% MMA.	31
5.7	Average light transmission results for pure resin samples with varying MMA percentages in weight.	32
5.8	Average light transmission results for GFRP samples with varying wt% of MMA.	33
5.9	Transparency of the TGFRP samples directly on top of the TU Delft Logo. From left to right: 0% MMA, 0.5% MMA, 1.0% MMA, 2.5% MMA.	34
5.10	Transparency of the TGFRP samples at a distance from a sheet of text. From left to right: 0% MMA, 0.5% MMA, 1.0% MMA, 2.5% MMA.	34
5.11	Average light transmission results for GFRP samples with varying glass fiber fabric layers.	35
5.12	Transparency of the TGFRP samples directly on top of the TU Delft logo. From left to right: 5 layers, 10 layers, and 15 layers of glass fiber fabric.	36
5.13	Transparency of the TGFRP samples at a distance from a sheet of text. From left to right: 5 layers, 10 layers, and 15 layers of glass fiber fabric.	36
5.14	Average light transmission results for TGFRP samples made from different resin and hardener batches.	37
5.15	TGFRP samples: non-post-cured vs post-cured samples directly on top of the TU Delft logo. From left to right: non-post-cured, post-cured at 40°C, and post-cured at 60°C for 24 hours.	38

5.16	TGFRP samples: non-post-cured vs post-cured samples at a distance from a sheet of text. From left to right: non-post-cured, post-cured at 40°C, and post-cured at 60°C for 24 hours. The images were taken at a distance from the TU Delft logo.	38
5.17	Average transmission curve for TGFRP samples under varying post-curing conditions.	39
5.18	TGFRP panel produced using glass fiber fabric after sizing removal by burn-off.	40
5.19	Pure resin sample (left) vs post-cured resin sample (right).	41
5.20	Microscopy images of defects in the TGFRP sample (sizing removed).	41
5.21	Microscopy images of the embedded TGFRP sample (with sizing).	42
5.22	Microscopy images of the embedded TGFRP sample (sizing removed).	42
5.23	Microscopy results of the TGFRP sample showing different failure modes.	43
6.1	TGFRP specimens after failure in tensile testing with various end tabbing materials.	45
6.2	Stress vs. strain curve of the TGFRP specimens during tensile testing.	46
6.3	TGFRP specimens after tensile testing.	46
6.4	(a) Stress vs. strain curve of specimen 16, (b) Opacity change of specimen 16 at different points in the stress vs. strain response.	47
6.5	Microscopy results of cracks within the TGFRP sample after loading.	48
6.6	(a) Images at varying focal distances between the lens and the top surface of the TGFRP specimen, (b) Images at varying focal distances between the lens and the bottom surface of the TGFRP specimen.	50
6.7	Microscope image comparison: first image of the top surface vs. last image of the bottom surface.	51
6.8	Microscope image comparison between the top surface and the underlying layer.	51
6.9	Light transmission curves for samples with different loading conditions.	52
6.10	Flow chart for crack density determination.	53
6.11	Image processing for crack detection: cleaned binary image overlaid on the original image.	54
6.12	Limitations of thresholding due to dark imprints on the top surface of the sample.	55
6.13	(a) Load versus displacement curve for open-hole specimen 9 during tensile testing, (b) Opacity changes in open-hole specimen 9 at different points along the load versus displacement curve.	56
6.14	Opacity change of open-hole specimen 9 during loading compared to the strain pattern obtained from DIC at t=34 s.	57
6.15	Grayscale histogram of open-hole specimen 9 under loading at different time intervals (t=0 s, t=40 s, and t=80 s).	58
6.16	Grayscale histogram of open-hole specimen 9 under loading at different time intervals (t=10 s up to t=18 s).	58
6.17	Opacity change, DIC strain pattern, and photoelastic fringe pattern comparison.	60
6.18	Photoelasticity images of the TGFRP sample under testing.	60
6.19	Tensile testing of the open-hole specimen up to 6 kN (before failure).	61
6.20	Microscopy images of the open-hole specimen after loading to 6 kN (before failure).	62
6.21	Microscopy images of the open-hole specimen after loading up to 6 kN (before failure), showing the region between the top and bottom surfaces.	62
6.22	DIC images of pure resin sample 2 captured during loading at different time intervals.	63
6.23	Grayscale histogram of open-hole resin specimen 2 under loading at different time intervals (t=0 s, t=30 s, and t=60 s).	63
6.24	Photoelasticity images comparing the pure resin sample to the TGFRP sample.	64
A.1	Phase 2 assembly.	74
A.2	Inlet tube assembly.	75
A.3	Assembly with the outlet tube.	75
A.4	Perforate flow mesh and peel ply covering the assembly.	76
A.5	Phase 4 assembly	76

A.6	Preparation of the inlet tube.	77
A.7	Bucket assembly.	78
B.1	Zeiss Abbe refractometer	79
B.2	Abbe refractometer sample requirements.	80
C.1	Tensile test samples with tape and pattern before sanding.	83
C.2	Aluminum tabs secured to the test sample using blue adhesive tape.	83
C.3	Adhesive application on the tabbing material and the specimen.	84
C.4	Clamped specimens with aluminum tabbing material.	84
D.1	Light transmittance curves for all 20 specimens with 0% MMA by weight.	85
D.2	Light transmittance curves for all 20 samples with 1% MMA by weight.	86
D.3	Light transmittance curves for all 20 samples with 2.5% MMA by weight.	86
D.4	Light transmittance curves for all 38 samples with 0% MMA by weight	87
D.5	Light transmittance curves for all 40 samples with 0.5% MMA by weight	87
D.6	Light transmittance curves for all 40 samples with 1% MMA by weight	88
D.7	Light transmittance curves for all 36 samples with 2.5% MMA by weight	88
D.8	Light transmittance curves for all 38 samples with 5 layers of glass fiber fabric.	89
D.9	Light transmittance curves for all 40 samples with 10 layers of glass fiber fabric.	89
D.10	Light transmittance curves for all 40 samples with 15 layers of glass fiber fabric.	90
D.11	Light transmittance curves for all 38 samples with no post-curing.	90
D.12	Light transmittance curves for all 24 samples with post-curing at 40°C.	91
D.13	Light transmittance curves for all 24 samples with post-curing at 60°C.	91
D.14	Light transmittance curves for all 12 samples tensile tested at 60% of the ultimate tensile strength.	92
D.15	Light transmittance curves for all 12 samples tensile tested at 70% of the ultimate tensile strength.	92
D.16	Light transmittance curves for all 12 samples tensile tested at 80% of the ultimate tensile strength.	93

List of Tables

2.1	RI of woven glass fiber fabrics (0/90) in the literature.	11
2.2	Defects in FRPs and their examples.	12
4.1	Hexforce 7581 glass fiber fabric properties.	21
4.2	Refractive indices of resins used in other papers fabricating transparent glass fiber-reinforced composites.	22
4.3	Tabbing materials.	24
5.1	Average measured RI for pure resin samples with different wt% MMA.	30
5.2	Transmission data for different MMA percentages (TGFRP).	33
5.3	Transmission data for TGFRP with varying layers.	35
5.4	Transmission data for TGFRP samples from different batches of resin and hardener.	37
5.5	Transmission data for TGFRP samples at different post-curing temperatures.	39
6.1	Tensile test data for TGFRP specimens.	46
6.2	Transmission data for TGFRP samples subjected to different loading conditions.	52
6.3	Calculated crack density per specimen under different maximum loading conditions.	54
6.4	Calculated strain at which the opacity change initiates.	59
B.1	Contact liquids and their respective refractive indices at 20°C.	81

List of Abbreviations

Abbreviation	Designation
DIC	Digital Image Correlation
FRP	Fiber-Reinforced Polymer
FVF	Fiber Volume Fraction
GFRP	Glass Fiber-Reinforced Polymer
LCD	Liquid Crystal Display
LMP	Liquid Molding Processes
MAT	Maximum Average Transmittance
MMA	Methyl Methacrylate
PAR	Photosynthetically Active Radiation
PDMS	Polydimethylsiloxaan
RI	Refractive Index
RTM	Resin Transfer Molding
TGFRP	Transparent Glass Fiber-Reinforced Polymer
VARTM	Vacuum Assisted Resin Transfer Molding
VIP	Vacuum Infusion Process

Chapter 1

Introduction

Stiff and transparent materials are widely used across various industries. Silica-based glass, known for its chemical inertness, hardness, and low cost, is commonly used in windows and panels. High-performance transparent ceramics are also crucial in the military, aerospace, and medical fields. With the growing demand for portable technologies, the need for durable and transparent materials is expected to increase further (Menta, Vuppalapati, Chandrashekhara, & Schuman, 2014; Zobeiry et al., 2020).

However, both glass and ceramics are brittle, prone to shattering, and have limitations such as low impact resistance, poor formability, and high density (Magrini, Bouville, & Studart, 2021). As a result, there is a strong demand for lighter, stronger materials with good optical properties to replace them (Menta et al., 2014).

1.1 Composite materials

Composite materials are defined as a combination of multiple materials that offer greater mechanical properties compared to the use of individual materials alone. In particular, fiber-reinforced polymers (FRPs) consist of two main components: fibers and a polymer matrix. The fibers provide the majority of the mechanical strength, while the matrix binds them, distributes loads, and offers protection (Campbell, 2003).

FRPs exhibit high specific properties, such as strength and stiffness, and are often used in applications where high mechanical performance is required, and weight is a critical constraint (Krug, Asuncion, Popova, & Laine, 2013). Beyond mechanical strength, the high customizability and adaptability of composite materials allow for a wide range of choices in ply numbers, orientations, and their placement within the composite. Part integration is another significant advantage of FRPs, as it reduces manufacturing steps, leading to fewer parts and decreased weight in the structure (Campbell, 2003).

Moreover, FRPs provide significantly higher impact resistance compared to glass and ceramics. Under impact loads, FRPs can dissipate a much larger quantity of impact energy due to their multi-scale structure and the occurrence of various failure modes, such as delamination, fiber failure, microcrack formation, and fiber debonding. The incorporation of fibers into the matrix also helps redistribute stresses, limiting the growth of microcracks and splits in the matrix (Zobeiry et al., 2020; Yang et al., 2024).

1.2 Glass fiber-reinforced composites

For FRPs, various materials can be used for the fibers, such as carbon, glass, and aramid. Glass fibers offer a good balance between cost and mechanical strength, making them one of the most

frequently used fiber materials in engineering applications. Additionally, their low thermal expansion and conductivity, high-temperature durability and stability, chemical inertness, and high strength-to-weight ratio make them highly desirable materials (Villegas, 2022; Mallick, 2017). In the field of transparent materials, a key characteristic of interest is their low light absorbance in the visible spectrum compared to other fiber materials. This property makes glass fibers suitable candidates for use as reinforcement materials in transparent fiber-reinforced polymers (Yang et al., 2024).

1.3 Key to achieving transparency

In addition to selecting the right materials, research has shown that the transparency of transparent glass fiber-reinforced polymers (TGFRPs) can be enhanced by matching the refractive indices of the epoxy resin and glass fibers. The refractive index (RI) is a dimensionless number that describes how much light is bent as it passes through a material. Studies have found that adding certain monomers can effectively alter the RI of organic materials (Zobeiry et al., 2020; Caydamli et al., 2021).

Since the RI of epoxy resin is typically higher than that of glass fibers, the monomer methyl methacrylate (MMA) is often used to reduce the epoxy resin's RI to better match that of the glass fibers. While it is impossible to match the refractive indices of both materials across all wavelengths, many studies agree that it is crucial to match the RI in the green light spectrum, ranging from about 520 to 600 nm (Yang et al., 2024; Caydamli et al., 2021; Krug et al., 2013).

However, the RI can also vary with temperature, degree of cure, light wavelength, and moisture content. Additionally, the sizing of the glass fibers can influence the resin infiltration quality and, consequently, affect transparency. Beyond matching RIs with MMA to achieve TGFRPs, these parameters have not been thoroughly explored in the literature (Caydamli et al., 2021).

Therefore, the first phase of this thesis will focus on modifying the manufacturing parameters to control the transparency of glass fiber-reinforced polymers (GFRPs). The effects of post-curing and the removal of sizing on transparency will also be investigated to expand the understanding of factors influencing the transparency of TGFRPs.

1.4 TGFRPs and damage detection.

In addition to the beneficial mechanical properties of FRPs and their potential to replace glass and ceramic materials in applications requiring transparency, another advantage could be improved damage detection in FRPs. Due to their complex, multilayered structure, damage can remain invisible and unnoticed until it reaches a critical point, potentially leading to unanticipated and catastrophic failure. While damage in FRPs can sometimes be seen on the surface, it typically initiates beneath the outer layers of the composite and propagates through the laminate (Chen et al., 2023).

Non-destructive damage detection techniques, such as ultrasonic testing, acoustic emission, eddy current testing, and C-scanning, are commonly used to identify damage beneath the surface. Although these methods are well-established, they are generally not easily applicable for on-site inspections or full-scale components. Additionally, they require skilled professionals, can be expensive, and are time-consuming (Wang, Zhong, Lee, Fancey, & Mi, 2020).

Thus, utilizing the transparency of TGFRPs to detect and visualize failure modes could be highly beneficial, as it allows for the visual inspection of damage beneath the surface. This approach could lead to the development of techniques that are potentially more reliable than current non-destructive testing methods for glass fiber-reinforced polymer composite structures. Therefore, the second phase of this project will focus on exploring the potential of TGFRPs for damage detection and stress analysis by leveraging their transparency.

1.5 Project goals and report outline

This project will be divided into two phases. The first phase will focus on modifying the manufacturing parameters of the commonly used vacuum infusion process (VIP) to control the transparency of GFRPs. During this phase, the influence of various parameters will be investigated, including the addition of MMA, the increase in layers of glass fiber fabric, and the effects of post-curing. Additionally, the effect of sizing removal on transparency will be explored to deepen the understanding of factors influencing the transparency of TGFRPs.

The second phase of the project will focus on the potential application of TGFRPs in damage detection and stress analysis. This will be achieved by utilizing the transparency of TGFRPs to detect interlayer damage with a confocal microscope and by correlating opacity changes in TGFRPs during tensile testing with the stress field observed through photoelasticity and the strain field measured using DIC during loading.

In summary, this thesis aims to address the following research question:

How can the transparency of glass fiber-reinforced polymers be controlled or optimized by modifying manufacturing parameters, and in what ways can this transparency aid in stress and failure analysis?

This report consists of eight chapters, outlined as follows:

In **Chapter 2: Literature Review**, the literature review is presented, forming the basis for this thesis. **Chapter 3: Problem Statement** outlines the problem, the main research questions, and the sub-questions that will be investigated in this thesis. **Chapter 4: Methodology** provides information on the materials, equipment, and methods used to obtain answers to these questions. **In Chapter 5: Results and Discussion – Manufacturing and Parameter Studies**, the outcomes of the experiments on manufacturing and parameters are presented and discussed. **Chapter 6: Results and Discussion – Applications** presents and discusses the outcomes of the experiments on the potential applications of TGFRPs in damage and stress analysis. The report concludes with **Chapter 7: Conclusions**, which summarizes the knowledge obtained from the experiments by answering the sub-questions and the main research question. Finally, recommendations for future research are provided in **Chapter 8: Recommendations for Future Work**.

Chapter 2

Literature Review

Stiff and transparent materials can be found in a wide variety of applications across different industries. Silica-based glass is commonly used for applications requiring stiffness and transparency, such as windows and panels with high transparency, owing to its favorable characteristics such as chemical inertness, hardness, resistance to scratches, and relatively low cost ([Menta et al., 2014](#); [Zobeiry et al., 2020](#)).

Transparent ceramic materials with high performance are also frequently utilized in the military, aerospace, and medical sectors ([Zobeiry et al., 2020](#)). With the increasing development of portable technologies such as smartphones, cameras, wearables, and virtual reality headsets, the demand for transparent materials is expected to increase even further.

However, both glass and ceramic materials are brittle in nature, meaning they shatter into numerous smaller pieces upon impact, potentially causing injuries ([Magrini et al., 2021](#)). Additional disadvantages such as low impact resistance, low formability, high density, and low repairability also exist. Therefore, lighter and stronger materials with good optical characteristics are highly desired as substitutes for these materials ([Menta et al., 2014](#)).

2.1 Fiber-reinforced polymers

Composite materials are categorized as a combination of multiple materials, which provide greater mechanical properties compared to the application of the individual materials themselves ([Campbell, 2003](#)). Fiber-reinforced polymers (FRPs) consist of two main components: fibers and a polymer matrix.

The fibers serve as the dominant contributors to the mechanical performance of the composite material, while the polymer matrix binds the fibers together, distributes the load, and protects them. For FRPs, various materials are used for the fibers, such as glass, carbon, and aramid. Additionally, different types of fibers exist, such as continuous and discontinuous fibers, as shown in [Figure 2.1](#) ([Campbell, 2003](#)).

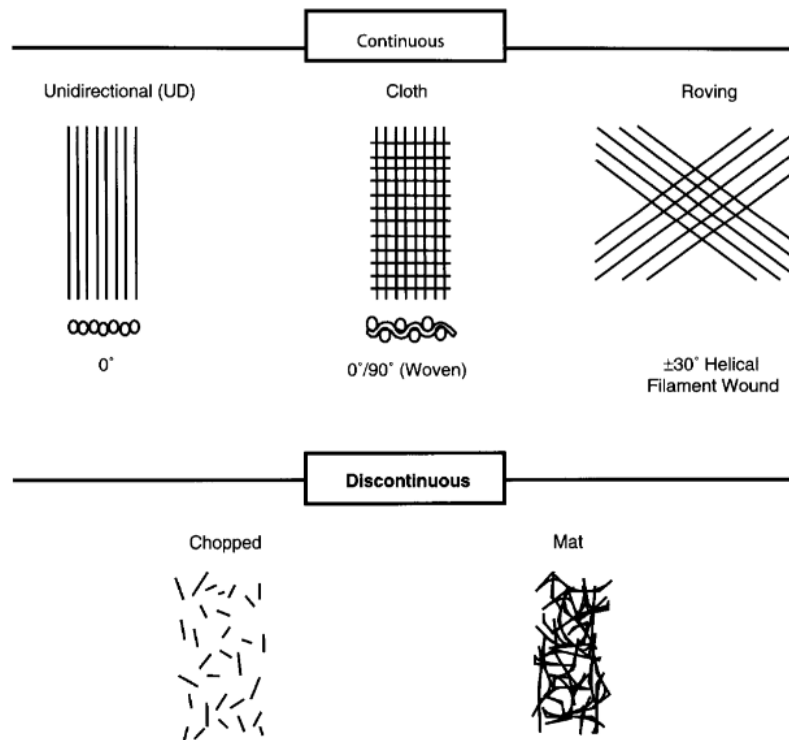


Figure 2.1: Types of fibers (Campbell, 2003).

FRPs provide high specific properties such as strength and stiffness and are often used in applications where high mechanical performance is required while weight is a critical constraint. For example, epoxy resin reinforced with glass fibers or carbon fibers can offer much higher mechanical properties compared to pure epoxy resin counterparts (Krug et al., 2013).

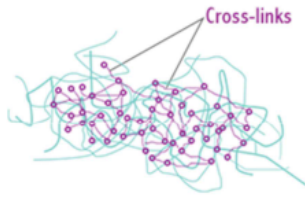
Aside from mechanical strength benefits, the high customizability/adaptability of composite materials allows for a broad selection of ply numbers, orientations, and their locations within the composite. Part integration is another significant advantage of FRPs. In production, complex parts made from metals usually require division into subassemblies, which are then assembled into the final part. FRPs can reduce manufacturing steps, leading to fewer parts and reduced weight in the structure, as fewer fastening materials, such as bolts, are required (Campbell, 2003).

Lastly, FRPs offer significantly higher impact resistance compared to glass and ceramics. Under impact loads, FRPs can dissipate a much larger quantity of impact energy due to their multi-scale nature and the occurrence of various failure modes, such as delamination, fiber failure, (micro)crack formation, and fiber debonding (Zobeiry et al., 2020). The incorporation of fibers into the matrix also helps redistribute stresses by limiting the growth of microcracks and splits in the matrix (Yang et al., 2024). Therefore, FRPs are often used in large load-bearing applications across the automotive, marine, aerospace, and construction industries.

2.2 Matrix materials

The matrix material in composites has the primary functions of protecting the fibers, distributing loads, offering interlaminar shear strength, and holding the fibers in position. Matrices for FRPs can be categorized into two types: thermoset and thermoplastic matrices, as illustrated in Figure 2.2 (Campbell, 2003).

Thermoset polymers



Chemical bonds (cross-links)
among polymer chains

Thermoplastic polymers



Physical bonds (van der
Waals, entanglements) among
polymer chains

Figure 2.2: Types of matrices: thermoset vs. thermoplastic (Villegas, 2022).

In the case of thermoset matrices, when the resin and hardener are mixed together, the low-viscosity mixture will cure either due to internally generated heat (an exothermic reaction) or heat applied from the external environment. Curing thermoset matrices results in long polymer chains interconnected by crosslinks (chemical bonds). This curing process is irreversible, meaning that the chemical bonds cannot be broken (Villegas, 2022; Campbell, 2003).

Thermoplastic matrices also consist of long polymer molecules, but they are not connected through chemical bonds. Instead, they are held together by van der Waals forces or entanglement (physical bonds). These high-viscosity materials do not crosslink upon heating. When the matrix is exposed to elevated temperatures, the physical bonds are released or weakened, causing the material to achieve a low-viscosity state, which can then be shaped into a different form. The physical bonds are restored upon cooling, and the material hardens again (Villegas, 2022; Campbell, 2003).

When choosing a resin from the thermoplastic or thermoset categories, the selection will affect not only the material properties but also the manufacturing process and cost. For example, thermoset composites generally involve slower and more expensive manufacturing processes compared to thermoplastic composites, as their reliance on chemical reactions makes them more time-consuming (Villegas, 2022; Campbell, 2003).

2.3 Fiber materials

Fibers are the primary component in FRPs responsible for providing mechanical properties, such as strength and stiffness. Various fiber materials are used for these purposes, including carbon, glass, aramid, and others. Among these, glass and carbon fibers are the most commonly used in engineering applications (Villegas, 2022; Campbell, 2003; Mallick, 2017).

The main differences between carbon and glass fibers are illustrated in Figure 2.3. From this table, it can be observed that carbon fibers have a higher elastic modulus and tensile strength, as well as a lower density compared to glass fibers. This means that carbon fibers are not only stronger and stiffer than glass fibers, but also lighter (Villegas, 2022).

Therefore, carbon fibers are often the preferred option in the aerospace industry. Other notable observations include the negative coefficient of thermal expansion for carbon fibers and the larger diameter of glass fibers, which could impact the manufacturing process (Campbell, 2003).

Fibre	Density (gr/cm ³)	Diameter (μm)	Elongation at failure (%)	Tensile strength (MPa)	E-Modulus (GPa)
Bagasse	–	490	–	70	–
Coir	1.2	–	30	175	4–6
Cotton	1.5–1.6	20	7.0–8.0	287–597	5–13
Curaua	1.38	66	3.9	913	30
Flax	1.5	50–100	2.7–3.2	345–1035	50–70
Hemp	1.10	120	1.6	389–900	35
Henequen	–	180	3.7–5.9	430–570	10–16
Jute	1.3	260	1.5–1.8	393–773	26
Kenaf	1.31	106	1.8	427–519	23–27
Pineapple	1.32	–	2.4	608–700	25–29
Ramie	1.50	34	3.6–3.8	400–938	24–32
Sisal	1.5	50–80	2.0–2.5	337–413	8–10
Bamboo	0.88–1.1	100–200	–	391–713	18–55
E-Glass	2.5	9–15	2.5	1200–1500	70
Carbon (PAN)	1.4	5–9	1.4–1.8	4000	230–240

Figure 2.3: Properties of different fiber materials (Osorio et al., 2011).

However, glass fibers provide a good balance between cost and mechanical strength and are, therefore, more frequently used in engineering applications compared to other fiber types. They are commonly found in the manufacturing of radomes, fairings, and wind turbine blades. In contrast, carbon fibers are significantly more brittle due to their lower elongation at failure compared to glass fibers (Villegas, 2022). Additionally, glass fibers offer excellent properties, such as (Mallick, 2017):

- Low thermal expansion and conductivity.
- High strength-to-weight ratio.
- High-temperature durability and stability.
- Chemical inertness.

One key optical characteristic of glass fibers is their low light absorbance in the visible spectrum compared to other types of fiber materials. This property makes them suitable candidates for use as reinforcement materials in transparent fiber-reinforced polymers (TFRPs) (Yang et al., 2024).

2.4 Transparency

The key to TGFRRPs lies in minimizing the loss in light transmittance. To achieve this, several requirements must be met: matching refractive indices (RI) between the materials, ensuring high resin-to-fiber infiltration, and achieving smooth surfaces (Zobeiry et al., 2020; Caydamli et al., 2021). Additionally, the loss of light transmission decreases with increasing fiber volume fraction. The fiber volume fractions in high-performance composite parts range between 50 to 65 percent (Mallick, 2017).

Refractive index

Refraction is the phenomenon where light bends due to a reduction in its speed when it passes from one medium to another. For example, when light shines through glass, the light beam appears to bend. It has also been observed that increasing the concentration of sugar in distilled water raises the RI of the medium (Mat Yunus & Rahman, 1988).

The RI is an optical property of materials that describes how light slows down or bends as it travels through the material. It is often used in the fields of chemistry and physics. A higher RI indicates that the material can bend light more effectively. Thus, the RI can be described by Equation 2.1.

$$n = \frac{c}{v} \quad (2.1)$$

Where:

- c = speed of light in vacuum [m/s]
- v = speed of light in medium [m/s]

Since the speed of light is highest in a vacuum, the RI is typically greater than 1. The RI is commonly measured at a wavelength of 589 nm, known as the sodium D-line, because of the availability, stability, and repeatability of this light source. Additionally, this wavelength is close to the middle of the visible light spectrum (400-700 nm), which is around 550 nm. The RI is usually expressed in a form that accounts for its dependency on temperature and wavelength as seen in [Equation 2.2](#).

$$N_D^t \quad (2.2)$$

Where:

- D = sodium D-line (wavelength of 589 nm)
- t = temperature at which the measurement is conducted [°C]

For example, the RI for monobromonaphthalene measured at 20°C at a wavelength of 589 nm is expressed as:

$$N_D^{20} = 1.63 \quad (2.3)$$

Up until now, the RI has been explained using the speed of light, but it can also be described using angles. Snell's Law describes the relationship between the angle of incidence and the angle of refraction, as shown in [Figure 2.4](#) and [Equation 2.4](#).

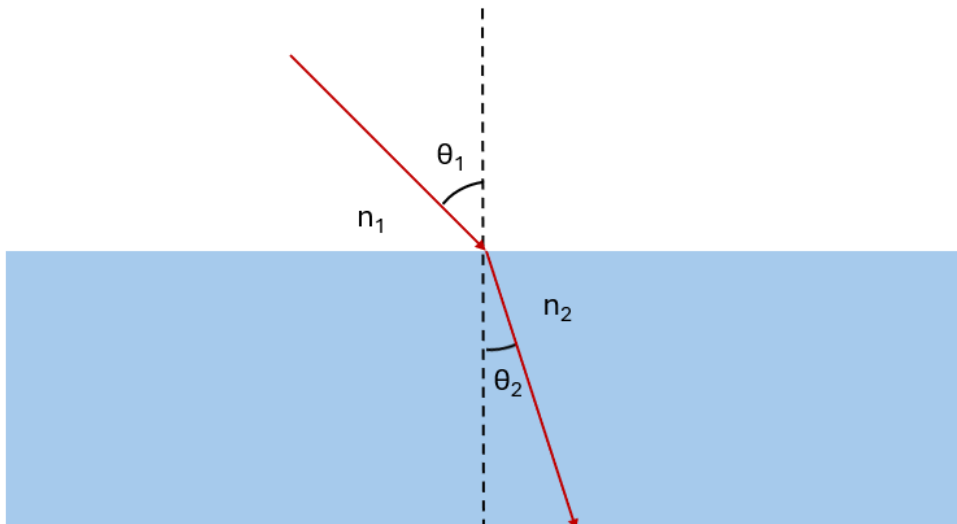


Figure 2.4: Refraction of light through two mediums (Snell's law).

$$n_1 \sin(\theta_1) = n_2 \sin(\theta_2) \quad (2.4)$$

Where:

- n_1 = refractive index of medium 1 [-]
- n_2 = refractive index of medium 2 [-]
- θ_1 = angle of incidence [deg]
- θ_2 = angle of refraction [deg]

The foundation for achieving high transparency in glass fiber-reinforced polymers (GFRPs) lies in matching the RI between the polymer matrix and the fiber reinforcements. The RI, a dimensionless number that describes the degree to which light is bent as it passes through a material, significantly influences the material’s light transmission (Yang et al., 2024). Furthermore, the RI can vary with temperature, degree of cure, wavelength of light, and moisture content. A large mismatch in RI can lead to chromatic aberration and haze in the material (Caydamli et al., 2021).

Light is electromagnetic radiation, and depending on its wavelength, it can be perceived as different colors, as shown in Figure 2.5. Light with longer wavelengths appears red, while shorter wavelengths are perceived as yellow, green, blue, and purple. The combination of all visible wavelengths forms white light. Chromatic aberration occurs when visible wavelengths are not refracted equally. For example, shorter wavelengths may be refracted more than longer wavelengths (Yang et al., 2024).

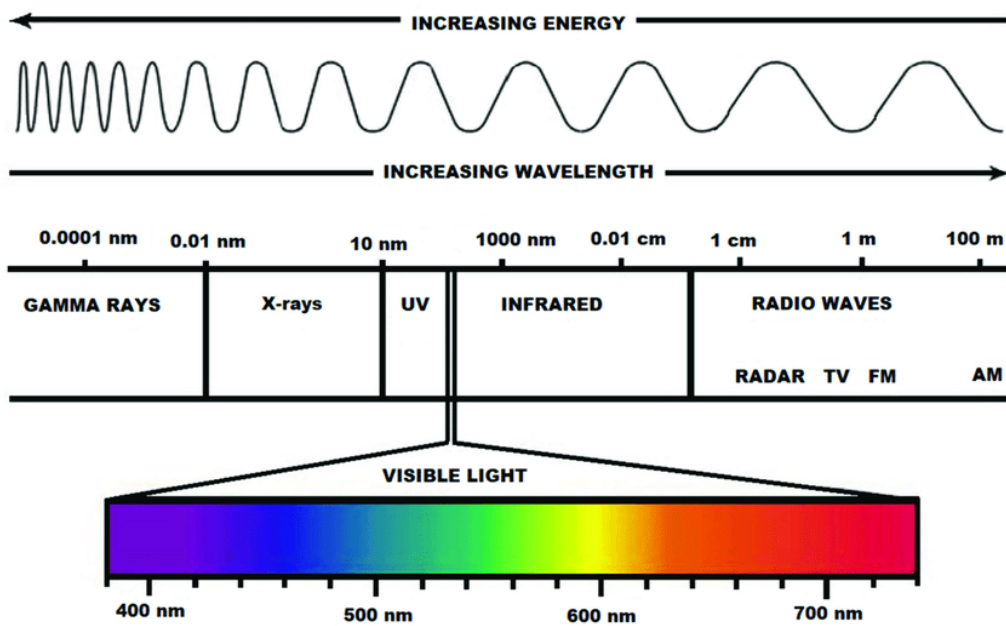


Figure 2.5: Visible light spectrum, colors, and associated wavelengths (Ailioaie & Litscher, 2020).

This results in white light being broken up into the visible spectrum. Instead of a sharp image, a less-defined image appears with coloration around the edges. Therefore, it can be concluded that the RI of the materials in the FRPs needs to closely match over the operating temperature range of the material and the visible light spectrum (Caydamli et al., 2021).

Several methods can be used to match the RI. Table 2.1 provides an overview of the RI of woven glass fiber fabrics from different manufacturers in the literature. The choices are to modify either the RI of the glass fibers or the RI of the polymer matrix. For example, annealing glass fibers has been shown to increase the RI (Menta et al., 2014). However, since the measurement of the RI of glass fibers can be a complicated process, the more straightforward and commonly applied method is to modify the RI of the polymer matrix (Yang et al., 2024).

Table 2.1: RIs of woven glass fiber fabrics (0/90) in the literature.

Glass fiber manufacturer	RI [-]
Guangzhou Yingu Building Materials	1.556 (Yang et al., 2024)
HexForce (TF970)	1.556 (Caydamli et al., 2021)
Hexcel (1522)	1.565 (Zobeiry et al., 2020)
Fibre Glast (S-glass)	1.525 (Krug et al., 2013)

When the RI of the glass fibers is predetermined or provided on the datasheet, the RI of the polymer matrix can be adjusted to match that of the glass fibers by introducing another material to the matrix, as the RI of both materials contribute to the final RI of the composite (Zobeiry et al., 2020). This additional material can be organic dopant molecules or inorganic nanoparticles. Studies have found that the addition of certain monomers can effectively alter the RI of organic materials.

Considering that the RI of epoxy resin is commonly larger than that of glass fibers, the monomer methyl methacrylate (MMA) can be dissolved into the resin matrix to reduce its RI (Zobeiry et al., 2020; Yang et al., 2024). As mentioned previously, due to multiple parameters being able to influence the RI and given the circular geometry of the fibers, it is only possible to match the RI of the fibers and the epoxy resin for a range of wavelengths and specific condition (temperature) (Zobeiry et al., 2020).

Therefore, many studies agree that it is crucial to match the RI in the green light spectrum, which is around 520-600 nm, instead of shorter wavelengths due to the natural light spectrum. Matching the RI at longer wavelengths could increase haze as well as lower the light transmittance (Yang et al., 2024; Caydamli et al., 2021; Krug et al., 2013).

Photoelasticity

Birefringence is an optical property in which double refraction occurs due to an incoming ray of light being split into two rays traveling at different speeds through the material. This effect arises from the material's anisotropy. Because of the difference in speeds, a phase difference is introduced between the two rays. When they recombine, they interfere with each other, creating either constructive interference, which amplifies certain wavelengths/colors, or destructive interference, which cancels out certain colors (Patterson, 2016).

This results in colorful patterns in birefringent materials when placed between polarizers, which are filters that only allow light of certain orientations to pass through, as shown in Figure 2.6. Polarizers further control the combination of the rays, enhancing the interference effect and making the fringe patterns more visible. In many materials, the fringe patterns change with the amount of stress applied to the material. Engineers have utilized these fringe patterns to assess stress distribution and detect issues such as cracks or regions of high strain within materials.

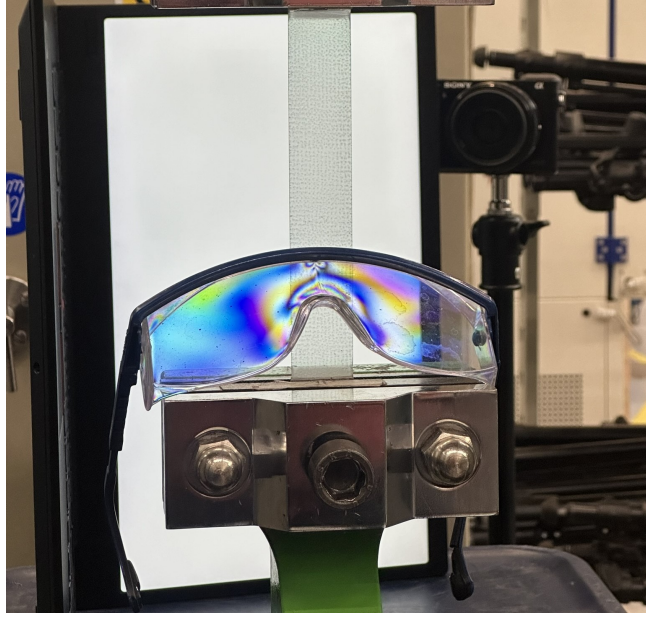


Figure 2.6: Colorful fringe pattern of transparent safety glasses between two polarizer filters.

Infiltration quality

The second key parameter for achieving high transparency in GFRPs is the quality of infiltration. Defects originating from materials (such as fabric and resin types), manufacturing methods, and parameters (such as temperature and pressure) can cause light scattering and reduce the transparency of transparent glass fiber-reinforced polymers (TGFRPs), as illustrated in Figure 2.7. These defects can be further categorized into matrix defects, fiber defects, interface defects, and surface defects. Examples of these defects are provided in Table 2.2 (Zobeiry et al., 2020; Yang et al., 2024; Caydamli et al., 2021).

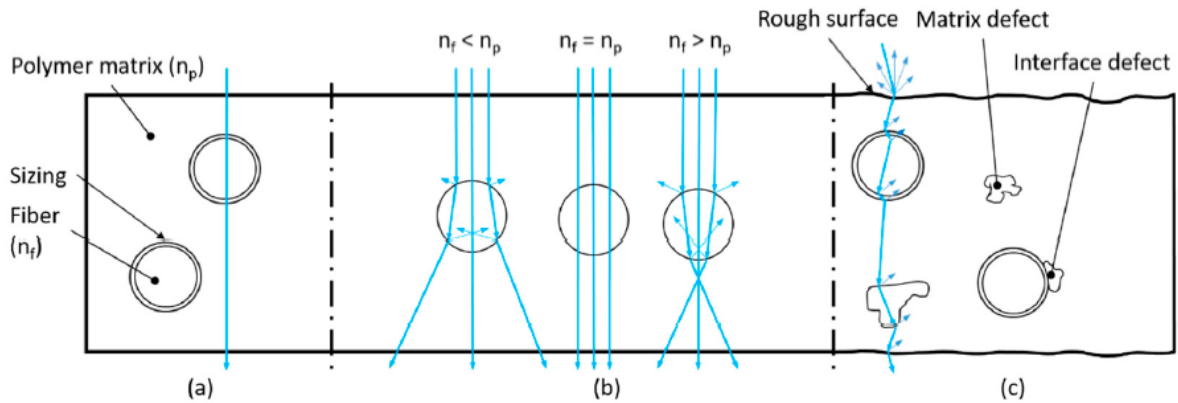


Figure 2.7: Sources leading to loss of transparency (Caydamli et al., 2021).

Table 2.2: Defects in FRPs and their examples.

Category of defect	Examples
Matrix	Incomplete infiltration of matrix into the fiber, voids/porosity, contamination/impurities
Fiber	Deviations in fiber orientation, waviness, fiber breakage, irregular fiber distribution
Interface	Unadhered regions, (micro)cracks, delamination
Surface	Orange peel, micro cracks, fiber print through, release agent residues, surface roughness

In addition, the fibers are usually coated with sizing or subjected to surface treatments to ensure proper wetting, which can affect the transparency of the material. Sizing is a mixture of chemicals with which the fibers are coated and consists of various components (Mallick, 2017):

- Lubricants: These prevent wear due to contact between the filaments.
- Anti-static agents: These reduce the static electricity between filaments.
- Binders: These combine the filaments into a strand and promote chemical bonding between the fiber and the polymer matrix. They also serve to protect the filaments against abrasion caused by rubbing against each other.

A PhD thesis at the Technical University of Denmark has demonstrated that a burnoff removal method at 565°C is more effective for removing a large part of the sizing on glass fibers compared to Soxhlet extraction using acetone (Petersen, 2017).

Surface quality

Finally, the surface quality of the TGFRP should be as smooth as possible, as surface roughness can lead to light scattering and reduced transparency (Caydamli et al., 2021). Print-through and orange peel are common defects observed with woven fabrics. Orange peel or dips can appear on the surface due to the shrinkage of the resin, while print-through occurs due to surface micro-cracks or partially uncovered fibers. These surface defects are illustrated in Figure 2.8 (Zobeiry et al., 2020). To minimize these surface defects, several methods can be applied to ensure smooth surfaces.

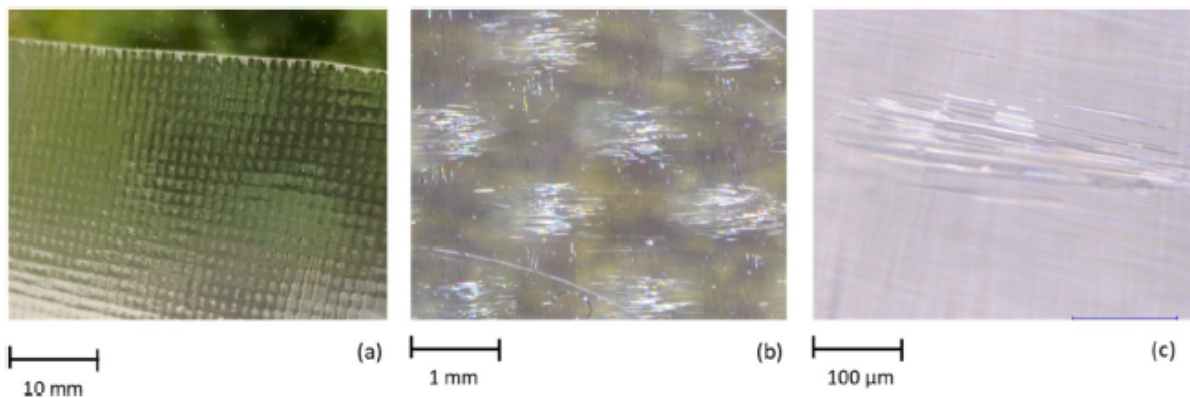


Figure 2.8: Surface defects (Zobeiry et al., 2020): (a) orange peel, (b) print-through at inter-tow regions, and (c) surface micro-cracks.

Firstly, high-quality molds with smooth surfaces can greatly improve surface flaws (Krug et al., 2013; Yang et al., 2024). Secondly, a resin-rich layer or clear coat can be introduced, which has been shown to decrease surface scattering and greatly enhance the optical clarity of the material (Magrini et al., 2021; Zobeiry et al., 2020). Lastly, the composite surface can be polished, and the addition of a refractive index matching layer, such as oil, can significantly reduce haze (Magrini et al., 2021).

2.5 Fabrication processes

Several fabrication processes can be used to fabricate FRPs, each with its own benefits and drawbacks. This chapter discusses these processes in more detail. The type of fabrication process depends on the number of parts, shape, and size of the part.

Depending on whether a thermoset or thermoplastic matrix is used, manufacturing processes and parameters will be different. For example, a thermoset matrix starts in a low viscosity form and cures to a solid due to internally generated heat or heat from the environment, while a thermoplastic matrix starts in a solid form and, with the addition of heat, transforms into a low viscosity liquid form.

2.5.1 Bag molding

A common process used in the fabrication of composite parts is bag molding, which allows for the production of parts with various fiber orientations, controllable fiber volume, and relatively low void content. This process involves the use of prepreg, a material that consists of fiber sheets pre-impregnated with a partly cured thermoset resin.

During the bag molding process, the cut prepreg sheets are placed on top of each other on a mold surface. A bag is then placed over the prepreg sheets and cured in either a press at a raised temperature or an autoclave. Vacuum is used to apply pressure, removing air, impurities/volatiles, and surplus resin from the prepreg sheets (Villegas, 2022; Mallick, 2017; Campbell, 2003).

2.5.2 Compression molding

In compression molding, uncured fiber-reinforced thermoset polymer sheets are placed between pre-heated molds. The top mold is then lowered down, which heats and compresses the material. Due to the compression and elevated temperature, the material spreads outward. Once the material has finished curing, the mold can be opened.

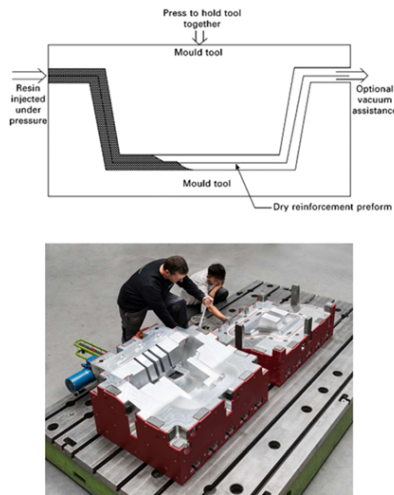
One drawback of this method is that the tooling cost of the molds is high, as they are subjected to high pressures to fill the mold. However, parts with complex shapes, details, and good surface finish can be produced at high production rates with this manufacturing method (Villegas, 2022; Mallick, 2017; Campbell, 2003).

2.5.3 Liquid molding processes

In liquid molding processes (LMP), the fiber reinforcements are placed in a mold. After closing the mold, the fibers are impregnated by injecting the matrix in a low-viscosity form. When the fibers are completely impregnated, the resin cures, usually at elevated temperatures (Campbell, 2003).

In LMP, one or multiple inlets and outlets are present, and a pressure differential is created between these to move the resin through the fiber reinforcement and impregnate them. Air inside the assembly is pushed out through the outlet. After the resin has cured, the part can be removed from the mold for further processing (Villegas, 2022).

LMP can be divided into two main categories: resin transfer molding (RTM) and vacuum infusion (VIP). In RTM, the main characteristics include the use of a rigid mold on both sides and the pressurization of the resin before injection into the mold. The pressurization of the liquid creates a pressure differential between the inlet and the outlet (atmospheric pressure), which drives the resin to move through and impregnate the fiber reinforcement, as shown in Figure 2.9 (Villegas, 2022; Campbell, 2003; Mallick, 2017).



RTM: Resin Transfer Moulding

2-sided rigid mould

$$P_{\text{inlet}} > 1\text{bar} / P_{\text{outlet}} = 1\text{bar}$$

$$P_{\text{outlet}} < 1\text{bar} \quad \text{VARTM}$$

Press required to close mould

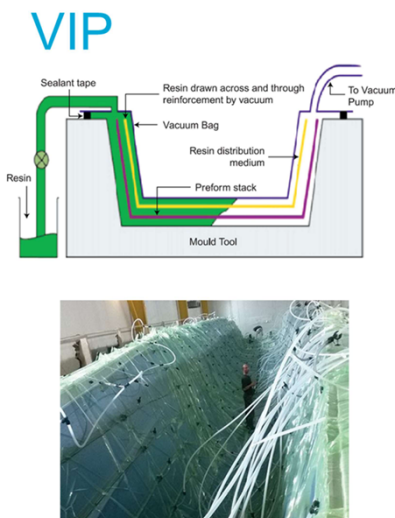
Small to medium-sized parts, high quality
 $V_f = 55\text{-}65\%$

Figure 2.9: Overview of resin transfer molding (RTM) (Villegas, 2022).

When the outlet is connected to a vacuum pump, it becomes vacuum-assisted RTM (VARTM), which creates a larger pressure differential compared to standard RTM. For these processes, a force in the form of clamps or a press is required to keep the mold closed during the impregnation and curing process because the injection pressure is higher than atmospheric pressure.

This process allows for the production of only small to medium-sized components; otherwise, the pressure required to close the molds would be too high. However, (VA)RTM is capable of producing parts with high surface quality and high fiber volume fractions (Villegas, 2022).

Another main process in LMP is VIP, which utilizes a one-sided rigid mold and a vacuum bag. Similar to the VARTM process, the outlet is connected to a vacuum pump. This creates a pressure differential with the inlet (atmospheric pressure), which forces the resin to flow from the inlet through the fibers and then to the outlet as shown in Figure 2.10 (Campbell, 2003; Villegas, 2022).



VIP: Vacuum infusion process

1-sided rigid mould + vacuum bag

$$P_{\text{inlet}} = 1\text{bar} / P_{\text{outlet}} < 1\text{bar}$$

Large parts

Normally used for wind turbine blades and boat hulls but finding its way into aerospace industry (VAP)

Figure 2.10: Overview of vacuum infusion process (VIP) (Villegas, 2022).

VIP is a suitable manufacturing process for large composite parts, as it requires only one rigid mold. In contrast, RTM involves two rigid molds, which are not only expensive to produce and heavy but also require significant force to keep the mold closed during the process, especially for large parts. Therefore, VIP can be considered a cost-efficient method for producing large composite parts.

However, VIP does have its drawbacks. Because the pressure differential is lower compared to RTM, impurities and volatiles might not be fully removed, which can result in higher void content in the composite. Additionally, since the other side uses a vacuum bag, inconsistent thickness and surface finish can occur compared to using rigid molds on both sides (Campbell, 2003; Villegas, 2022; Mallick, 2017).

2.6 TGFRPs in damage detection

In addition to the mechanical advantages of TGFRPs and their potential to replace glass and ceramics in transparent applications, they could offer significant benefits for damage detection. The multilayered structure of traditional FRPs can conceal internal damage, which might go unnoticed until it becomes critical, leading to sudden and catastrophic failure. Although surface damage may be visible in FRPs, damage typically initiates beneath the outer surface of the composite and propagates through the laminate (Chen et al., 2023).

Common non-destructive damage detection techniques include ultrasonic testing, acoustic emission, eddy current testing, and C-scanning. While these methods are well-established, they are often not easily applicable on-site or for full-scale components. Furthermore, they require skilled professionals, can be expensive, and are time-consuming (Wang et al., 2020).

Therefore, utilizing the transparency of TGFRPs to detect and visualize failure modes could be highly beneficial, as damage beneath the surface can be visually inspected and detected. This approach could potentially lead to new techniques that might be more reliable than current non-destructive testing methods for damage detection and visualization in GFRP composite structures.

2.7 Potential applications

Windshields and windows

Structural glass is commonly utilized in the building sector and automotive industry, where it can be found in various applications such as sliding doors, windshields, windows, and transparent roofs. Current strategies primarily focus on strengthening glass against impact or reducing the formation of smaller glass shards post failure (Magrini et al., 2021).

Two main categories of structural glass are commonly used: strengthened glass and laminated glass. Laminated glass contains a polymer interlayer between two annealed glass plates. Upon impact or failure, the glass shards remain attached to the interlayer, preventing them from coming loose and potentially causing injuries. Strengthened glass requires more impact energy to break and typically shatters into smaller, rounded glass pieces, which are less likely to cause injuries (Magrini et al., 2021). However, despite these strategies, the inherent brittleness of glass remains.

Therefore, the development of new transparent composite materials with high impact and fracture resistance could be highly beneficial in these markets. This is particularly relevant for fighter jets, where the canopy comprises a significant percentage of the frontal area of the aircraft. Given the high speeds and the potential for bird strikes, such materials are crucial to prevent substantial damage to both the plane and the pilot inside.

Portable displays

High haze in transparent composites results from their multi-scale nature, where light passing through the material spreads out due to the presence of defects in the visible light range (Magrini et al., 2021). While this may be considered a drawback in some cases, it can be advantageous for products in contact with a light source, such as portable device screens.

For example, liquid crystal displays (LCDs) are widely used in various technologies today, but they require a backlight since the liquid crystals cannot emit light themselves. A key component of the backlight is a diffuser, which serves several functions including light scattering, beam shaping, and ensuring uniform brightness.

In this way, the light from the source is evenly spread out, resulting in increased brightness. This application is primarily used in backlit displays and offers several benefits, including lower power consumption due to increased brightness without consuming extra power, as well as creating an anti-glare surface that improves visibility when viewed from different angles outdoors (Fang et al., 2014).

Light scattering films are commonly categorized into particle diffusing films or surface relief films. Particle diffusing films incorporate transparent beads within the material for light scattering, while surface relief films rely on microstructures on the material's surface. Various manufacturing techniques such as extrusion molding, electrospray methods, Polydimethylsiloxane (PDMS) replica molding, holographic recording, and 3D diffuser lithography have been developed. However, it is widely acknowledged that the manufacturing of light-scattering diffusers involves a complicated and expensive process (Huang, Ciou, Huang, Hsieh, & Yang, 2008).

For glass, surface relief methods such as dry/wet etching and sandblasting are available, which essentially roughen up the glass surface. However, these manufacturing methods could potentially damage, crack, or introduce defects to the surface. Therefore, leveraging the multi-scale nature of TFRPs to introduce haze without compromising the material could offer significant benefits in the production of portable displays.

Solar cell covers

A solar cell typically consists of several components, with a tempered cover glass primarily used to protect the solar cells from the environment. However, the density of glass and the industry standard thickness of 3-4 millimeters for the coverglass contribute significantly to the weight of the solar panel, often comprising more than half of its total weight (Reynolds, 2022). As the demand for thinner, lighter, and more efficient solar panels grows, transparent composites offer a promising solution due to their significant reduction in weight compared to glass.

Furthermore, light trapping plays a crucial role in maximizing the efficiency of silicon-based solar cells. A cover with low haze is not favorable, as it allows light to pass through the solar cells without scattering. Introducing haze to the material optimizes the power conversion efficiency by promoting the scattering of light. This increase in scattering leads to enhanced light trapping within the solar cells, facilitated by the added path length of light (Fang et al., 2014).

Greenhouse roofings

As the world population continues to increase, so does the demand for vegetables and fruits. Consequently, greenhouse productivity must also increase to meet this rising demand. The primary function of greenhouses is to protect crops from environmental factors such as weather and animals, while also maintaining a stable temperature. This contributes to enhancing both the quantity and quality of the crops (Timmermans et al., 2020).

One crucial aspect of plant growth is controlling solar irradiance, which can be categorized into various wavelength regimes:

- Ultraviolet: 0-400 nm
- Photosynthetically active radiation (PAR): 400-700 nm
- Near-infrared: 700-2500 nm

PAR is considered the key element of irradiance for photosynthesis and is often the limiting factor in greenhouses. Significant efforts are made to increase PAR light by utilizing anti-reflective surface treatments, maintenance/cleaning practices, and developing new surface structures. PAR lighting can be divided into direct and diffuse components, with the latter being more favorable.

While diffuser materials may reduce the intensity of incoming light, they allow for deeper light penetration, resulting in a more favorable distribution of light and ultimately improving the growth and development of crops. Studies have shown that distributing light more evenly leads to increased plant yields, as it reduces the likelihood of plant stress and allows for alterations in plant morphology. In this context, materials that promote the diffusion of light are of interest, with TFRPs offering a potential solution.

Chapter 3

Problem Statement

The focus of this study is to manufacture transparent glass fiber-reinforced polymers (TGFRPs) and to understand the manufacturing parameters and material selection/modification that influence transparency. Additionally, this study will explore how to utilize this transparency to visualize and detect failures, damage, and stresses in TGFRPs. The main research question addressed during this project is:

How can the transparency of glass fiber-reinforced polymers be controlled or optimized by modifying manufacturing parameters, and in what ways can this transparency aid in stress and failure analysis?

To address the main question, it is first broken down into several sub-questions:

- What optical tests and equipment are available for characterizing the transparency of TGFRP samples?
- Which manufacturing methods and parameters minimize void formation while maximizing fiber impregnation and transparency?
- How do the number of woven glass fiber layers and the sizing on the glass fibers affect the transparency of the TGFRP?
- What testing methods and parameters can be used to create visible damage within the composite without causing complete failure?
- What measurement equipment is available for visualizing damage and stresses within the composite?

Chapter 4

Materials and Methodology

4.1 Materials

4.1.1 Glass fiber material

The chosen glass fiber material is Hexforce 7581, which is a woven glass fabric with an 8-harness satin weave style. This means that a warp yarn passes under seven fill yarns, then over one fill yarn, and repeats. A higher harness number results in greater drape capability of the fabric, making the fabrication of parts with complex shapes much easier compared to a plain weave, which might require cuts to avoid wrinkles. A schematic of this specific fabric can be seen in [Figure 4.1](#).

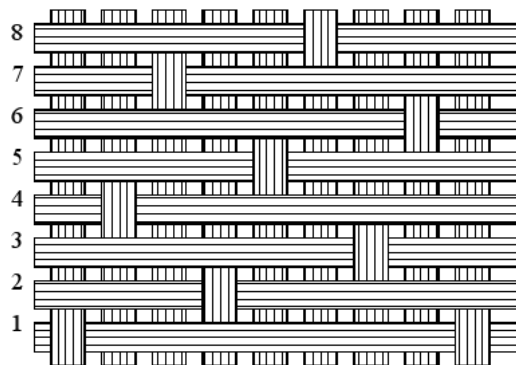


Figure 4.1: Schematic of 8-harness satin weave glass fiber fabric ([Hosur et al., 2003](#)).

Other useful properties of Hexforce 7581 are presented in [Table 4.1](#).

Table 4.1: Hexforce 7581 glass fiber fabric properties.

Properties	Value	Units
Yarn type (warp)	EC6 66	-
Yarn type (fill)	EC6 66	-
Fabric weight	299	g/m^2
Fabric thickness	0.22	mm
Breaking strength (warp)	570	$lb_f/inch$
Breaking strength (filling)	450	$lb_f/inch$

4.1.2 Resin

The decision was made to use Resin L and Hardener GL2 from R&G Composite Materials in Germany. This choice was based on a paper that utilized this material to fabricate transparent composites with refractive indices (RIs) similar to those in other studies that achieved the same objective, as seen in [Table 4.2](#).

Table 4.2: Refractive indices of resins used in other papers fabricating transparent glass fiber-reinforced composites.

Papers	Manufacturer	Resin refractive index [-]	Hardener refractive index [-]
(Yang et al., 2024)	Easy composites	1.5491	1.4689
(Caydamli et al., 2021)	R&G	1.5527	1.4685
(Zobeiry et al., 2020)	Rhino	1.555	1.50 and 1.460 (2 hardeners)

However, the paper that used the resin and hardener from R and G did not use methyl methacrylate (MMA) to optimize the RI matching between the glass fibers and the resin matrix.

4.1.3 Methyl methacrylate

The monomer MMA, used to match the RIs of the glass fibers and the resin matrix, was sourced from Sigma-Aldrich. Additionally, the Sigma-Aldrich MMA was used in a paper with the same objective of matching the RIs of glass fiber and epoxy resin ([Yang et al., 2024](#)).

4.2 Vacuum infusion process

For the manufacturing of the composite panels, a modified Vacuum Infusion Process (VIP) was used, as seen in [Figure 4.2](#), due to the selection of a low viscosity thermoset resin. The main modification includes the addition of a top caul plate between the fibers and the perforated release film. The use of these caul plates ensures smooth surface quality on both sides of the panel.

Perspex/plexiglass was chosen as the material for both the bottom and top plates due to its high-quality surface finish, availability, and cost-effectiveness. Over time, the surface quality of the plexiglass plates will inevitably degrade due to handling, leading to scratches or stains caused by resin. However, the plexiglass plates are available in various sizes and thicknesses, and replacing these caul plates is relatively inexpensive.

The detailed manufacturing plan of the TGFRP panels is provided in [Appendix A](#). The resin for the production of a TGFRP plate with 5 layers of glass fiber fabric was infused at a pressure of 50 mbar, measured by a digital vacuum barometer (GDH-200) connected to the vacuum pump. This pressure was increased to 100 mbar and 150 mbar for the TGFRP panels with 10 layers and 15 layers of glass fiber fabric, respectively. After the glass fabric was fully infused, the pressure was increased to 500 mbar and left to cure for 24 hours.

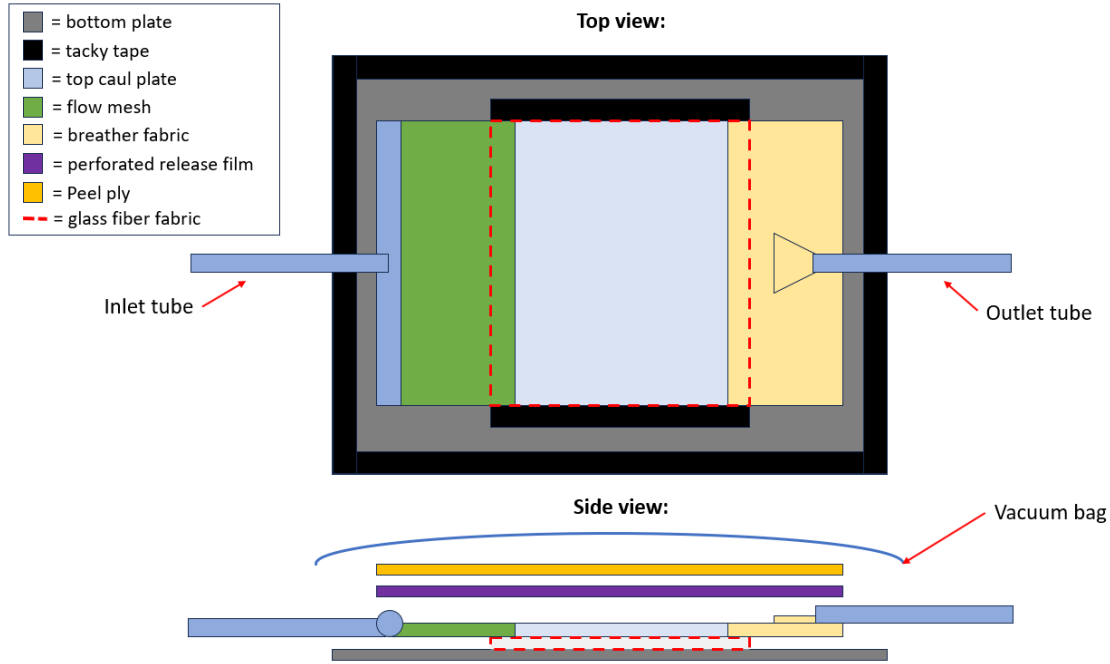


Figure 4.2: Modified vacuum infusion process for fabricating TGFRPs.

4.3 Sample preparation

4.3.1 Composite cutting machine

For cutting the TGFRP plates into samples with their desired dimensions, a Compcut ACS 600 was used. This machine is capable of cutting a composite panel with a surface area of $600 \times 600 \text{ mm}^2$. It was used to cut the composite tabs for the tensile testing specimens ($25 \times 50 \text{ mm}^2$), the tensile specimens according to the ASTM standard D3039 ($25 \times 250 \text{ mm}^2$), and the samples for the spectrophotometer measurements ($25 \times 50 \text{ mm}^2$).

4.3.2 Tabbing materials

During tensile testing, if precautions are not taken with the test specimen, failure can occur at the clamps, leading to invalid results. The force applied through the thickness due to the clamps on a specimen is higher than the tensile force, which causes high stress concentrations at the grip edges.

Dog-boned tensile specimen shapes are generally employed to counteract this phenomenon and ensure that failure occurs in the region with the smaller cross-section. However, due to the difficulty of cutting a composite plate into a dog-bone shape, an alternative method is required to address the stress concentrations caused by the grip force. Additionally, the grip surface can damage the resin and affect the reinforcing fibers, promoting failure in this region.

End tabbing can be employed to reduce stress concentrations and protect the surface of the test specimen. Several tabbing materials have been prepared for tensile testing, and the material that provides the best results will be used for the tensile specimens in the final experiment. A list of available tabbing materials is provided in [Table 4.3](#). The adhesive used to bond the tabs to the specimens is LOCTITE EA 3430, and a detailed tabbing procedure for the TGFRP tensile specimens is provided in [Appendix C](#).

Table 4.3: Tabbing materials.

Material type	Thickness [mm]
No tabbing material	-
Aluminium	1.0
GFRP (0/90)	1.95
GFRP (± 45)	1.95
TGFRP (0/90)	1.23

4.4 Measurement equipment and techniques

4.4.1 Refractive index measurement

For the measurement of the solid resin samples' RI, a Zeiss Abbe refractometer was used. This refractometer only allows for the measurement of samples at 589 nm (yellow sodium D-line), and this was done at room temperature. The solid resin samples with various MMA wt% have approximate dimensions of 25 x 8 x 5 mm^3 (length x width x height).

For this measurement, it was important to have smooth, mirror-like surfaces on the bottom and front sides of the samples, which are in contact with the measurement prism and the light source, respectively. The detailed measurement procedure, as well as the complete sample preparations, are provided in [Appendix B](#).

4.4.2 Transmission measurement

For the transmission measurement, a Shimadzu UV-1800 spectrophotometer was used to measure the light transmission of the glass fiber reinforced samples across the visible light spectrum, with a wavelength range between 400-700 nm. A bracket was designed in the CAD software Fusion 360 and printed using a Prusa MK3S+ for the measurement of the solid samples with a surface area of 25x50 mm^2 (W x H). The data were saved into a CSV file and post-processed in Microsoft Excel and Python.

4.4.3 Confocal microscope

A Keyence VK-X1000 confocal scanning microscope was used to obtain optical images of the TGFRP samples. It combines a laser and white light source to scan a specimen's surface and collect surface data as well as high-resolution optical images. The microscope also allows for different magnification settings, ranging from 5x to 20x.

4.5 Mechanical testing

4.5.1 Testing machine and specimen dimensions

Mechanical tensile testing of TGFRP specimens was conducted using a Zwick 20 kN universal testing machine in accordance with ASTM standard D3039, which specifies surface dimensions of 25 x 250 mm (W x H) for the specimens. Aluminum tabs with surface dimensions of 25 x 50 mm (W x H) were added to prevent failure at the clamping area during testing. Additionally, open-hole tensile specimens, which required no tabbing materials, were prepared for testing. Detailed preparation of the tensile testing samples is provided in [Appendix C](#).

4.5.2 Digital image correlation

Digital Image Correlation (DIC) is a method used to measure strains and deformations on the sample surface. This is achieved by applying a speckle pattern to the specimen's surface, which deforms with

the material during loading and is tracked by cameras. A dual-camera system will be used to measure displacements in all three directions: x, y, and z.

Typically, specimens are painted white, with a speckle pattern applied on top using black spray paint. However, to retain the transparency of the TGFRP samples for capturing opacity changes and photoelasticity, the white paint has been omitted. Instead, a monitor with a white background, used to visualize photoelasticity, will illuminate the TGFRP samples to provide sufficient contrast for the DIC to function effectively.

For DIC, two 5-megapixel DIC cameras with 50 mm lenses were used, capturing an image every 200 ms. The post-processing tool was VIC-3D 7, with a subset of 29 and a step size of 7 applied during post-processing.

4.5.3 Photoelasticity setup

In order to view the fringe patterns of the TFRP specimens, the specimen needs to be placed between two polarizers with a uniform backlight. For this purpose, a monitor, which typically consists of a polarizer and backlight, will be positioned behind the tensile testing machine. A polarizer will be placed in front of a third camera positioned between the two DIC cameras to capture the fringe patterns. This setup allows for simultaneous capture of the DIC images and videos of the changing fringe pattern due to photoelasticity. A top view of this setup is provided in [Figure 4.3](#).

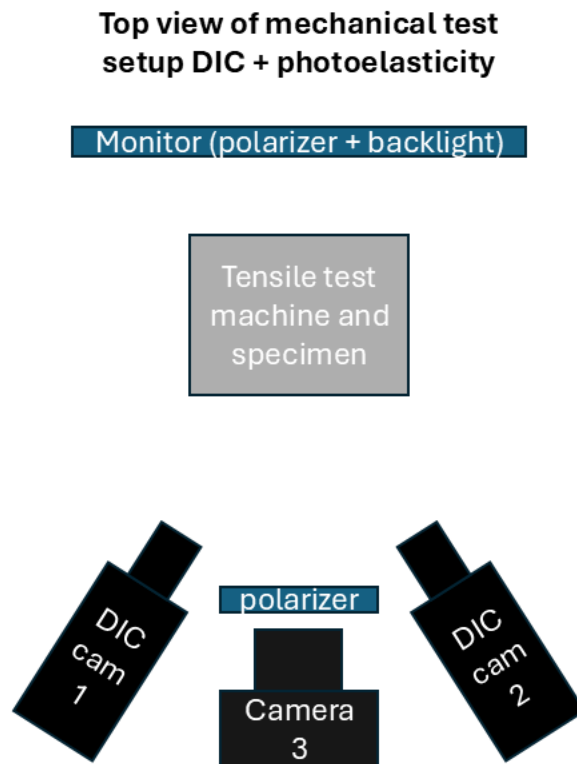


Figure 4.3: Top view of the mechanical testing setup for DIC and photoelasticity.

Chapter 5

Results and Discussion: Manufacturing and Parameter Studies

5.1 Vacuum infusion

The first objective of this project was to optimize the manufacturing method and assess the influence of the surface quality of the top caul plate and bottom plate on the transparency of the transparent glass fiber-reinforced polymer (TGFRP) panels. Epokote 04908 resin and hardener was used initially, as the resin with the desired refractive index (RI) properties that had been ordered was unavailable at the time. New mold plates with higher surface quality were also ordered. Plexiglas panels were obtained for this purpose.

The produced TGFRP panels are shown in [Figure 5.1](#). The TGFRP panel in [Figure 5.1a](#) was made using an aluminum top caul plate and a bottom glass plate. The TGFRP panel produced using the plexiglass plates is shown in [Figure 5.1b](#). From these results, an observation can be made that the surface quality of the molds/caul plates has a significant impact on the transparency of the TGFRP samples.



(a) Aluminium plate (top) and glass plate (bottom).



(b) 2 Plexiglas plates (top and bottom).

Figure 5.1: Influence of the mold's surface quality on the transparency of the TGFRP panels.

Once the desired resin from R&G arrived, the same modified vacuum infusion process and parameters were applied to produce the TGFRP panel using the plexiglass plates for the top caul plate and bottom plate, as shown in [Figure 5.2](#). An initial visual observation suggests that the transparency of the TGFRP panel has improved, likely due to better RI matching between the resin and hardener from R&G and the glass fibers, compared to the Epokote 04908 resin and hardener.



Figure 5.2: TGFRP panel produced using the modified VIP with resin from R&G.

[Figure 5.3](#) shows the average light transmittance curve across the visible wavelength range for the TGFRP samples and the pure resin samples. The sample size for the TGFRP samples is 38, and for the pure resin samples, it is 20 ($N = 38$ and $N = 20$, respectively). The color bands indicate the average transmission values \pm the calculated standard deviation. The thickness of the samples was measured to be 1.21 mm and 1.33 mm, respectively. The fiber volume fraction (FVF) of the TGFRP samples was calculated to be approximately 50%.

[Figure 5.3](#) shows that the curve for the pure resin samples remains almost a straight line. This can be explained by the fact that light of nearly all wavelengths in the visible spectrum passes through the pure resin samples equally, resulting in a colorless image when viewing an object through the sample, as illustrated in [Figure 5.4](#) and [Figure 5.5](#).

For the TGFRP sample, the light transmission curve shows a noticeable peak at a wavelength around 510 nm, which corresponds to the green color range (500-570 nm). This peak in the wavelength associated with the color green is expected, as a noticeable green hue is visible when viewing objects through the TGFRP samples.

While the average transmittance values around 500 nm (green color range) for the TGFRP samples do not decrease significantly compared to the pure resin samples, the light transmission curve shows a noticeable decrease in transmittance at wavelengths associated with other color ranges. For example, the transmittance at 400 nm, corresponding to the color purple, is reduced by half. A similar reduction is observed at 700 nm, the wavelength associated with the color red.

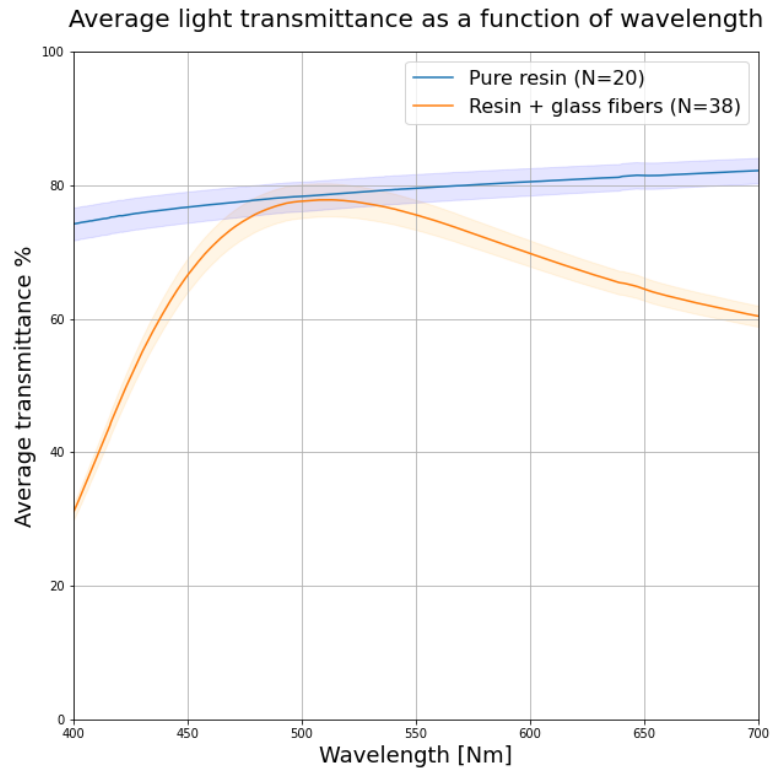


Figure 5.3: Average light transmission results for pure resin and TGFRP samples.

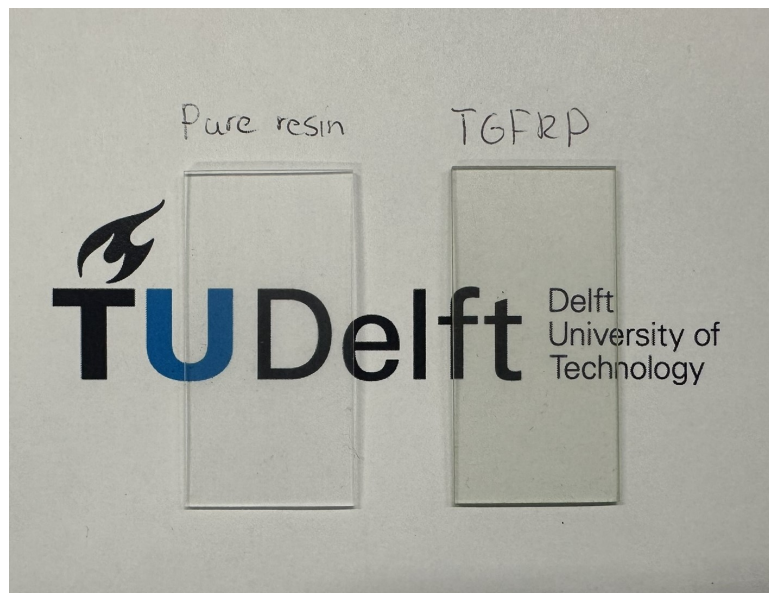


Figure 5.4: Pure resin vs. TGFRP sample directly on top of the TU Delft logo.



Figure 5.5: Pure resin sample (left) vs. TGFRP sample (right) at a distance from the TU Delft logo.

5.2 The influence of MMA on the refractive index and light transmission of GFRPs

The next investigation focuses on the influence of MMA on the refractive index (RI) of the epoxy resin. According to the literature, optimizing the transparency of GFRP panels requires matching the refractive indices of the resin and the glass fibers. Therefore, to optimize the transparency of the TGFRP samples, the RI of the resin must be determined. Since the RI of cured epoxy resins is typically higher than that of glass fibers, the addition of MMA is expected to reduce the RI of the epoxy resin.

Table 5.1 presents the measurement results from the Abbe refractometer, which measures the RI of the pure resin samples with varying wt% of MMA at a wavelength of 589 nm. The table indicates that the addition of MMA has minimal influence on the resin's RI. The slight variations in RIs at different wt% of MMA may also be attributed to inherent variations in the samples themselves due to preparation and impurities. Therefore, it can be initially concluded that adding MMA to the epoxy resin has a negligible impact on the RI and, consequently, on the transparency of the TGFRP panels.

Table 5.1: Average measured RI for pure resin samples with different wt% MMA.

Wt% MMA	Average RI [-] (N=10)	Standard deviation [-]
0	1.558	0.0051
2.5	1.559	0.0021
5	1.559	0.0029
7.5	1.560	0.0023
10	1.558	0.0025

However, when producing the TGFRP panels with varying wt% of MMA, a noticeable difference can be observed. Figure 5.6 shows the manufactured panels with different wt% percentages of MMA using the modified VIP. From left to right in Figure 5.6: 10% MMA, 7.5% MMA, and 0% MMA. The thickness of these samples was measured to be 1.21, 1.23, and 1.21 mm, respectively. Because the modified VIP process uses a caul plate between the glass fibers and the vacuum bag, the thickness variation in the composite is minimal. The fiber volume fraction (FVF) of all these panels has been calculated to be approximately 50%.

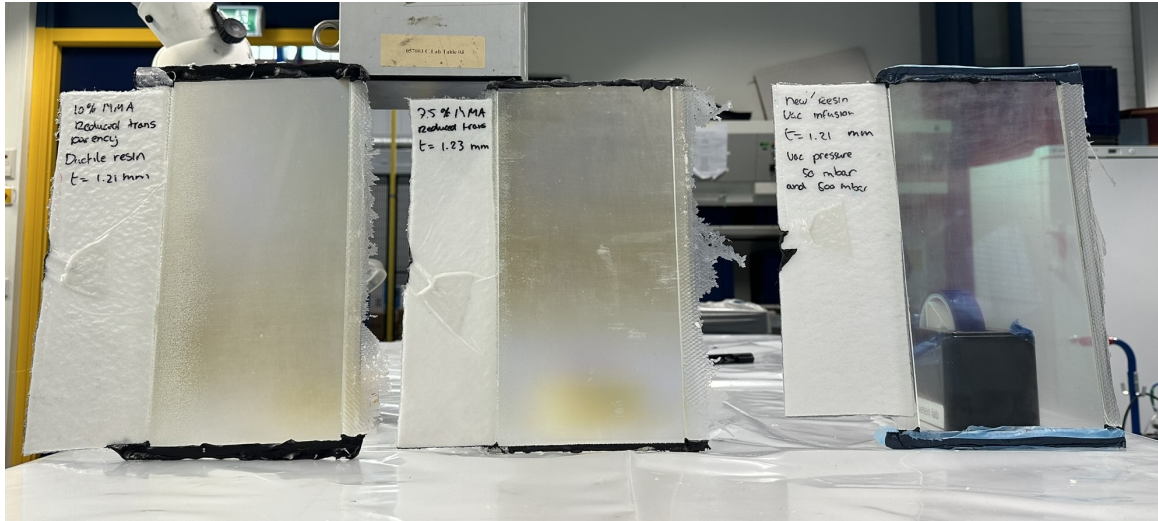


Figure 5.6: Manufactured GFRP panels with varying weight percentages of MMA. From left to right: 10% MMA, 7.5% MMA, and 0% MMA.

From [Figure 5.6](#), an initial observation can be made that the transparency of the panels significantly decreases with increasing wt% of MMA. Even 0.5%, 1%, and 2.5% MMA by weight resulted in TGFRP panels with visibly lower transparency. The thickness of these panels is 1.18, 1.22, and 1.21 mm, respectively. This suggests that, while the change in RI due to the addition of MMA measured at 589 nm using the ABBE refractometer was very small, the RI of the resin at other wavelengths may have changed significantly, resulting in reduced transparency of the GFRP panels with increasing wt% of MMA.

Another observation is that, when using the same production process (the modified VIP) and consistent parameters across all panels, the presence of voids becomes more pronounced with increasing MMA content. These voids can be seen on the left side of the panels, which corresponds to the vacuum/outlet side in the modified VIP process.

This phenomenon can be explained by the fact that the viscosity of MMA is much lower compared to that of the resin. Therefore, increasing the amount of MMA lowers the overall viscosity of the mixture. Under the same manufacturing conditions, particularly the vacuum pressure, this results in faster resin flow rates during the infusion of the glass fibers. Instead of pushing the air inside the vacuum bag out, the resin traps air bubbles in the glass fibers, resulting in voids after curing, as seen in [Figure 5.6](#).

5.3 Spectrophotometer measurements: pure resin samples

To briefly summarize, [Table 5.1](#) shows that the RI of the resin hardly changed with the addition of MMA. However, when producing the GFRP samples with varying weight percentages of MMA, a noticeable difference can be visually detected, as seen in [Figure 5.6](#). Therefore, a new hypothesis can be proposed: either the measurement using the Abbe refractometer at 589 nm is insufficient for solid samples, or while the RI of the resin at 589 nm remains relatively constant with varying wt% of MMA, the RI at other wavelengths may have changed significantly.

Therefore, it is worthwhile to investigate the influence of MMA on the transmission curve across the visible light spectrum using a spectrophotometer. [Figure 5.7](#) presents the results from this measurement. It can be observed that increasing the MMA content in the resin samples leads to higher light transmittance across all wavelengths, indicating a decrease in the RI of the resin. After all, a lower RI allows light to travel faster and be bent less.

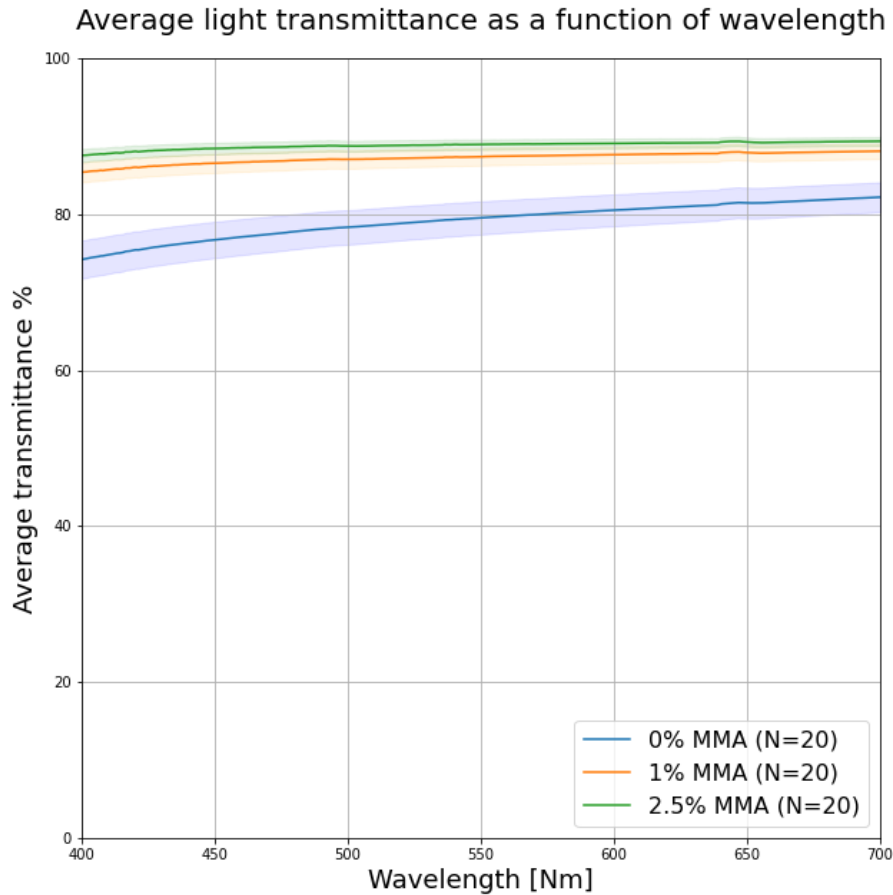


Figure 5.7: Average light transmission results for pure resin samples with varying MMA percentages in weight.

However, it must be noted that even though Figure 5.7 shows a clear difference in transmittance across all wavelengths, no distinct differences in transparency are observed when visually inspecting the samples. This suggests that a small difference in light transmission (approximately 10%) may have a negligible effect on the transparency perceived by the human eye.

5.4 Spectrophotometer measurements: TGFRP samples

The next step is to investigate the influence of both the introduction of MMA and the glass fibers on the light transmission capabilities of TGFRPs. Figure 5.8 shows the average light transmission results of GFRP samples with varying MMA weight percentages. The maximum average transmittance (MAT) and the average wavelength at which the peak values occurs with their standard deviations are given in Table 5.2. Similar to Figure 5.3, it can be seen that the introduction of the glass fibers to the resin creates a peak in the light transmission curve.

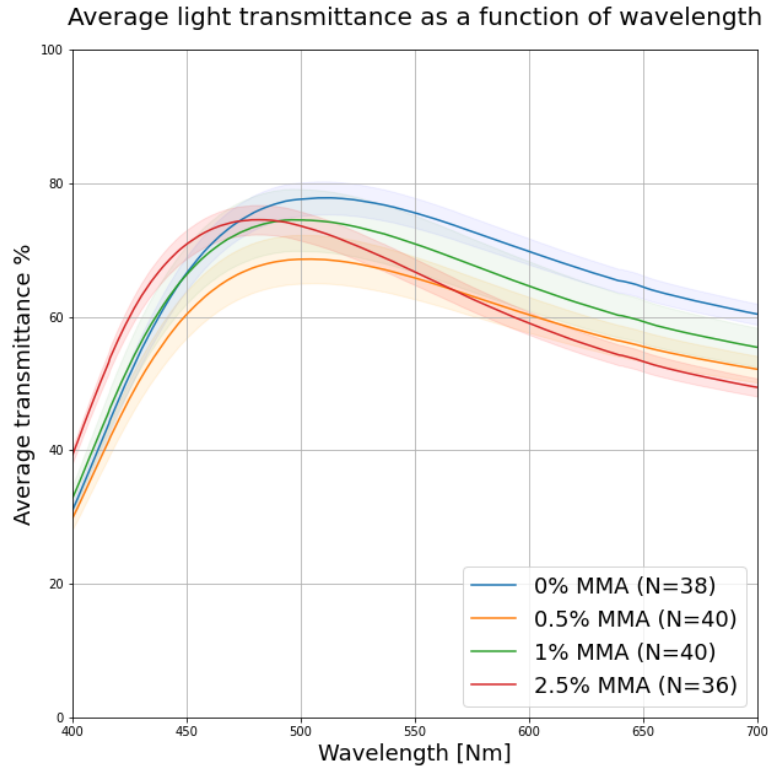


Figure 5.8: Average light transmission results for GFRP samples with varying wt% of MMA.

Table 5.2: Transmission data for different MMA percentages (TGFRP).

Percentage MMA in weight [%]	MAT [-]	SD [-]	Wavelength (MAT) [nm]	SD [nm]
0	77.840	2.466	510.842	2.153
0.5	68.665	3.624	503.590	3.107
1	74.537	4.639	497.045	2.235
2.5	74.560	2.205	481.189	1.726

From [Figure 5.8](#) and [Table 5.2](#), several observations can be made. First, the addition of MMA seems to decrease the maximum light transmission in all cases compared to the light transmission curve without MMA. The decrease in light transmission, and therefore also in transparency, is also visible in the TGFRP samples. However, it must be noted that while the raw measurements, which are provided in [Appendix D](#), show substantial variations in the peak values, but the wavelength at which the peak values occur is much more consistent.

Additionally, with increasing MMA content in the composite, the wavelength at which the maximum transmittance occurs shifts to the left. While the average transmission curve for 0.5% MMA shows a lower maximum transmission compared to the higher MMA contents, visual inspection reveals it is more transparent compared to the sample with 2.5 wt% MMA content as seen in [Figure 5.9](#) and [Figure 5.10](#). This suggests that, similar to the pure resin samples in [Figure 5.7](#), maximum transmission may only tell part of the story, and the wavelength at which the peak occurs could have a greater impact on the transparency of the samples.



Figure 5.9: Transparency of the TGFRP samples directly on top of the TU Delft Logo. From left to right: 0% MMA, 0.5% MMA, 1.0% MMA, 2.5% MMA.



Figure 5.10: Transparency of the TGFRP samples at a distance from a sheet of text. From left to right: 0% MMA, 0.5% MMA, 1.0% MMA, 2.5% MMA.

5.5 Spectrophotometer measurements: varying layers

Another variable worth investigating is the effect of increasing glass fiber fabric layers on the transparency of the TGFRP samples. For this experiment, TGFRP panels with 10 and 15 layers were produced with thicknesses of 2.37 and 3.61 mm, respectively. [Figure 5.11](#) shows the average light transmission results of TGFRP samples with varying layers. The MAT and the average wavelength at

which the peak values occur, along with their standard deviations, are provided in [Table 5.3](#).

From initial production, it was observed that keeping the manufacturing parameters of the modified VIP process the same as the parameters used for the 5 layers TGFRP panel, resulted in noticeable formation of voids near the outlet side similar to increasing MMA content in [Figure 5.6](#). To counteract this, the vacuum infusion pressure was increased from 50 mbar to 100 mbar and 150 mbar for the manufacturing of the 10- and 15-layer TGFRP panels, respectively. Even though the manufacturing parameters were changed, the calculated FVF for the 10- and 15-layer TGFRP panels remained close to 50%.

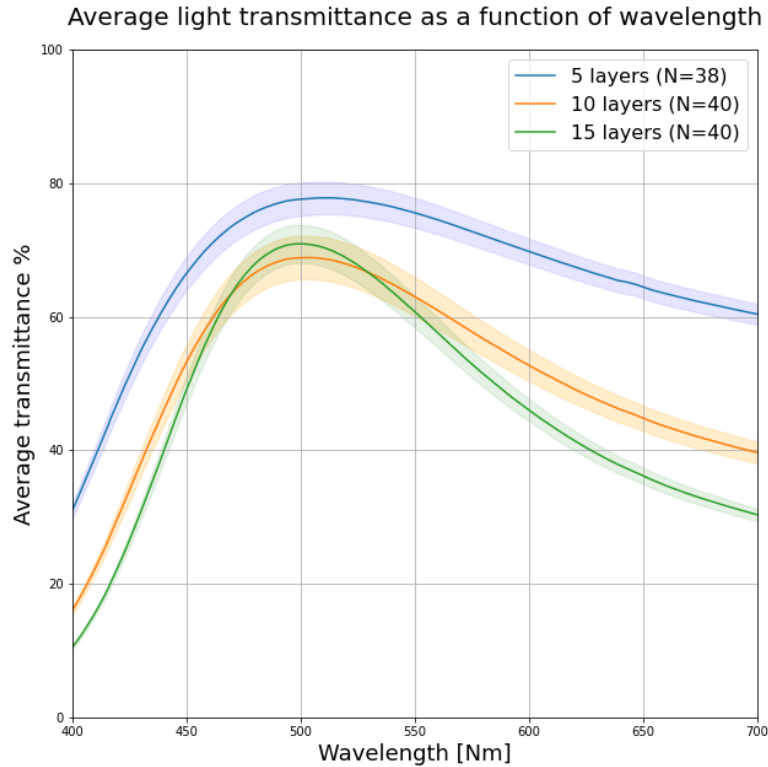


Figure 5.11: Average light transmission results for GFRP samples with varying glass fiber fabric layers.

Table 5.3: Transmission data for TGFRP with varying layers.

Layers	MAT [%]	SD [%]	Wavelength (MAT) [nm]	SD [nm]
5	77.840	2.466	510.842	2.153
10	68.895	3.256	502.130	1.506
15	70.942	2.855	499.445	1.193

From [Figure 5.11](#) and [Table 5.3](#), it can be observed that increasing the number of layers generally decreases the MAT, which is also evident in the samples due to the loss of transparency. A less expected result is that the 10-layer samples show a slightly lower MAT compared to the 15-layer samples. This could be explained by the fact that the TGFRP samples with 10 layers were made using a second batch of resin, which was visibly less transparent, albeit very minimally.

The original expectation was that the average transmission curve of the 10-layer samples would lie between the average transmission curves of the 5-layer and 15-layer samples. This means that the transmission values for the 10-layer samples in [Figure 5.11](#) across all wavelengths should be shifted upwards. The explanation for this unexpected result may lie in the fact that the transmission values

across all wavelengths for the second batch of resin are lower compared to the first batch. This will be validated through an additional experiment with measurements and elaborated on later.

Even though the MAT differences between the TGFRP samples with 10 layers and those with 15 layers are minimal, the transparency loss is observed visually in [Figure 5.12](#) and [Figure 5.13](#) shows a more drastic difference. This could be attributed to a shift in the wavelength to the left, similar to the effect observed with varying wt% of MMA. When looking at [Figure 5.11](#), it becomes clear that another effect is at play.

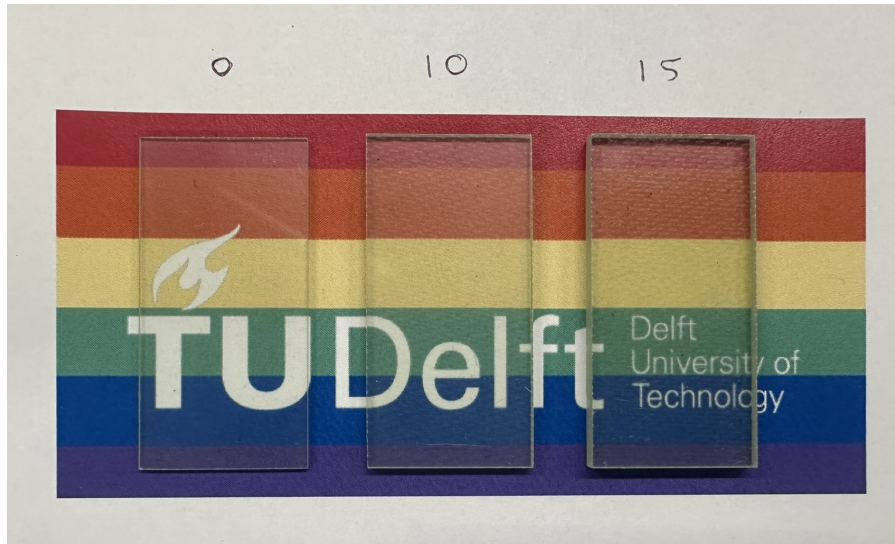


Figure 5.12: Transparency of the TGFRP samples directly on top of the TU Delft logo. From left to right: 5 layers, 10 layers, and 15 layers of glass fiber fabric.

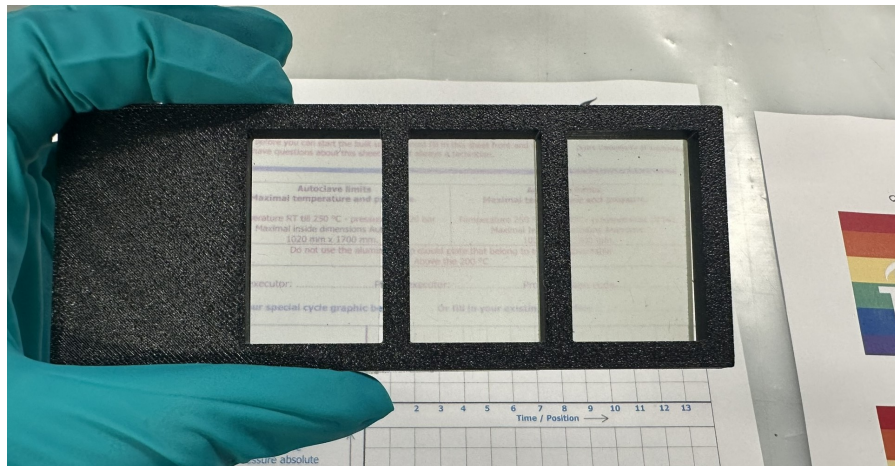


Figure 5.13: Transparency of the TGFRP samples at a distance from a sheet of text. From left to right: 5 layers, 10 layers, and 15 layers of glass fiber fabric.

From this figure, it can be seen that the average transmission curve also becomes narrower. As the curve narrows, less light over a range of wavelengths is transmitted, which could contribute to the loss in transmission in addition to the shift in the wavelength where the MAT occurs. This suggests that more factors are at play, and the MAT may have less of an effect than the literature suggests.

Next, the transmission data for varying batches of resin and hardeners are presented. When making the TGFRP samples with a different resin batch, it was visibly observed that the second batch of resin

and hardener resulted in slightly less transparent TGFRP samples. To investigate this phenomenon, transmission measurements were performed to compare the TGFRP samples between the batches.

5.6 Spectrophotometer measurements: varying resin batches

To explain the unexpected result in Figure 5.11, where the average transmission curve of the 10-layer samples does not lie between the average transmission curves of the 5-layer and 15-layer samples, an additional experiment has been conducted to test the hypothesis that the second batch resin has different light transmittance properties compared to the first batch resin.

Figure 5.14 shows the average light transmission as a function of wavelength for TGFRP samples with 5 layers of glass fibers, fabricated using different batches of resin and hardener. The MAT and the average wavelength at which the peak values occur, along with their standard deviations, are provided in Table 5.4. From Figure 5.14 and Table 5.4, it can be observed that the second batch of resin and hardener resulted in a lower MAT starting from a wavelength of 430 nm and a shift in the average wavelength at which the maximum transmittance occurs.

Therefore, the expectation is that if the same resin/hardener batch (first batch) had been used to produce the 10-layer TGFRP samples, the maximum absorbance transmission (MAT) for the 10-layer samples in the average transmission curve in Figure 5.11 would likely have fallen between the MAT of the 5-layer and 15-layer samples, thereby confirming the hypothesis.

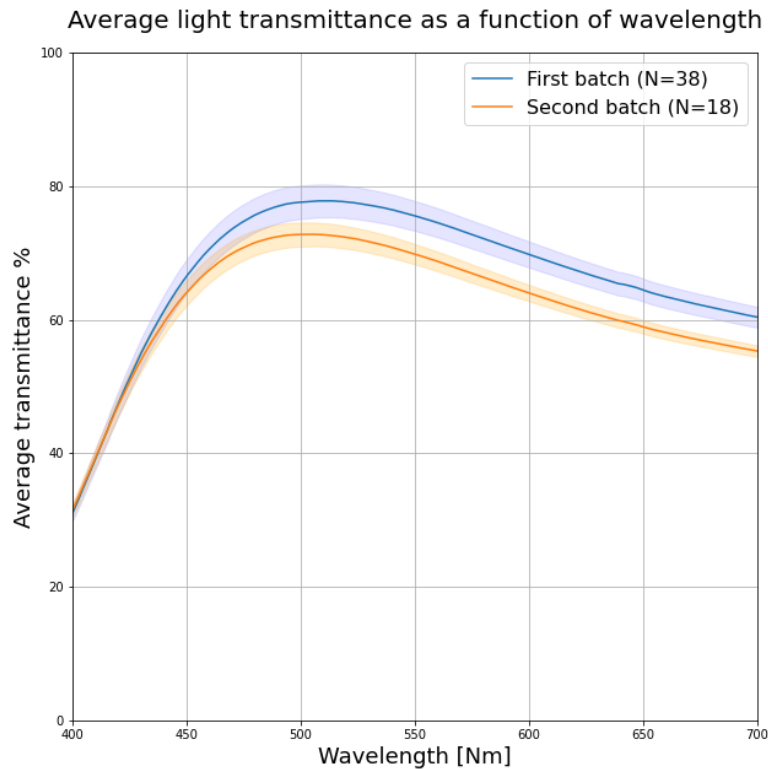


Figure 5.14: Average light transmission results for TGFRP samples made from different resin and hardener batches.

Table 5.4: Transmission data for TGFRP samples from different batches of resin and hardener.

Batches	MAT [%]	SD [%]	Wavelength (MAT) [nm]	SD [nm]
1	77.840	2.466	510.842	2.153
2	72.817	1.787	502.933	2.899

5.7 Spectrophotometer measurements: post-curing

The next study of parameters is the influence of post-curing on the transparency of the TGFRP samples. From the literature, it is stated that the RI is a function of temperature, thus, in theory, post-curing should have a noticeable effect on the transparency as well as the light transmission capability of the samples.

Figure 5.15 shows three TGFRP samples with 5 layers of glass fiber fabric. From left to right: non-post-cured, post-cured at 40°C, and post-cured at 60°C, all for 24 hours. As seen in Figure 5.16, the post-curing of samples does indeed have an influence on the transparency of the TGFRP samples when viewing objects from a distance. Noticeably, the higher the post-curing temperature, the greater the loss in transparency.

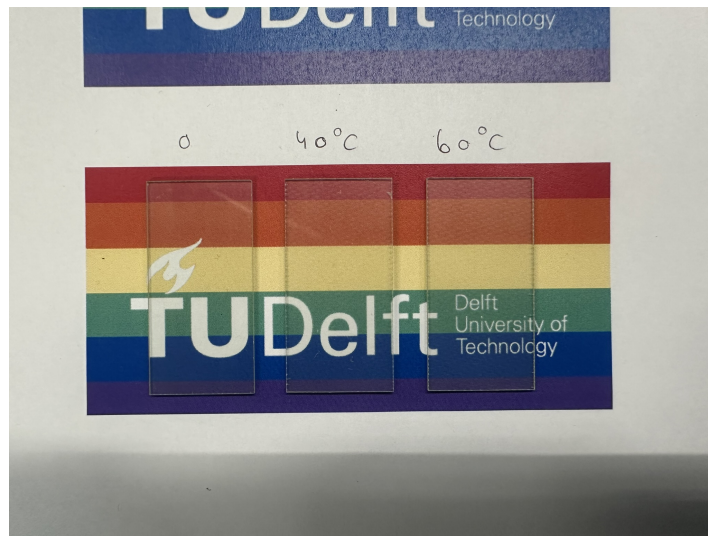


Figure 5.15: TGFRP samples: non-post-cured vs post-cured samples directly on top of the TU Delft logo. From left to right: non-post-cured, post-cured at 40°C, and post-cured at 60°C for 24 hours.

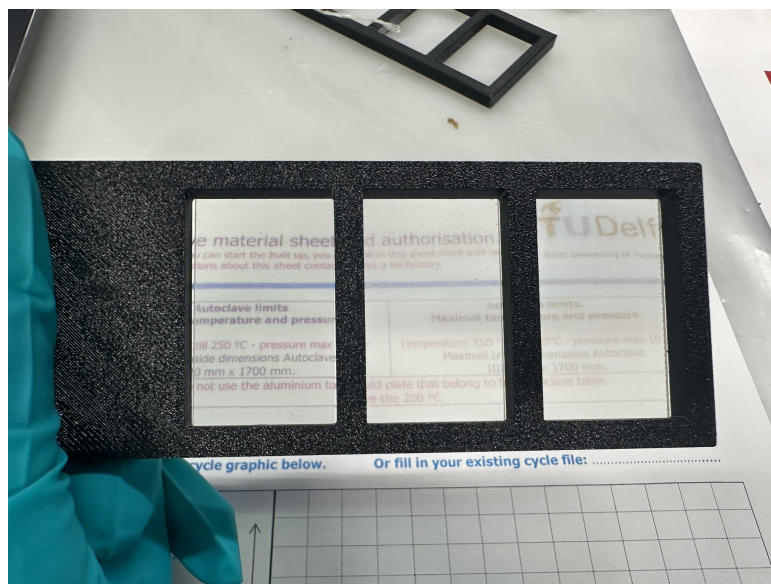


Figure 5.16: TGFRP samples: non-post-cured vs post-cured samples at a distance from a sheet of text. From left to right: non-post-cured, post-cured at 40°C, and post-cured at 60°C for 24 hours. The images were taken at a distance from the TU Delft logo.

Figure 5.17 shows the average light transmission as a function of wavelength for different post curing conditions. The MAT and the average wavelength at which the peak values occur, along with their standard deviations, are provided in Table 5.5.

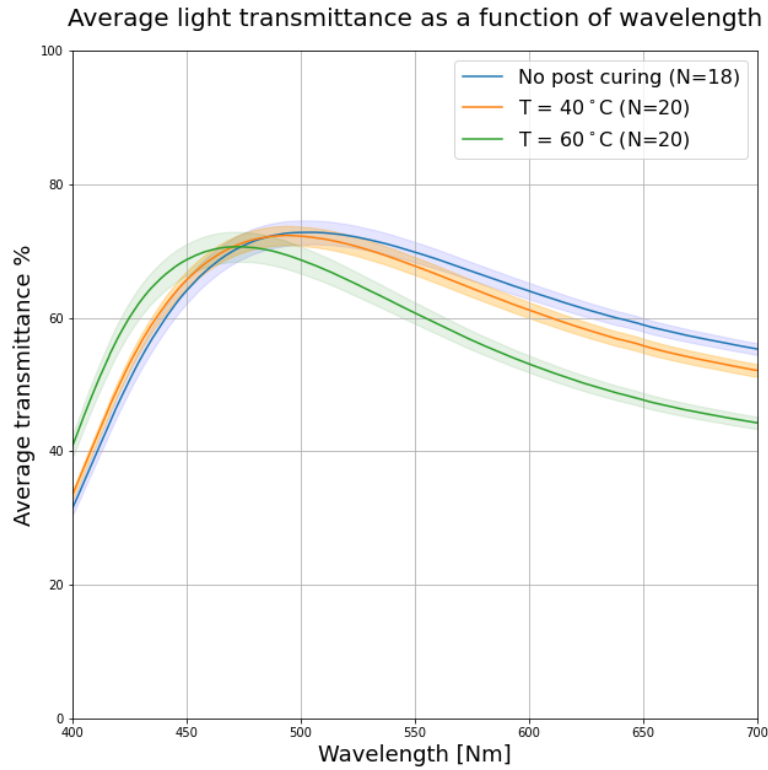


Figure 5.17: Average transmission curve for TGFRP samples under varying post-curing conditions.

Table 5.5: Transmission data for TGFRP samples at different post-curing temperatures.

Conditions	MAT [%]	SD [%]	Wavelength (MAT) [nm]	SD [nm]
No post curing	72.817	1.787	502.933	2.899
Post curing at 40 ° C	72.355	1.445	493.675	1.313
Post curing at 60 ° C	70.670	2.249	472.1	2.083

When examining the light transmission curves of the post-cured and non-post-cured samples in Figure 5.17, it is evident that post-curing has a noticeable effect on the average wavelength at which the MAT occurs, while minimally affecting the MAT value. The wavelength of the MAT shifts to the left with increasing post-curing temperatures, moving into the range corresponding to blue light (380–500 nm). This shift is also visually apparent, as a blue hue can be seen when viewing a white background on a computer through the composite.

Similar to varying the MMA weight percentages, post-curing shifts the wavelength at which the MAT occurs; however, unlike MMA variation, it has a minimal effect on the MAT value. This can be validated by looking at the average wavelength at which the maximum transmission of light occurs as seen in Table 5.5. This implies that varying the post-cure temperature could be a more controlled method of matching the RI of the resin and glass fibers at a preferred wavelength compared to the addition of MMA.

5.8 Sizing experiment

Next, the influence of sizing on the transparency of the TGFRPs is investigated. [Figure 5.18](#) shows the TGFRP sample produced using five layers of glass fiber fabric, following the removal of sizing by the burn-off method in the oven at 565°C for 24 hours. In this figure, a noticeable loss of transparency can be observed, similar to the post-curing experiment. As with the post-cured sample at 60°C, a distinct blue tint is visible through the panel, suggesting that the wavelength of MAT has shifted to the left, into the blue color range.

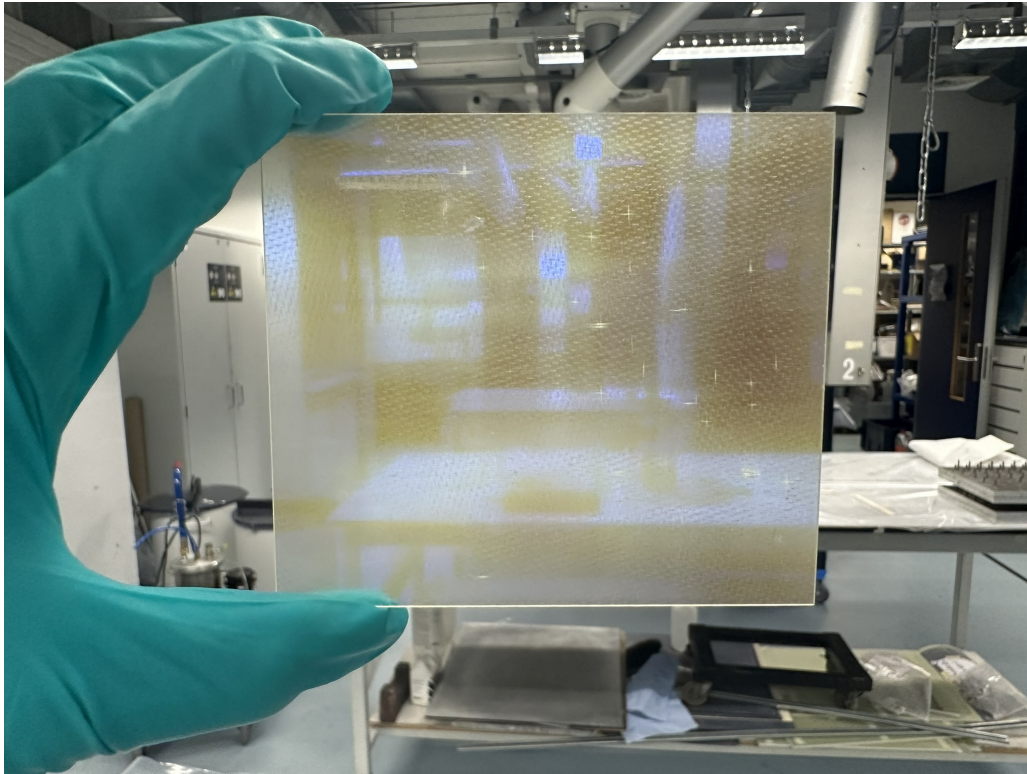


Figure 5.18: TGFRP panel produced using glass fiber fabric after sizing removal by burn-off.

Even though the resin used to produce the TGFRP panel without sizing was not subjected to elevated temperatures, the result is very similar to that of the TGFRP sample from the post-curing experiment. This suggests that elevated temperatures primarily affect the RI of the glass fibers. To test this hypothesis, pure resin samples with a thickness of approximately 1.2 mm, matching that of the TGFRP samples, were post-cured at 60°C for 24 hours. [Figure 5.19](#) shows the results of this experiment. From this figure, it can be observed that although one of the resin samples was subjected to elevated temperatures, the transparency remained similar. This confirms that the transparency loss in the TGFRP samples subjected to elevated temperatures is mainly caused by a change in the RI of the glass fibers.

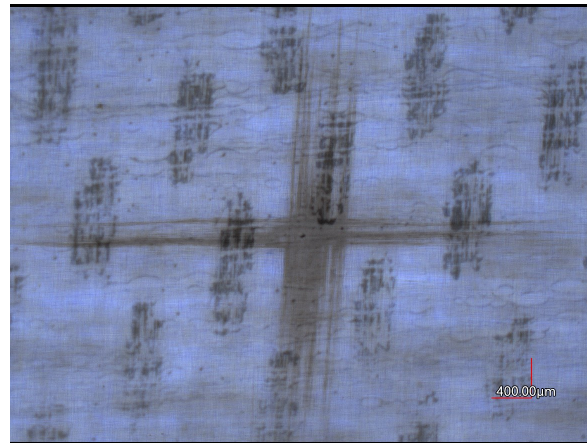


Figure 5.19: Pure resin sample (left) vs post-cured resin sample (right).

In addition to the transparency loss in the TGFRP panel, other defects can be observed, such as visible fibers and cross-shaped marks in the material, as seen in [Figure 5.20](#). These defects could be attributed to the absence or reduced effectiveness of the sizing, which promotes proper bonding between the fibers and the polymer matrix. The visible fibers are likely due to exposed glass fibers resulting from the removal of the caul plate. Instead of adhering to the glass fibers, a thin layer of epoxy resin may have peeled off along with the caul plate. The cross-shaped marks resemble dry glass fibers that were not adequately infiltrated by the resin.



(a) Visible glass fibers.



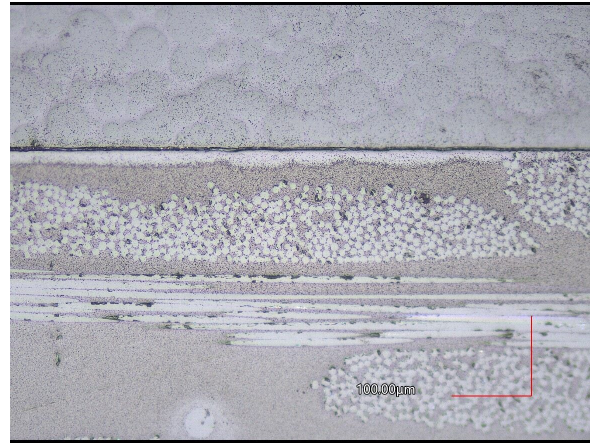
(b) Cross-shaped marks.

Figure 5.20: Microscopy images of defects in the TGFRP sample (sizing removed).

To further investigate whether the visible fibers in the TGFRP panel are indeed exposed glass fibers, TGFRP samples with and without sizing were cut and embedded in green resin to allow side (in-plane) viewing through a confocal microscope. [Figure 5.21](#) shows a microscopy image of the TGFRP sample with sizing from this side view. Some defects, such as impurities, along with dark marks and scratches from the sanding and polishing process, can be observed. However, the infiltration quality of the resin into the glass fibers appears to be high, with no visible voids.



(a) Side view of the TGFRP sample.

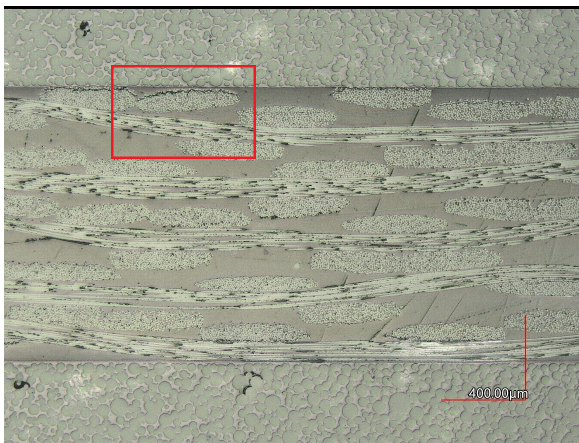


(b) Zoomed-in view of the glass fiber bundles.

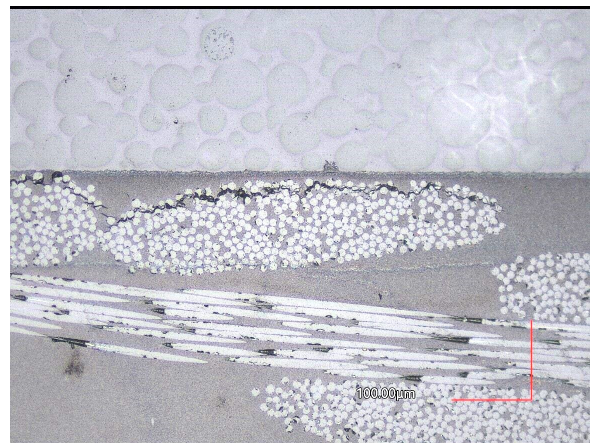
Figure 5.21: Microscopy images of the embedded TGFRP sample (with sizing).

Figure 5.22 shows a microscopy image of the TGFRP sample without sizing from the side through the confocal microscope. When compared to the microscopy results of the TGFRP sample with sizing in Figure 5.21, one key difference can be observed in the glass fiber bundles. By comparing the zoomed-in microscopy images in Figure 5.21b and Figure 5.22b, which focus on the glass fiber bundles near the surface of the TGFRP sample, it can be seen that the TGFRP sample without sizing shows cracks at the edges of the individual glass fibers, which are not present in the TGFRP sample with sizing.

These cracks recur in regions near the surface, where the resin layer is thin. Additionally, it can be seen that near the surface of the TGFRP sample, all glass fibers are covered with resin, which disproves the assumption of exposed fibers. While the initial assumption was that the visible glass fibers in the TGFRP sample without sizing were due to exposed fibers, it has now been confirmed that the visible fibers are actually attributed to cracks in the fiber bundles near the surface of the TGFRP panel, resembling debonded fibers.



(a) Side view of the TGFRP sample.



(b) Zoomed-in view of the glass fiber bundles.

Figure 5.22: Microscopy images of the embedded TGFRP sample (sizing removed).

5.9 Initial microscopy result

Initial microscopy results of a damaged TGFRP sample, as seen in [Figure 5.23](#), demonstrate the benefits of characteristics like high transparency. From this damaged TGFRP sample, several imperfections and failure modes can be observed, such as voids, impurities, fiber debonding, and delamination. When these defects occur, the loss of light can immediately be detected visually. Fiber debonding and delamination show opaque areas, while voids appear as tiny air bubbles in the composite material.

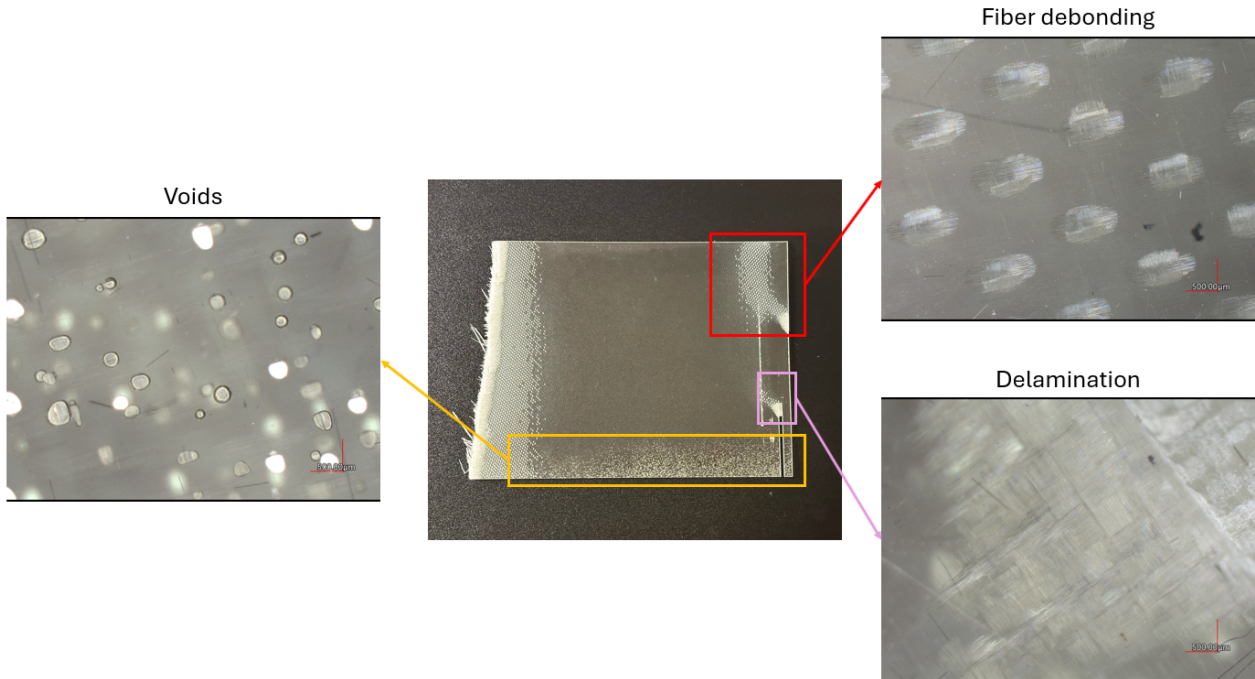


Figure 5.23: Microscopy results of the TGFRP sample showing different failure modes.

Thus, it can be said that transparency allows for easy visual detection of various failure modes without the need for expensive or specialized equipment. Another common failure mode is matrix cracking. While the damaged TGFRP in [Figure 5.23](#) does not show visible matrix cracking, it was observed during preliminary tensile testing that cracks in the matrix occur, resulting in a loss of transparency in the TGFRP sample after testing. This will be described in more detail in the following chapter.

Chapter 6

Results and Discussion: Applications of TGFRPs in Damage and Stress Analysis

6.1 Mechanical testing

Mechanical tensile testing measurements were conducted to determine the ultimate tensile strength (UTS) of the TGFRP specimens. The specimens dimensions adhered to ASTM-D3039 standard and a strain rate of 4 mm/s was used during the experiment. From the initial experiment, it was evident that failure occurred mostly at the grips of the tensile testing machine. Therefore, end tabbing techniques with different tabbing materials were tested. This initial experiment showed that the use of aluminum tabbing material resulted in the most desirable failure location in the TGFRP tensile test specimens, as seen in [Figure 6.1](#).

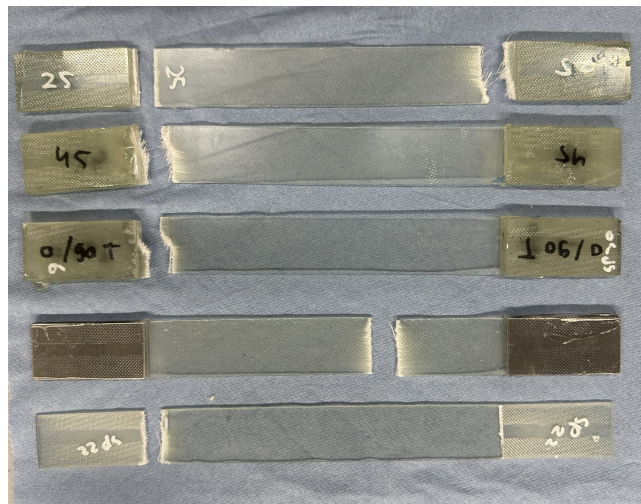


Figure 6.1: TGFRP specimens after failure in tensile testing with various end tabbing materials.

Now that it has been determined that the aluminum tabbing resulted in the most desirable failure location, the UTS of the TGFRP specimens can be measured. Five specimens were prepared for this experiment. The stress vs. strain curves of the TGFRP specimens with aluminum tabbing are presented in [Figure 6.2](#), and the ultimate tensile strength is provided in [Table 6.1](#). This results in an average tensile strength of 14.698 kN with a standard deviation of 0.339 kN.

Table 6.1: Tensile test data for TGFRP specimens.

Specimen number	Ultimate tensile strength [kN]	Average area [mm^2]
1	13.261	30.323
4	14.342	30.585
14	15.160	31.313
16	14.623	31.058
17	14.668	29.483

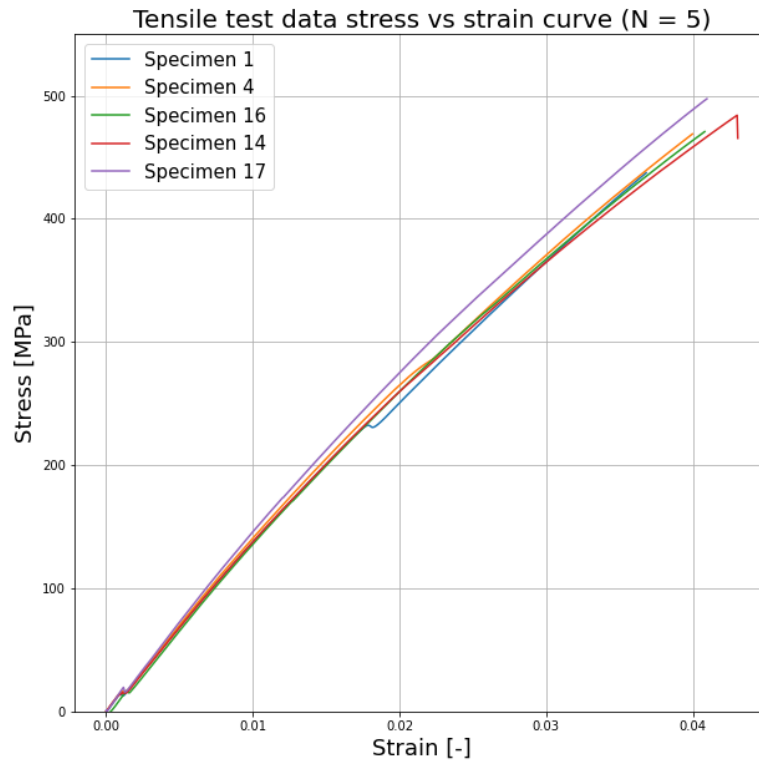


Figure 6.2: Stress vs. strain curve of the TGFRP specimens during tensile testing.

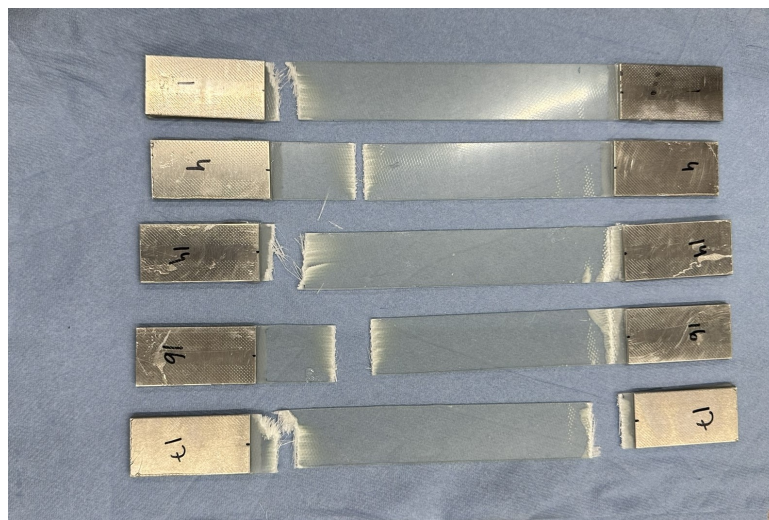
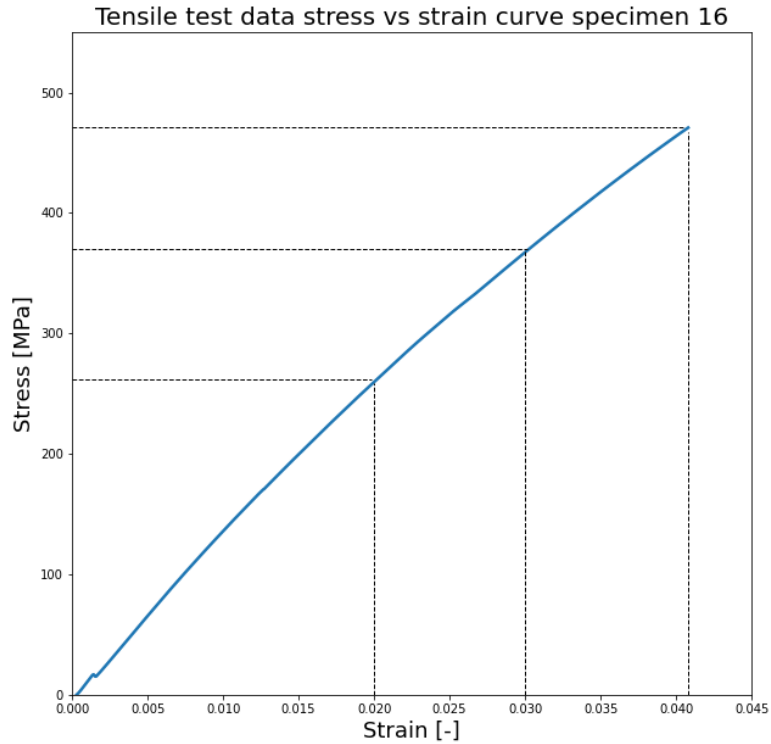
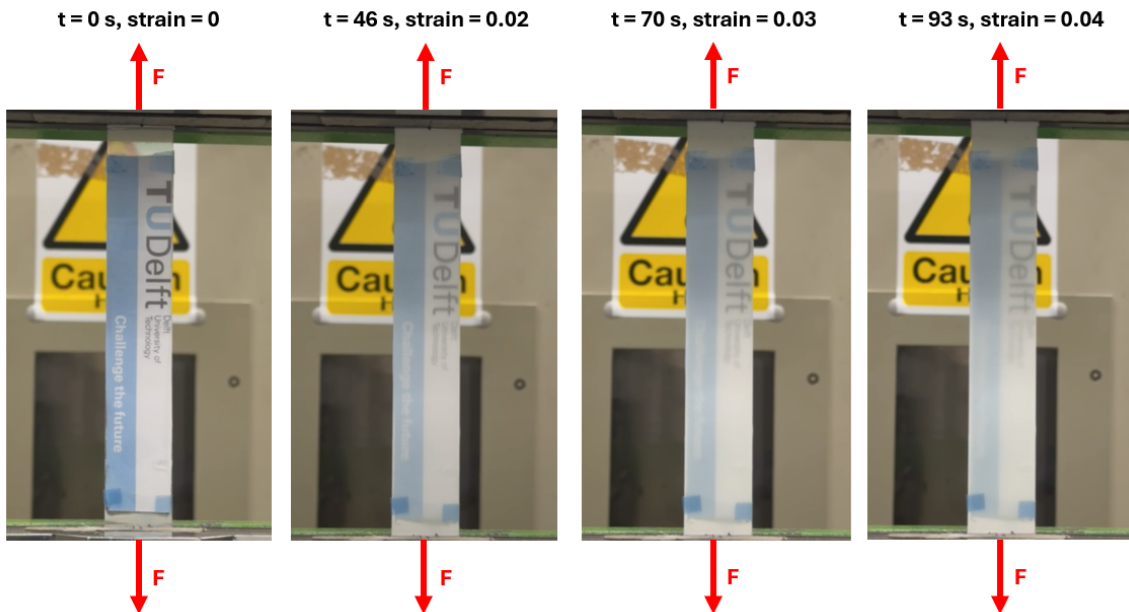


Figure 6.3: TGFRP specimens after tensile testing.

During tensile testing, an interesting observation was made. As the test progressed, the specimen became increasingly opaque as it underwent more strain. This phenomenon can be seen in Figure 6.4a and Figure 6.4b. Visually, it was detected that around $t=16$ s, corresponding to a stress of 90 MPa, the text behind the composite began to become less visible, indicating a change in the opacity of the resin. Images at different points on the stress-strain curve can be seen in Figure 6.4b.



(a) Stress vs. strain curve of specimen 16.



(b) Opacity change of specimen 16 during tensile testing.

Figure 6.4: (a) Stress vs. strain curve of specimen 16, (b) Opacity change of specimen 16 at different points in the stress vs. strain response.

From this figure, it can be observed that as the specimen undergoes more strain, the TGFRP specimen becomes less transparent. This suggests that the RI is not only a function of temperature, degree of cure, wavelength of light, and moisture content, but also of the stress that the composite material undergoes. By leveraging this phenomenon, stress could be related to the loss of transparency, providing a new method for visualizing or measuring stresses in composite materials.

6.2 Cracks in TGFRP specimens from tensile testing

Figure 6.5 shows the microscopy results of the TGFRP surface after tensile testing. In the left figure, viewed through the microscope without an aluminum plate underneath the specimen, several observations can be made. Firstly, matrix cracks can be seen forming perpendicular to the loading direction during the tensile test. Secondly, the cracks appear to concentrate in certain areas. In addition to the cracks, impurities and surface defects, such as scratches and irregularities, are also visible.

By elevating the samples with an aluminum plate and inspecting them under the microscope, larger cracks hidden beneath smaller ones become visible, as shown in the right figure. This enhanced visibility reveals that, in areas with concentrated cracking, larger cracks are present that were not noticeable in the left figure, where no aluminum plate was used.

This grouping of cracks may be explained by their initiation within the fiber tows perpendicular to the loading direction, which contribute minimally to load-bearing capacity. Small cracks form at these initiation points until larger cracks develop. At this stage, the smaller cracks close up, while the larger cracks continue to open and increase in length.

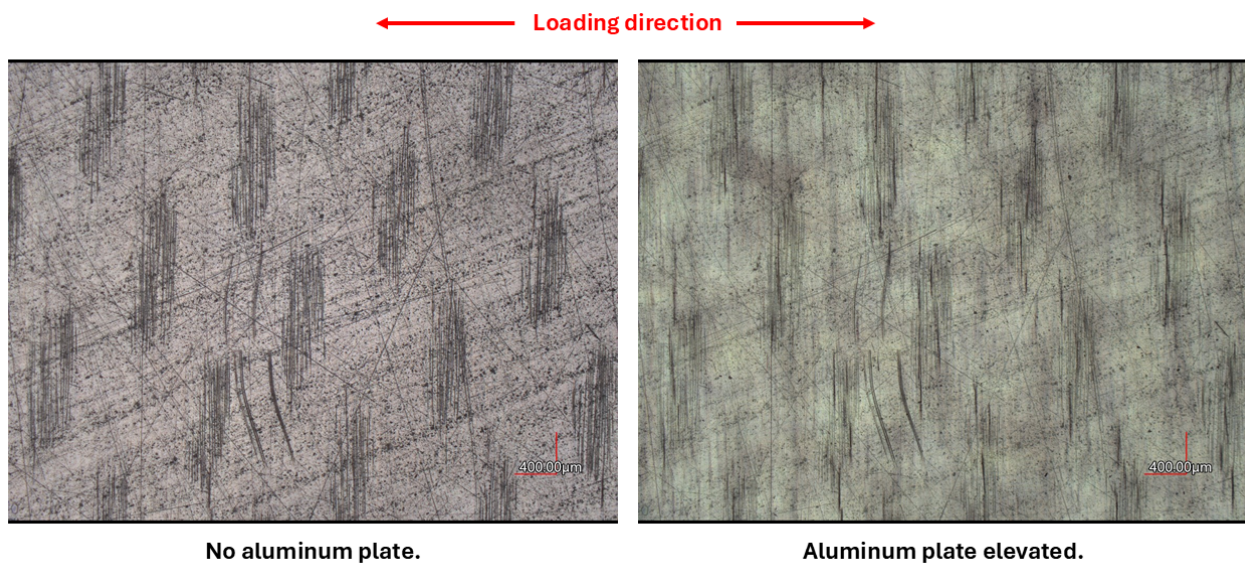


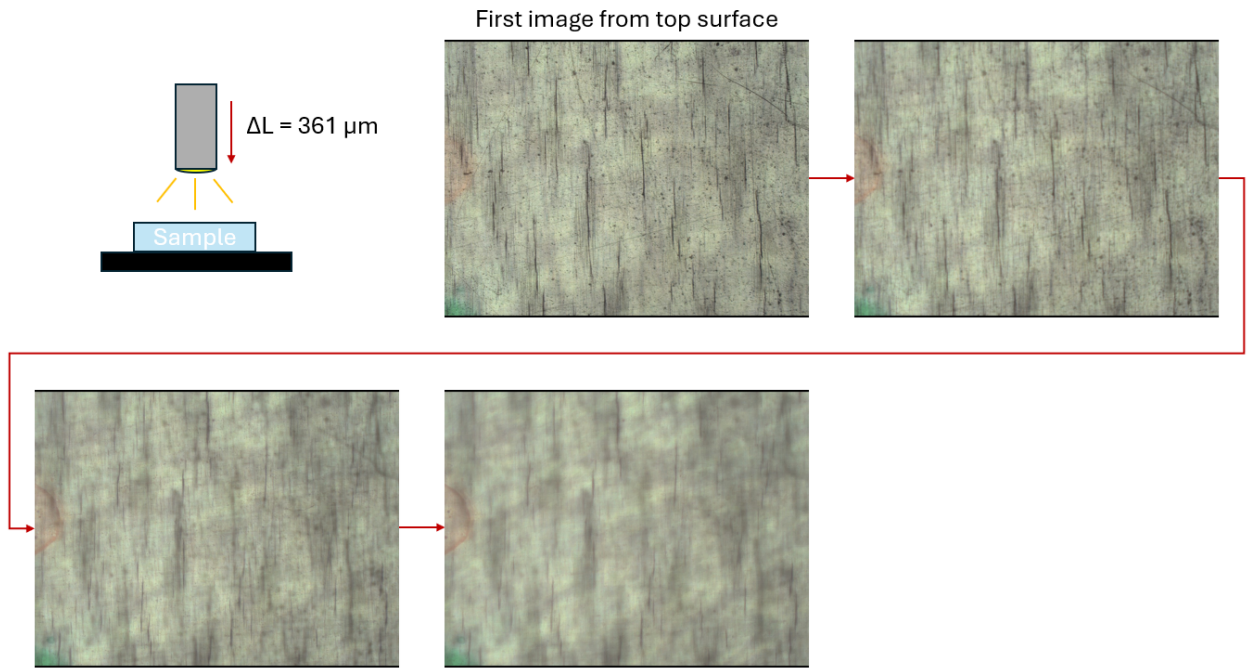
Figure 6.5: Microscopy results of cracks within the TGFRP sample after loading.

While the ability to view cracks on the surface of the composite is not uncommon, transparency could provide additional benefits. Another observation was made: when changing the focal distance of the confocal microscope, different features in the composite sample, such as cracks and impurities of varying sizes and locations, became visible. This suggests that by adjusting the focal distance, the observer may be able to see through the sample's thickness.

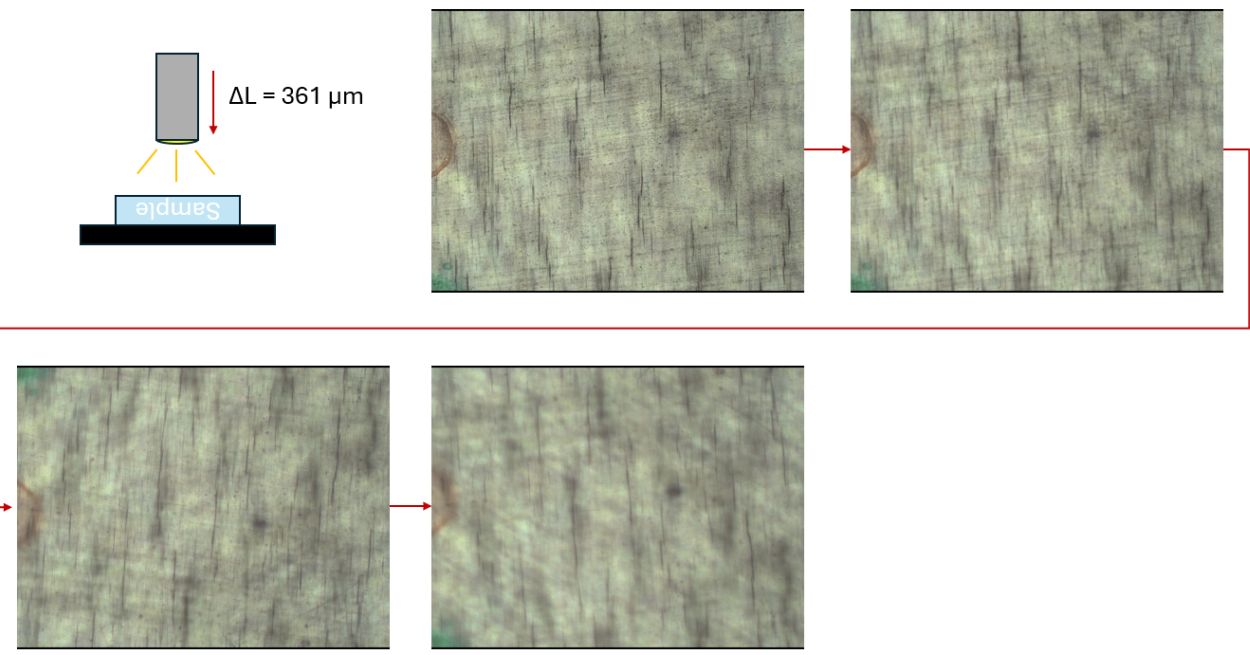
6.2.1 Through-thickness microscopy measurement

To test the hypothesis of being able to see through the thickness of the sample, two dots (orange and green) were made as reference points, as seen in [Figure 6.6a](#). In this figure, the focal distance between the lens and the sample's front surface was decreased by a constant length of $361 \mu\text{m}$. From this image, it can be observed that cracks of varying sizes and locations appear at different focal distances. Additionally, in the last image of the sequence, the brushed surface of the aluminum plate placed underneath the sample becomes visible.

The next step is to turn the sample upside down. [Figure 6.6b](#) shows the image sequence with the same varying focal distance of $361 \mu\text{m}$ between each image. The reference points (dots) were placed to ensure that the same area is visible as in [Figure 6.6a](#). In this sequence, the last image is of particular importance when compared to the first image in [Figure 6.6a](#). If these images correspond with each other, it validates the hypothesis of being able to see through the sample thickness by adjusting the focal distance between the microscope lens and the TGFRP sample.



(a) Microscope lens on top surface.



(b) Microscope lens on bottom surface.

Figure 6.6: (a) Images at varying focal distances between the lens and the top surface of the TGFRP specimen, (b) Images at varying focal distances between the lens and the bottom surface of the TGFRP specimen.

Figure 6.7 shows the comparison between the first image in the sequence of changing the focal distance from the microscope lens to the top surface and the last image in the sequence with the focal distance to the bottom surface of the sample. From this comparison, it can be observed that the cracks in both images match each other in location and size, as indicated by the colored markings in the figure. This confirms that through-thickness images of the sample can be obtained by adjusting the focal distance

between the microscope lens and the TGFRP sample.

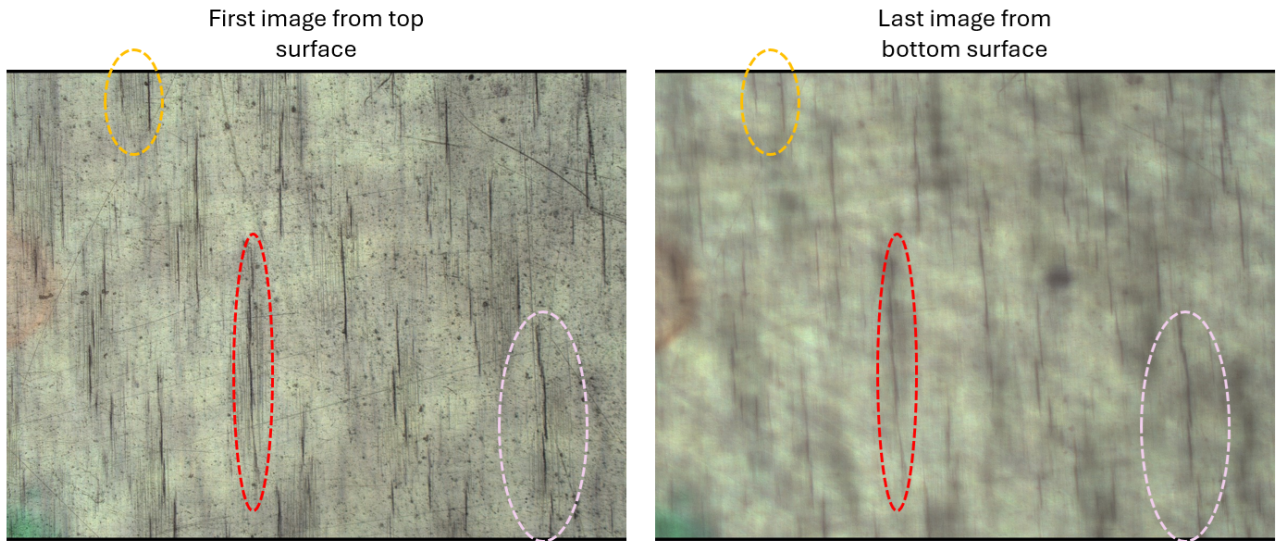


Figure 6.7: Microscope image comparison: first image of the top surface vs. last image of the bottom surface.

However, it must be noted that when we compare the sequence of images, the top surface cracks leave a dark imprint on the images later in the sequence, as seen in [Figure 6.8](#). This phenomenon can also be observed with the colored dots. Even though only the top surface features the colored dots for indication, these features also appear in a later image in the sequence (focal distance $\Delta = 902$ nm). This implies that features of the top surface influence the images of the layers below, which can be explained by the way light from the microscope travels through the sample. As the light travels from the top surface to an underlying layer, it is diminished when passing through areas where cracks are present on the top surface. The same applies to the colored dots, which allow only light of certain wavelengths to pass through to the layers below.



Figure 6.8: Microscope image comparison between the top surface and the underlying layer.

6.2.2 Crack density determination

The next investigation involves utilizing image processing to obtain the 2D crack surface density percentage in 3D space. This means that the crack density percentage will be calculated for each layer to estimate the density in 3D space by utilizing the transparency and the ability of the confocal microscope to see through the layers.

Tensile testing was conducted using different maximum loading conditions. Transmission measurements were performed for each of these samples using a spectrophotometer, as shown in [Figure 6.9](#). The MAT, along with the average wavelength at which the peak values occur and their standard deviations, are provided in [Table 6.2](#).

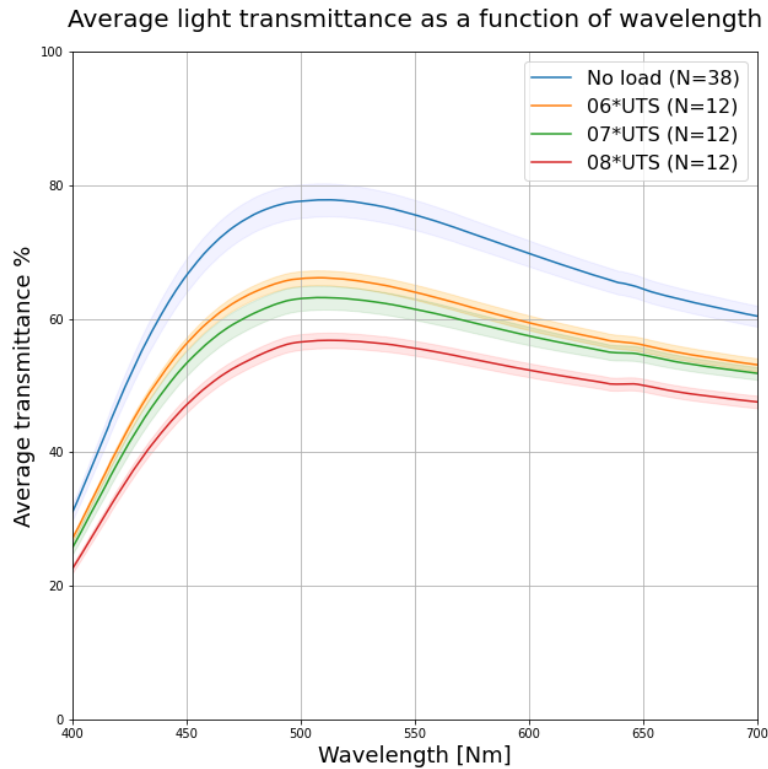


Figure 6.9: Light transmission curves for samples with different loading conditions.

Table 6.2: Transmission data for TGFRP samples subjected to different loading conditions.

Conditions	MAT [%]	SD [%]	Wavelength (MAT) [nm]	SD [nm]
No loading	77.840	2.466	510.842	2.153
0.6*UTS	66.163	1.110	507.25	1.096
0.7*UTS	63.203	1.789	509.567	2.489
0.8*UTS	56.788	1.152	512.850	2.224

From [Figure 6.9](#) and [Table 6.2](#), it can be observed that while the wavelength at which the MAT occurs does not change significantly, increasing the maximum load during tensile testing results in reduced light transmittance across all wavelengths. This is likely due to the formation of more crack initiation points and increased crack propagation at higher loads, which reduces the amount of light passing through the sample. Another possible explanation is the increased plastic deformation around the cracks, which decreases the transparency of the samples.

To confirm the hypothesis that increased crack density results in decreased light transmission across all

wavelengths in the visible range, image thresholding has been employed to determine the crack density. The image processing flowchart is shown in Figure 6.10. First, the image is converted to grayscale, followed by the application of Gaussian filtering to blur and smooth the image, reducing noise. The image is then converted into a binary form using thresholding and cleaned to remove impurities. Finally, pixel counting is used to estimate the number of crack pixels, which is then converted into a crack density percentage.

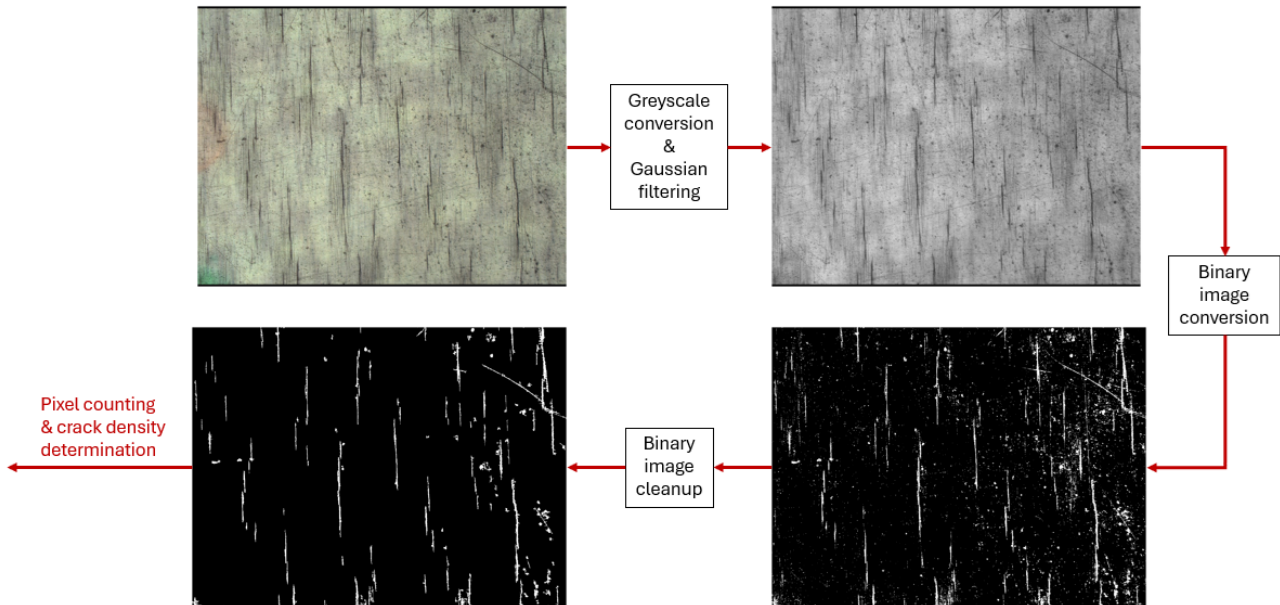


Figure 6.10: Flow chart for crack density determination.

Figure 6.11 shows the cleaned binary image overlaid on top of the original image. Parameters such as the standard deviation of the Gaussian filter, the thresholding value, and the pixel size for impurity removal have been optimized to ensure accurate crack detection in the image. As seen in this image, the crack detection script performs reasonably well, successfully identifying the most noticeable cracks.

However, limitations still persist, such as the inability to detect closed-up cracks. The thresholding can be increased to identify these, but doing so may cause the program to confuse cracks with surface scratches, leading to an overestimation of crack density. Furthermore, as observed in the figure, while most impurities have been filtered out using the Gaussian filter, some still remain.

Two methods can be employed to counteract this phenomenon: increasing the standard deviation of the Gaussian filter or increasing the pixel size of objects to be removed. However, adjusting these parameters may result in some cracks not being registered, and it has been decided that the presence of these impurities promotes a conservative approach.



Figure 6.11: Image processing for crack detection: cleaned binary image overlaid on the original image.

Even though the crack detection is not perfect, the image processing script provides a good relative difference in crack density for specimens subjected to different maximum loading conditions, as all parameters in the image processing script are kept the same. Table 6.3 shows the calculated average crack density as a percentage of the top surfaces. For each loading specimen, two different samples were investigated, with images obtained from two different measurement points in each sample.

Table 6.3: Calculated crack density per specimen under different maximum loading conditions.

Loading condition [kN]	Average crack density [%]
0.6*UTS	1.88
0.7*UTS	2.27
0.8*UTS	3.01

Referring back to Figure 6.9, it was observed that increasing the maximum load during tensile testing results in reduced light transmittance across all wavelengths, possibly due to the increase in crack density. From Table 6.3, it is evident that crack density increases with increasing load, confirming the hypothesis that increased crack density leads to decreased light transmission across all wavelengths in the visible range.

Apart from the previously mentioned limitations in the image processing method, such as the inability to detect closed cracks, distinguish deep scratches from cracks, and filter out all impurities, another problem arises when attempting to detect cracks in layers below the top surface of the sample. Figure 6.12 shows a layer deeper in the sequence, where the lens of the microscope has been lowered 1083 μm from the top surface.

As observed earlier in Figure 6.8, cracks and deep scratches on the top surface of the sample can create dark imprints on the layers below due to diminished light transmission. When attempting to detect

cracks using the thresholding technique in the layers below the top surface, as shown in [Figure 6.12](#), the dark areas are also registered. Even reducing the threshold is insufficient to overcome this limitation, resulting in an overestimation of the crack density.

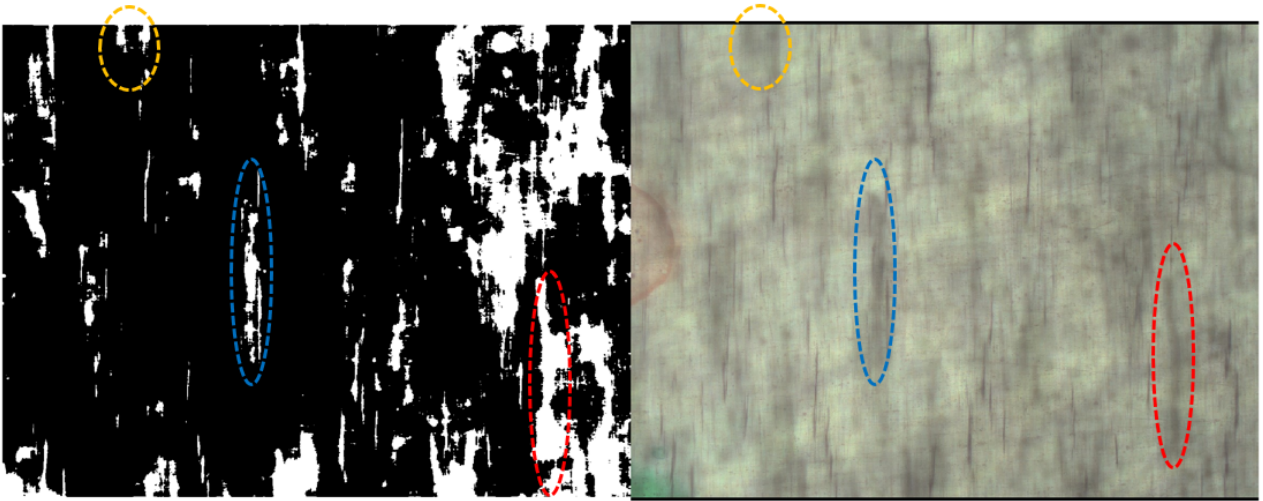
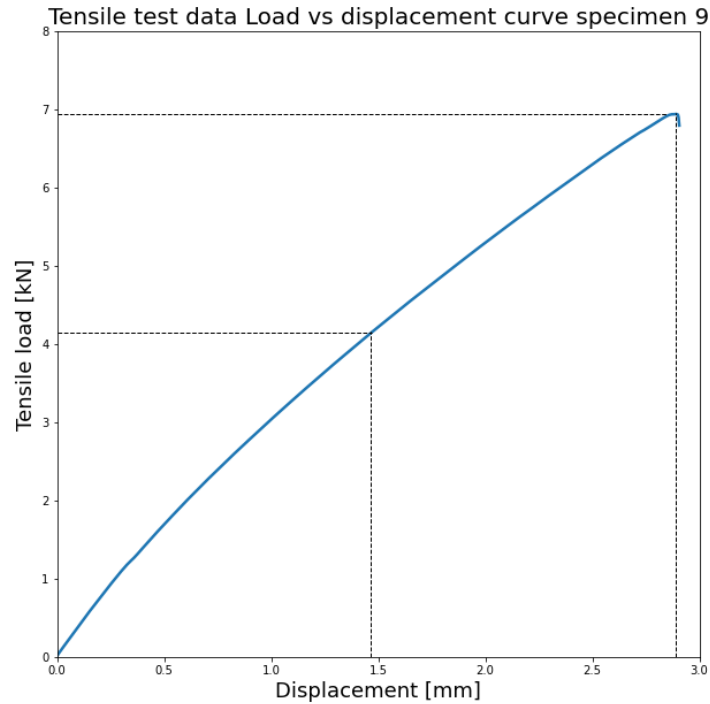


Figure 6.12: Limitations of thresholding due to dark imprints on the top surface of the sample.

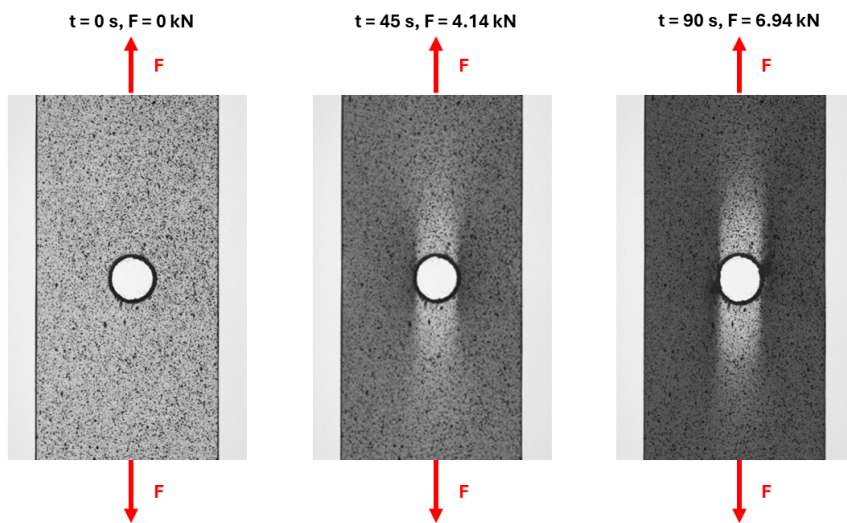
6.3 Opacity change

6.3.1 TGFRP sample

As previously shown in Figure 6.4, the specimen under loading undergoes a change in opacity. However, with a standard tensile specimen, this opacity change occurs gradually throughout the entire specimen. A more interesting scenario is the open-hole tensile specimen, where stress concentrations are expected. Therefore, to better correlate opacity change with localized stress, this experiment focuses on loading the open-hole tensile specimens, each with five layers of glass fiber fabric. Figure 6.13 shows the opacity change in open-hole specimen 9 during loading.



(a) Load vs displacement curve of open-hole specimen 9.



(b) Opacity change of open-hole specimen 9 during tensile testing.

Figure 6.13: (a) Load versus displacement curve for open-hole specimen 9 during tensile testing. (b) Opacity changes in open-hole specimen 9 at different points along the load versus displacement curve.

From Figure 6.13, it can be observed that certain regions become darker compared to others during loading, indicating an opacity change due to reduced light transmission. Notably, the first opacity change occurs along the loading direction at the edge of the hole, which is expected, as stresses must flow around the hole, creating a stress concentration at the edges. Additionally, differences in opacity are observed between the areas directly above and below the hole, as well as between the regions to the right and left, as shown in Figure 6.13b. This suggests that the intensity of the opacity change is indeed a function of the local stress in the material. Figure 6.14 confirms this hypothesis: lighter areas correspond to regions of lower strain in the DIC strain pattern, while darker areas correspond to regions of higher strain.

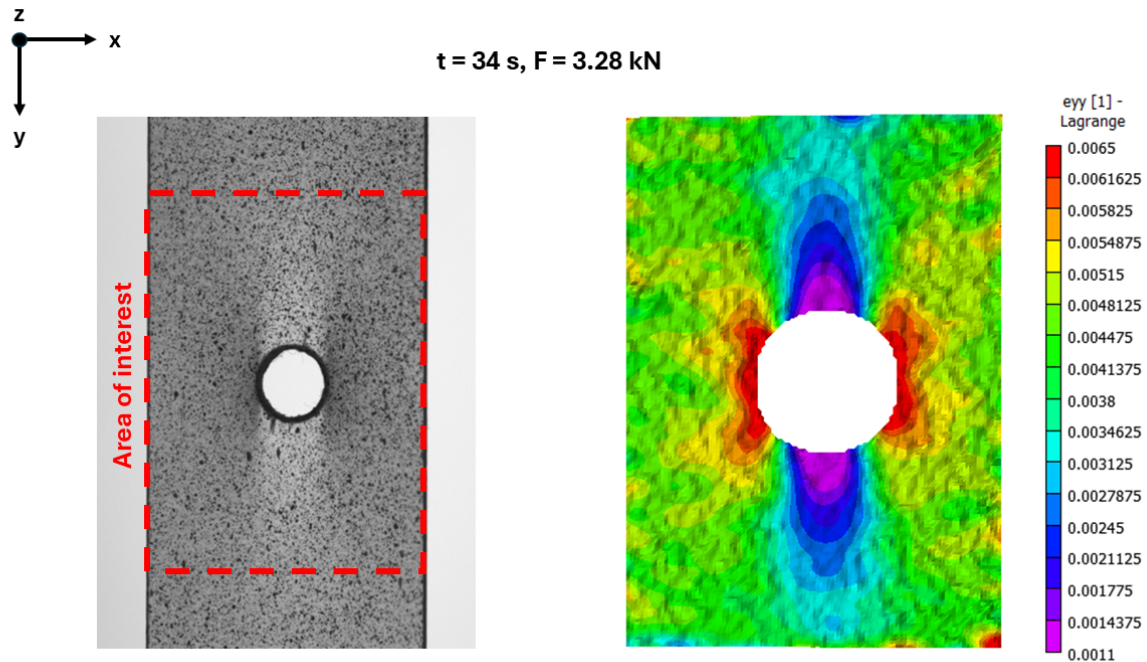


Figure 6.14: Opacity change of open-hole specimen 9 during loading compared to the strain pattern obtained from DIC at $t=34$ s.

The next step in correlating the opacity change with the strain field is quantification. For this purpose, the captured DIC images are converted into grayscale images, from which a histogram can be generated to show the pixel count for each gray level intensity. The gray level of each pixel should correspond to the intensity of the opacity change. If the opacity increases, less light will pass through, resulting in darker areas and an increase in pixel count for lower gray level values.

Figure 6.15 shows the grayscale histogram curve for open-hole specimen 9 under loading at different times. From this figure, it can be observed that the grayscale curves change during the loading of the sample. More notably, the pixel count for lower gray levels increases, while the pixel count for higher gray levels decreases as the specimen is loaded. This is in line with expectations, as the regions become darker the more the sample is loaded. Utilizing this information, it is possible to determine, in conjunction with the DIC strain pattern, at which strain value the opacity change initiates in the specimen.

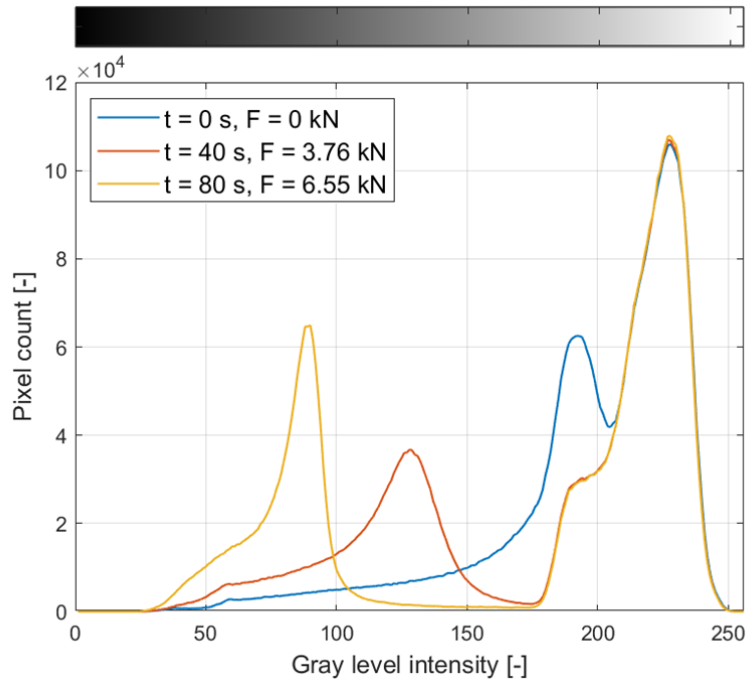


Figure 6.15: Grayscale histogram of open-hole specimen 9 under loading at different time intervals ($t=0$ s, $t=40$ s, and $t=80$ s).

Figure 6.16 shows the grayscale histogram curves for open-hole specimen 9 under loading, between $t=10$ s and $t=18$ s, with a time step of 2 seconds. From Figure 6.16b, it can be observed that the first significant decrease in gray intensity, around a value of 190, begins at approximately 14 s, corresponding to a tensile load of 1.49 kN, as shown in Figure 6.13a. In the DIC strain pattern, this corresponds to a maximum strain of 2.58×10^{-3} with an average noise of 3.97×10^{-5} . The noise is computed using the strain observed in the DIC strain pattern at the measurement point from 10 images before tensile loading is applied to the specimen.

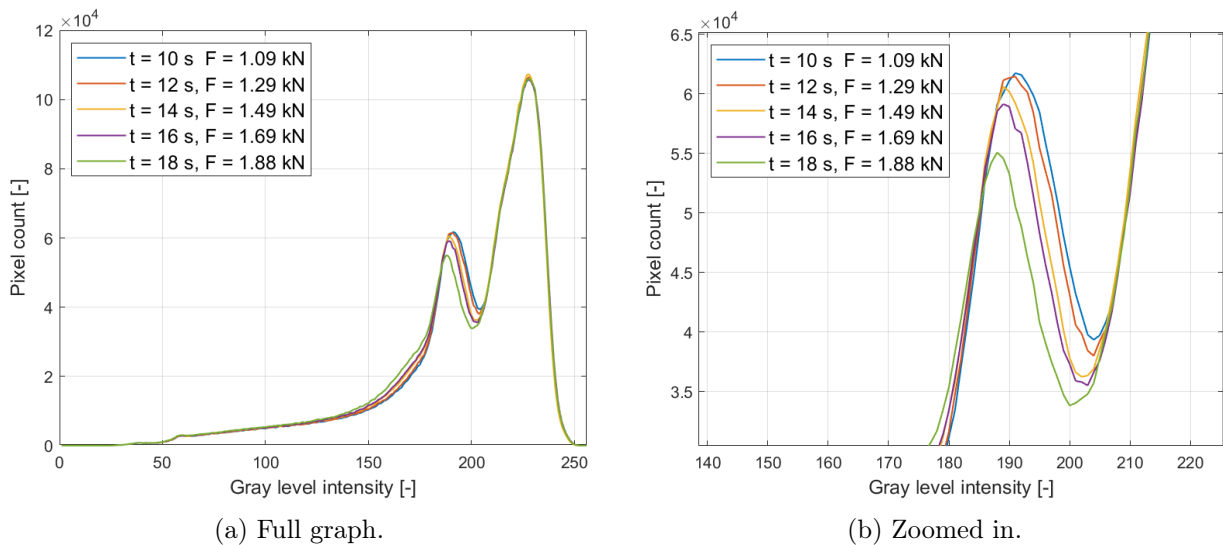


Figure 6.16: Grayscale histogram of open-hole specimen 9 under loading at different time intervals ($t=10$ s up to $t=18$ s).

Table 6.4 presents the time and corresponding maximum strains for each tested specimen, as determined from the DIC pattern, where opacity changes initiate. As shown, the associated noise are minimal, at two orders of magnitude lower than the reported strain values. From these values, an average strain of 2.13×10^{-3} is calculated at which opacity change initiates.

Table 6.4: Calculated strain at which the opacity change initiates.

Specimen number [-]	Time of opacity change [s]	Tensile load [kN]	Maximum strain [-]	Noise [-]
9	14	1.49	2.58×10^{-3}	3.97×10^{-5}
8	14	1.54	2.29×10^{-3}	4.74×10^{-5}
5	12	1.24	2.13×10^{-3}	6.49×10^{-5}
4	12	1.32	2.10×10^{-3}	4.54×10^{-5}
3	10	1.13	1.56×10^{-3}	7.32×10^{-5}

6.3.2 Photoelasticity

Another interesting phenomenon is photoelasticity, in which fringe patterns appear when a specimen under stress is viewed through polarized filters. Figure 6.17 shows the fringe pattern observed via photoelasticity alongside the opacity change pattern and DIC pattern at $t=34$ s. From this figure, it can be seen that the fringe patterns occur at the locations where the strains and stresses are highest.

Figure 6.18 shows the fringe pattern over a larger time frame, from $t=10$ s until $t=88$ s. From here, it can be seen that the fringe pattern begins to resemble the strain pattern at $t=10$ s. However, after reaching a certain threshold around $t=20$ s, the vertical fringe bands at the sides of the hole start to compress, while fringe patterns continue forming along the hole's edge. This results in multiple vertical fringe bands directly on top of and at the bottom of the hole at $t=30$ s, resembling the stress flow around the hole, although this is an assumption.

At a later time ($t=88$ s), the sides of the hole reach a certain opacity, reducing the visibility of the fringe patterns at the edges. The regions on top and bottom of the hole remain transparent due to low stresses, allowing the fringe patterns to stay visible until the specimen's failure.

While the fringe pattern initially aligns with the DIC strain pattern, with bands appearing in highly stressed regions and an absence of fringe patterns in the low-strain areas directly above and below the hole, it begins to deviate over time. Multiple fringe patterns start to emerge in the lower-stressed regions above and below the hole. This observation suggests that the fringe patterns may reflect a more complex phenomenon, involving stresses from multiple directions. Consequently, focusing only on the DIC strain pattern in the y-direction may be insufficient for accurately correlating strain with the photoelastic fringe bands.

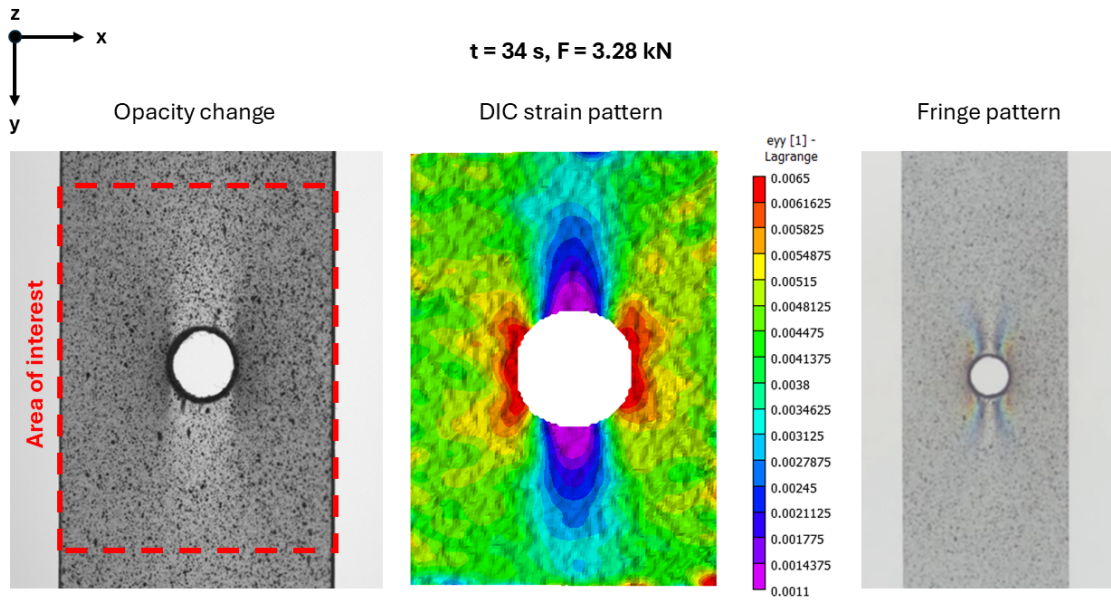


Figure 6.17: Opacity change, DIC strain pattern, and photoelastic fringe pattern comparison.

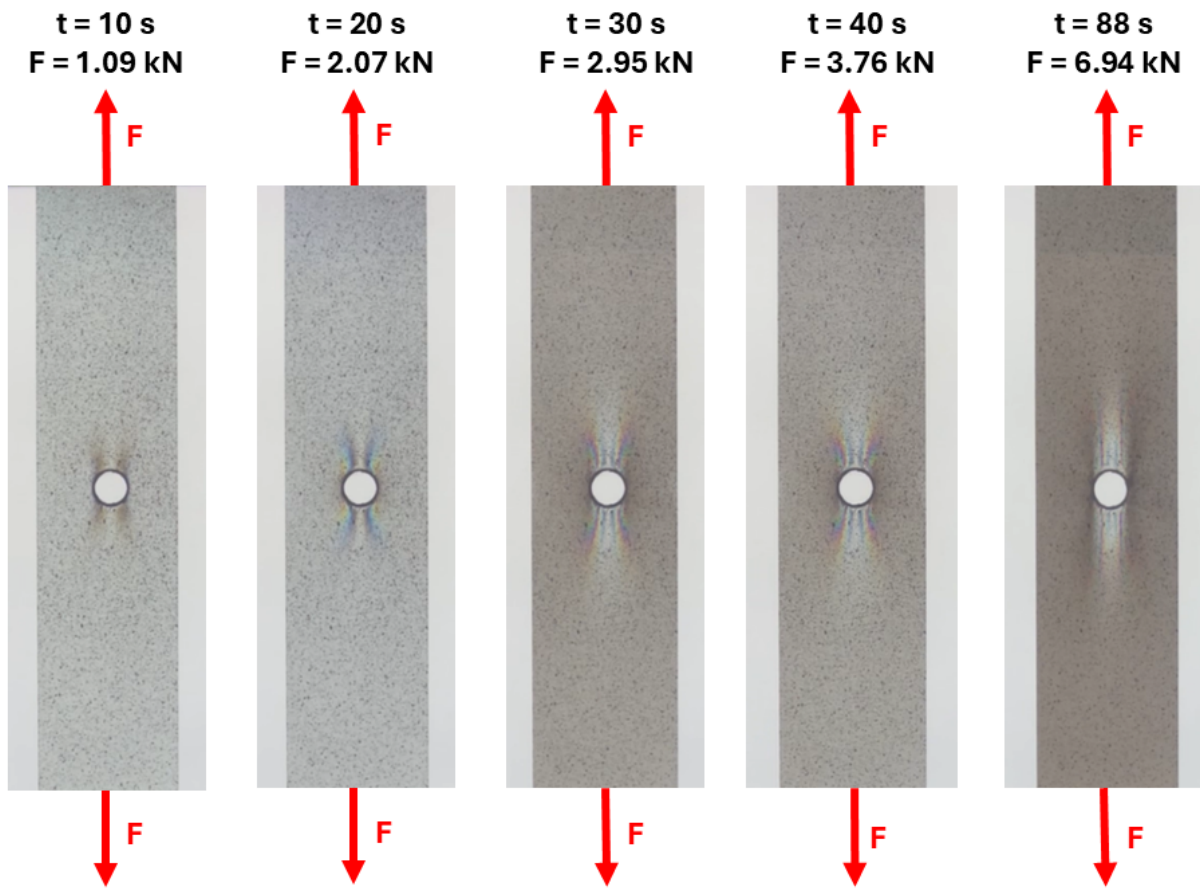


Figure 6.18: Photoelasticity images of the TGFRP sample under testing.

6.3.3 Reversibility of transparency

Another phenomenon observed during the mechanical testing of the specimens is the reversibility of transparency, where the opacity of the specimen reverts to transparent after loading. This effect may be due to the RI being a function of stress and therefore reversible. Alternatively, it could be caused by cracks that open up during the opacity transition and close during the return to transparency. [Figure 6.19](#) shows an open-hole specimen loaded up to 6 kN and unloaded before failure. It can be observed that regions of the specimen revert to transparent, while areas with high strain/stress near the edges of the hole remain opaque.

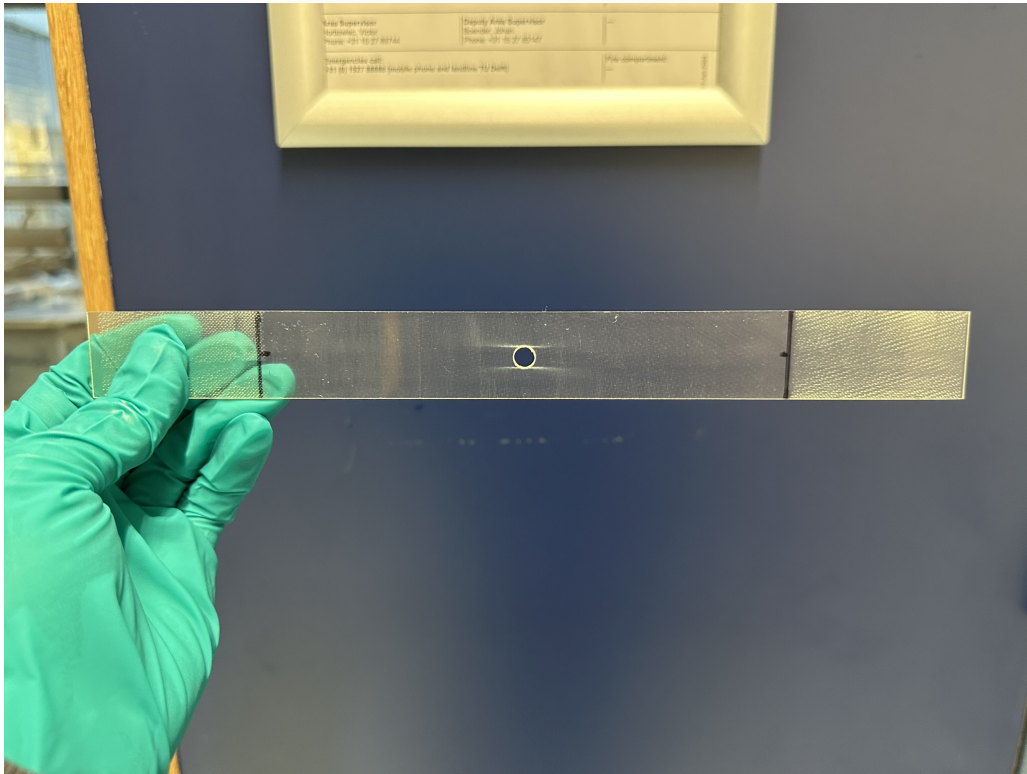


Figure 6.19: Tensile testing of the open-hole specimen up to 6 kN (before failure).

To further investigate this, microscopy images are provided for an area exhibiting irreversible opacity change near the edge of the hole (see [Figure 6.19](#)). [Figure 6.20a](#) shows the microscope image of the top surface, [Figure 6.20b](#) shows the bottom surface, and [Figure 6.21](#) shows the region between the top and bottom surfaces by changing the focal distance between the microscope lens and the specimen surface.

In these figures, numerous cracks and scratches can be seen in the loading direction and parallel to it. Particularly in [Figure 6.21](#), vertical cracks are noticeable, contributing to the irreversible opacity change. However, these vertical cracks are not observed on the top or bottom surfaces in [Figure 6.20](#).

This observation also highlights the advantage of transparency characteristics. Transparency not only allows for viewing cracks on the opposite side, as demonstrated in [Figure 6.6](#), but also enables the detection of cracks between surfaces. Other parts of the open-hole specimen were also investigated, showing minimal cracking, which supports the conclusion that irreversible opacity change is indeed caused by cracks in regions of high strain/stress.



(a) Top surface.



(b) Bottom surface.

Figure 6.20: Microscopy images of the open-hole specimen after loading to 6 kN (before failure).

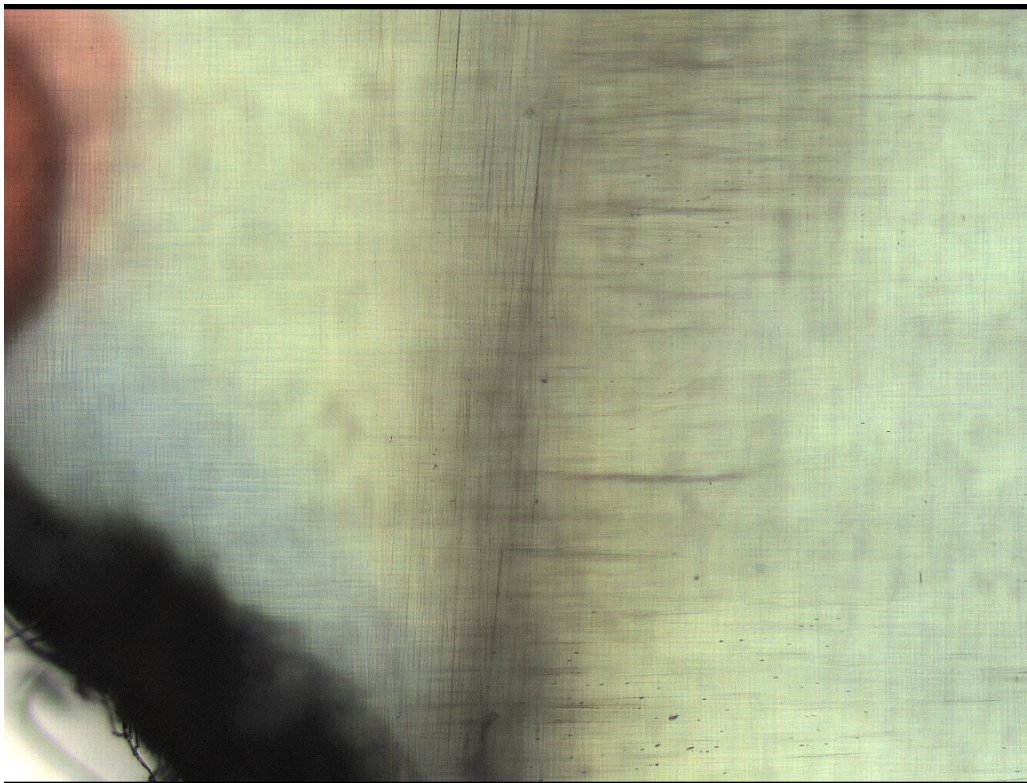


Figure 6.21: Microscopy images of the open-hole specimen after loading up to 6 kN (before failure), showing the region between the top and bottom surfaces.

6.3.4 Pure resin samples

Pure resin samples with thicknesses similar to the TGFRP samples were also prepared to determine whether opacity changes occur in the absence of glass fibers. [Figure 6.22](#) shows captured DIC images of the open-hole resin sample during loading. This figure illustrates that the opacity does not vary under increasing tensile load, in contrast to the TGFRP sample shown in [Figure 6.13](#). This observation suggests that the opacity change is associated with the presence of glass fibers, potentially due to the formation of micro-cracks or an increase in the RI mismatch between the glass fibers and the resin.

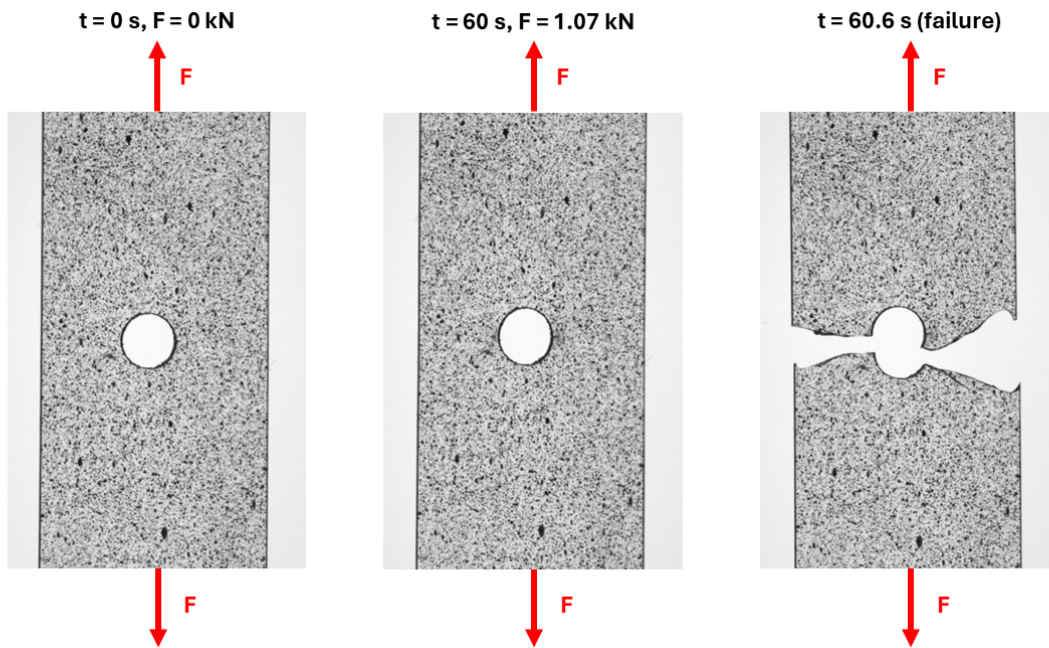


Figure 6.22: DIC images of pure resin sample 2 captured during loading at different time intervals.

The absence of opacity change is confirmed by the gray level curves shown in Figure 6.23. This figure demonstrates that, for the pure resin sample at a time and load just before failure ($t=60$ s and $F=1.07$ kN), the grayscale curve remains consistent with the grayscale curve of the resin sample at $t=0$ s, before any loading was applied.

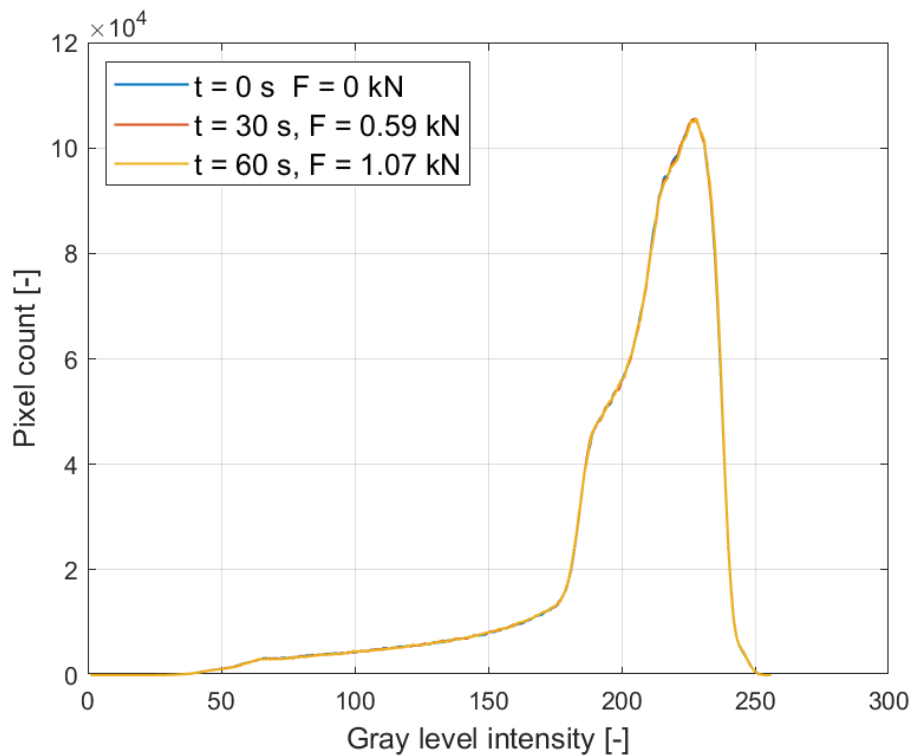


Figure 6.23: Grayscale histogram of open-hole resin specimen 2 under loading at different time intervals ($t=0$ s, $t=30$ s, and $t=60$ s).

An interesting observation can be made from the photoelasticity images taken after failure, as shown in [Figure 6.24](#). These images reveal that, after failure, stresses in the pure resin sample are fully released, whereas residual stresses remain in the TGFRP sample. The residual stresses in the TGFRP sample are likely caused by the mismatch in elastic behavior between the resin and the glass fibers.

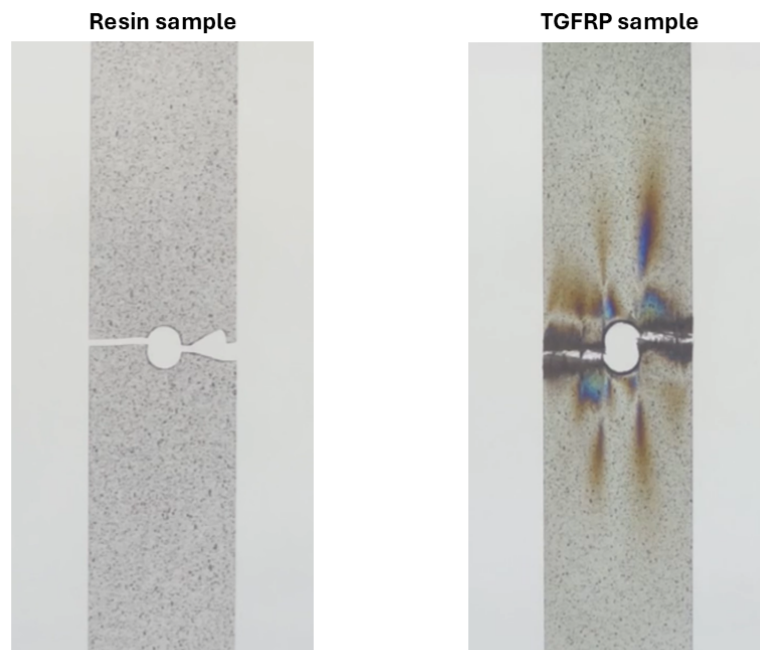


Figure 6.24: Photoelasticity images comparing the pure resin sample to the TGFRP sample.

Chapter 7

Conclusions

Since the beginning of this project, the goal was to manufacture transparent glass fiber-reinforced polymers (TGFRPs) and to understand the manufacturing parameters and material selection/modification that influence transparency. Additionally, this study explores how to utilize this transparency to visualize and detect failures, damage, and stresses in TGFRPs. Therefore, the main research question formulated at the beginning of this project was:

How can the transparency of glass fiber-reinforced polymers be controlled or optimized by modifying manufacturing parameters, and in what ways can this transparency aid in stress and failure analysis?

To answer this question, it has been subdivided into several sub-questions. In this chapter, answers to each of these sub-questions are presented. Finally, based on these answers, a conclusion to the main research question will be formulated and presented.

7.1 Answers to sub-questions

Sub-question 1

What optical tests and equipment are available for characterizing the transparency of TGFRP samples?

During the measurement of the refractive index (RI) of the fully cured epoxy resin and hardener mixture using the Abbe refractometer at 589 nm, the addition of MMA resulted in negligible differences in RIs, which could also be attributed to sample variations. However, when creating the GFRP panels with varying MMA percentages by weight, noticeable differences could be observed regarding transparency. Since the manufacturing parameters remained the same for all panels, the drastic change in visible transparency implies that the RI of the epoxy resin and hardener mixture with methyl methacrylate (MMA) should have changed significantly.

This leads to the conclusion that the measurement at 589 nm using the Abbe refractometer for solid samples might not be sufficient for optimizing the transparency of TGFRP samples. Therefore, it can be concluded that a different method, where the optical properties can be measured across a range of wavelengths, should be used, such as a spectrophotometer. This highlights the importance of knowing the optical properties across an entire wavelength range for the manufacturing and optimization of TGFRPs.

Sub-question 2

Which manufacturing methods and parameters minimize void formation while maximizing fiber impregnation and transparency?

Due to the use of low-viscosity resin in liquid molding processes (LMP), combined with a pressure differential, the resin is effectively transferred through the fibers in its low-viscosity form, allowing air molecules and impurities to be expelled from the assembly. It was also observed that molds with high surface quality on both sides are essential for achieving high transparency. Therefore, it can be concluded that LMP, such as resin transfer molding (RTM) or a modified vacuum infusion process (VIP) with an additional caul plate between the fibers and the vacuum bag, are the most suitable manufacturing methods for TGFRPs. Depending on the viscosity of the resin and hardener mixture, the internal pressure may need to be adjusted to prevent excessive infusion speeds, which can trap air instead of expelling it.

The experiment, in which TGFRP samples were manufactured using plates with different surface finishes, showed that the use of top and bottom caul plates with varying surface qualities significantly influenced the transparency of the TGFRP samples. Lower surface quality promotes greater light scattering on the sample surface, leading to reduced transparency. This finding underscores the importance of selecting molds with high-quality surface finishes to optimize the optical properties of TGFRP materials.

Finally, the post-curing temperature experiment demonstrated that increasing the post-curing temperature results in a decrease in the transparency of TGFRP samples. This loss in transparency is reflected in the transmission curves, which show that the wavelength at which the maximum average transmittance (MAT) occurs shifts to shorter wavelengths with higher temperatures. The slight differences in MAT suggest that the wavelength of the MAT has a significant impact on transparency.

Compared to the findings from the MMA variation experiment, it can be concluded that post-curing TGFRP samples is a more controlled method than using MMA. Post-curing results in minimal loss in MAT while significantly shifting the wavelengths at which the MAT occurs. These findings emphasize the importance of optimizing post-curing conditions in the manufacturing process to enhance the optical properties of TGFRPs.

Sub-question 3

How do the number of woven glass fiber layers and the sizing on the glass fibers affect the transparency of the TGFRP?

In conclusion, the experiment with varying numbers of woven glass fiber fabric layers demonstrated that as the number of layers increases, the transparency of TGFRP samples decreases. Although the MAT decreases only slightly with additional layers, noticeable differences in transparency can be observed through visual inspection. This indicates that other factors may influence transparency more significantly than the MAT alone suggests.

Furthermore, the transmission curves show that the wavelength at which the MAT occurs shifts to the left with increasing layers, likely contributing to the loss of transparency. These findings underscore the importance of considering layer composition when high transparency is a key requirement.

Sizing has also been shown to significantly impact the transparency of TGFRPs. Removal of the sizing at elevated temperatures caused a shift in the MAT wavelength to the blue color range, primarily by changing the RI of the glass fibers. This shift gives the samples a distinct blue tint, similar to post-cured samples at 60°C. However, the reduced effectiveness of the sizing is apparent under the

confocal microscope, where cross-shaped marks resembling inadequately infiltrated glass fibers, as well as visible glass fibers, can be observed.

Initially, it was assumed that the visible glass fibers in the TGFRP sample without sizing were due to exposed fibers. However, it has now been confirmed that these visible fibers result from cracks in the fiber bundles near the surface of the TGFRP panel, resembling fiber debonding. These findings highlight the importance of sizing when high infiltration quality and proper bonding between the fibers and matrix are required for manufacturing TGFRPs.

Sub-question 4

What testing methods and parameters can be used to create visible damage within the composite without causing complete failure?

Mechanical tensile testing demonstrated that microcracks perpendicular to the loading direction can be created, while delamination and fiber debonding were only visible with complete tensile failure. An incident involving a TGFRP panel, which bent like a cantilever beam with two fixed ends during cutting, revealed delamination and fiber debonding. Therefore, it can be concluded that tensile testing is optimal for creating microcracks, while three-point bending tests are more suitable for assessing fiber debonding and delamination. The ability to create specific failure modes in the composite could aid in exploring methods to identify, visualize, and analyze these failure modes by utilizing the transparency characteristics of the TGFRP samples.

Sub-question 5

What measurement equipment is available for visualizing damage and stresses within the composite?

In conclusion, the inspection of TGFRP samples using confocal microscopy revealed that altering the focal distance allows for visualization of cracks at various depths, not just on the surface. However, this method has limitations, such as the difficulty in visualizing cracks in lower layers due to dark imprints from cracks in the top layers. Image processing techniques, such as thresholding, were shown to be effective. These techniques were employed to calculate crack density and correlated higher crack density with reduced light transmittance across the visible range. However, detecting closed microcracks remained challenging due to the presence of impurities.

Tensile testing of open-hole specimens demonstrated a significant opacity change in areas with high stress concentration, confirming that opacity change correlates with local stress in the material. The strain pattern obtained from DIC and the grayscale histograms provided insight into the strain value at which opacity changes initiate. Furthermore, photoelastic fringe patterns aligned with DIC strain patterns in the early stages but began to deviate as loading progressed, suggesting that the fringe patterns reflect a more complex stress phenomenon involving multiple directions. This indicates that a comprehensive approach, considering strain in multiple directions, is necessary to accurately correlate strain with photoelastic fringe bands.

7.2 Conclusion to the main research question

Now that all the sub-questions have been answered, the final conclusion to the main research question can be formulated:

How can the transparency of glass fiber-reinforced polymers be controlled or optimized by modifying manufacturing parameters, and in what ways can this transparency aid in stress and failure analysis?

Controlling and optimizing the transparency of glass fiber-reinforced polymers (TGFRPs) begins with selecting an appropriate manufacturing method, such as resin transfer molding (RTM) or vacuum infusion processing (VIP). These methods use low-viscosity resin combined with optimal infusion pressure and speed to achieve high-quality fiber infiltration with minimal void formation. Additionally, achieving smooth, high-quality surfaces on both sides of the composite is crucial for maximizing transparency.

Measurement techniques, such as spectrophotometry, allow for assessment of transmission across the visible spectrum (400–700 nm). Although maximum average transmittance (MAT) is often cited as a transparency measure, the wavelength at which MAT occurs significantly impacts transparency, as small differences in MAT percentage are visually indistinguishable. Thus, optimizing transparency should focus on shifting the MAT wavelength into the green light spectrum (520–600 nm).

This study identified two methods for achieving this wavelength optimization: adding methyl methacrylate (MMA) to shift the MAT wavelength toward the blue light spectrum or using elevated post-curing temperatures, with the latter offering a more controlled method that minimally affects the MAT value. Additionally, sizing proved essential in enhancing transparency by promoting adequate infiltration and bonding between the matrix and glass fibers within fiber bundles. Minimizing the number of glass fiber layers is also beneficial, as adding layers generally reduces MAT across all visible wavelengths.

Beyond manufacturing and parameter optimization, this thesis explored the application potential of TGFRP transparency for visualizing internal damage and stress. Although transparent composites are commonly achieved by refractive index matching with MMA, the use of transparency as a tool for internal visualization and non-destructive inspection remains relatively unexplored in the literature.

Confocal microscopy inspections demonstrated that altering the focal distance enables visualization of cracks at various depths, not just on the surface. In combination with image processing techniques, such as thresholding, it was shown that increasing crack density in TGFRP samples reduced light transmittance across the visible range.

Tensile testing of open-hole specimens showed significant opacity changes in areas with high strain, confirming that opacity change correlates with local stress. The strain pattern from digital image correlation (DIC) and grayscale histograms offered valuable insights into the specific strain values at which opacity changes initiate.

These findings suggest that TGFRPs not only hold promise as lightweight, strong materials with desirable optical properties for applications traditionally reliant on glass or ceramics, but they could also support innovative and potentially more reliable techniques for non-destructive testing, damage detection, and stress visualization in glass fiber-reinforced polymer structures.

Chapter 8

Recommendations for Future Work

Opacity change and validating reversibility

From the experiments, it was observed that opacity changes occur due to both refractive index (RI) shifts during loading and the initiation and propagation of cracks within the material. Further exploration could leverage the strain threshold at which opacity changes occur to conduct additional mechanical tests. This would help quantify the strain values where opacity changes are exclusively attributed to RI differences between the glass fibers and the epoxy resin.

Additionally, some reversibility in opacity changes was observed in specific regions of the TGFRP samples during specimen unloading or after failure. Although qualitative, this reversibility could be validated through spectrophotometer measurements conducted post-mechanical testing. These findings could enhance the understanding of the mechanisms driving opacity changes in TGFRPs under loading.

Environmental impact

To enable TGFRPs to effectively replace current transparent materials such as glass and ceramics in real-world applications, it is crucial to further investigate the impact of environmental aging. Although the effect of high-temperature exposure has been studied in the form of post-curing, the influence of low temperatures, moisture, and humidity on the composite's transparency is worthwhile to investigate, especially given that transparent materials are often used in environments exposed to these factors.

Moreover, while UV exposure is known to degrade mechanical properties, it could also accelerate transparency loss, which would be detrimental in applications where optical clarity is essential, such as in windows, lenses, or protective barriers. Correlating the degradation of transparency with environmental factors like humidity, moisture, and UV exposure could provide valuable insights for the long-term performance and health assessment of TGFRPs.

Fatigue

Aside from environmental factors, mechanical factors also play a significant role. Fatigue is a well-known concept in engineering, characterized by damage mechanisms and phenomena initiated by repeated fluctuations of loads at stress levels below the material's failure strength. This process results in permanent changes, a loss of load-bearing capacity, and eventual failure at stress levels lower than the material's original failure strength. Early fatigue damage typically begins with microscopic defects, such as cracks, which are nearly invisible to the naked eye but can progress to sudden and catastrophic failure.

One key challenge associated with fatigue is detecting early fatigue damage without relying on non-destructive testing methods. During the testing conducted in this project to correlate crack density

with transparency loss, it was observed that as crack density increases, so does the loss of transparency in TGFRP samples. Therefore, a recommendation could be made to manufacture and prepare TGFRP samples for fatigue testing, where cyclic loading with varying amplitudes and cycles might be correlated with transparency loss. Utilizing the transparency characteristics of TGFRPs could help in the early detection of fatigue damage.

References

- Ailioaie, L., & Litscher, G. (2020, 09). Molecular and cellular mechanisms of arthritis in children and adults: New perspectives on applied photobiomodulation. *International journal of molecular sciences*, *21*. doi: 10.3390/ijms21186565
- Campbell, F. (2003). *Manufacturing processes for advanced composites*. Elsevier Science.
- Caydamli, Y., Heudorfer, K., Take, J., Podjaski, F., Middendorf, P., & Buchmeiser, M. R. (2021). Transparent fiber-reinforced composites based on a thermoset resin using liquid composite molding (lcm) techniques. *Materials*, *14*(20), 6087. doi: <https://doi.org/10.3390/ma14206087>
- Chen, X., Cheng, S., Wang, S., Wen, K., Shi, C., Zhang, J., ... Shao, J. (2023). Embedding stretchable, mesh-structured piezoresistive sensor for in-situ damage detection of glass fiber-reinforced composite. *Composites Science and Technology*, *233*, 109926. Retrieved from <https://www.sciencedirect.com/science/article/pii/S0266353823000192> doi: <https://doi.org/10.1016/j.compscitech.2023.109926>
- Fang, Z., Zhu, H., Li, Y., Liu, Z., Dai, J., Preston, C., ... Chen, G. (2014). Light management in flexible glass by wood cellulose coating. *Scientific reports*, *4*(1), 5842. doi: <https://doi.org/10.1038/srep05842>
- Hosur, M., Jeelani, S., Vaidya, U., Wosu, S., & Kelkar, A. (2003, 04). Survivability of affordable aircraft composite structures. volume 1: Overview and ballistic impact testing of affordable woven carbon/epoxy composites. , 47.
- Huang, T., Ciou, J., Huang, P., Hsieh, K., & Yang, S. (2008). Fast fabrication of integrated surface-relief and particle-diffusing plastic diffuser by use of a hybrid extrusion roller embossing process. *Optics express*, *16*(1), 440-447. doi: <https://doi.org/10.1364/oe.16.000440>
- Krug, D., Asuncion, M., Popova, V., & Laine, R. (2013). Transparent fiber glass reinforced composites. *Composites Science and Technology*, *77*, 95-100. doi: <https://doi.org/10.1016/j.compscitech.2012.12.010>
- Magrini, T., Bouville, F., & Studart, A. (2021). Transparent materials with stiff and tough hierarchical structures. *Open Ceramics*, *6*, 100109. doi: <https://doi.org/10.1016/j.oceram.2021.100109>
- Mallick, P. (2017). *Processing of polymer matrix composites*. CRC Press.
- Mat Yunus, W. M., & Rahman, A. (1988, 08). Refractive index of solutions at high concentrations. *Applied optics*, *27*, 3341-3. doi: 10.1364/AO.27.003341
- Menta, V., Vuppalapati, R., Chandrashekhara, K., & Schuman, T. (2014). Manufacturing of transparent composites using vacuum infusion process. *Polymers and Polymer Composites*, *22*(9), 843-850. doi: <https://doi.org/10.1177/096739111402200912>
- Osorio, L., Trujillo, E., Vuure, A., & Verpoest, I. (2011, 04). Morphological aspects and mechanical properties of single bamboo fibers and flexural characterization of bamboo/ epoxy composites. *Journal of Reinforced Plastics and Composites - J REINF PLAST COMPOSITE*, *30*, 396-408. doi: 10.1177/0731684410397683
- Patterson, E. (2016). *Reference module in materials science and materials engineering*. Elsevier. doi: <https://doi.org/10.1016/B978-0-12-803581-8.03530-X>
- Petersen, H. (2017). *Investigation of sizing - from glass fibre surface to composite interface* (Unpublished doctoral dissertation). Technical University of Denmark.

- Reynolds, S. (2022). *Glass for solar applications*. Retrieved 2024-03-16, from <https://www.swiftglass.com/blog/glass-for-solar-applications/#:~:text=The%20industry%20standard%20weight%20for,glass%20is%20around%2020%20kg>.
- Timmermans, G. H., Hemming, S., Baeza, E., Van Thoor, E., Schenning, A., & Debije, M. G. (2020). Advanced optical materials for sunlight control in greenhouses. *Advanced Optical Materials*, 8(18), 2000738. doi: <https://doi.org/10.1002/adom.202000738>
- Villegas, I. F. (2022). *Polymer composite manufacturing*. <https://brightspace.tudelft.nl/d21/le/content/498884/viewContent/2997471/View>. (Accessed: 2024-7-07)
- Wang, B., Zhong, S., Lee, T., Fancey, K., & Mi, J. (2020). Non-destructive testing and evaluation of composite materials/structures: A state-of-the-art review. *Advances in Mechanical Engineering*, 12. doi: 10.1177/1687814020913761
- Yang, Y., Lai, Y., Zhao, S., Chen, H., Li, R., & Wang, Y. (2024). Optically transparent and high-strength glass-fabric reinforced composite. *Composites Science and Technology*, 245, 110338. doi: <https://doi.org/10.1016/j.compscitech.2023.110338>
- Zobeiry, N., Lee, A., & Mobuchon, C. (2020). Fabrication of transparent advanced composites. *Composites Science and Technology*, 197, 108281. doi: <https://doi.org/10.1016/j.compscitech.2020.108281>

Appendix A

Modified Vacuum Infusion Process

A.1 Materials and equipment

All required materials, equipment, and quantities can be seen below:

- 2 plexiglass plate
- Marbocote 227 release agent
- Masking tape
- 5 sheets of Hexforce 7581 glass fiber
- FM 94 blue adhesive tape
- Dianet 135 flow mesh
- H014 peel ply
- Wrightlon 3900 release film
- Tacky tape
- Flexible tube
- Spiral tube
- Aceton
- Isopropanol
- T - shaped tube connector
- Breather fabric
- Vacuum bag
- Tube clamp
- Sponge
- Small clamps
- Scissor
- Safety glasses
- Gloves

- wooden mixing sticks

A.2 Vacuum assisted resin transfer molding (VARTM) process

The VARTM process for producing transparent composite panels can be divided into several phases:

Phase 1: cleaning and applying release agent

For this phase, clean the top of the large plexiglass plate with acetone and isopropanol. After cleaning, apply masking tape to the four edges of the plexiglass plate. Then, apply three layers of release agent with 5-minute intervals between applications. Finally, remove the tape from the edges of the plate. This will ensure maximum adhesive force between the plate and the vacuum bag.

The same process will be followed for the smaller plexiglass plate (caul plate), but without applying masking tape to the edges. This plate will be placed on top of the glass fibers. The entire process of cleaning and applying the release agent will be done on all surfaces of the caul plate.

Phase 2: Layup

In the second phase, remove the masking tape from the plate and replace it with tacky tape. Afterward, place the layers of glass fiber sheets in the middle of this plate. Then, place the caul plate on top of the fiber sheets. Finally, apply tacky tape to the ends of the glass fiber sheets in the transverse direction (in the direction of the resin flow), ensuring that the tape comes into contact with both the caul plate and the edges of the glass fiber sheets. This will ensure that no cavities exist when the vacuum bag is placed on top and the vacuum is applied. Otherwise, resin will flow rapidly through these channels, which could lead to entrapped air in the middle of the composite plate. The setup should resemble [Figure A.1](#).

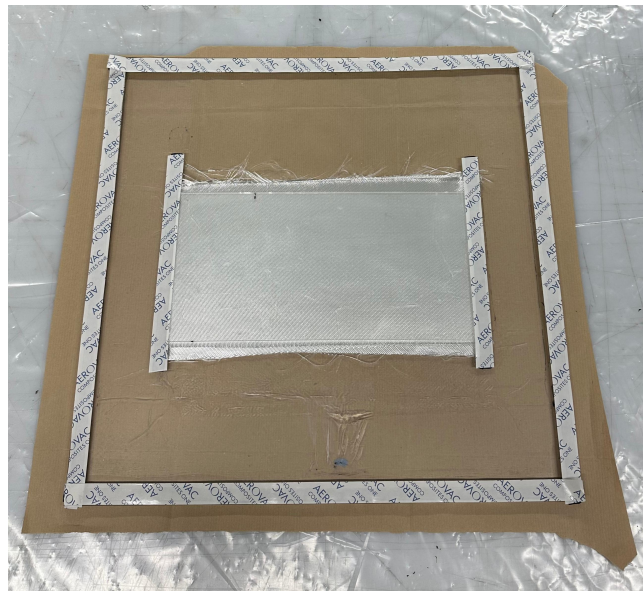


Figure A.1: Phase 2 assembly.

Phase 3: Tubing

In the third phase, connect the T-connector and the spiral tube, and wrap the ends with blue adhesive tape. Covering the spiral tube ends with adhesive tape will reduce the chances of this component puncturing the vacuum bag. Then, make a hole in the middle of the flow mesh and secure it with

staples. Again, cover the staples with blue adhesive tape to prevent them from damaging the vacuum bag. Next, attach the flexible tube to the T-connector, wrap the tube with 3 layers of tacky tape, and place it in the middle of the tacky tape at the edges of the large plate. This will serve as the inlet for the resin and hardener mixture. The assembly for the inlet tube can be seen in [Figure A.2](#).

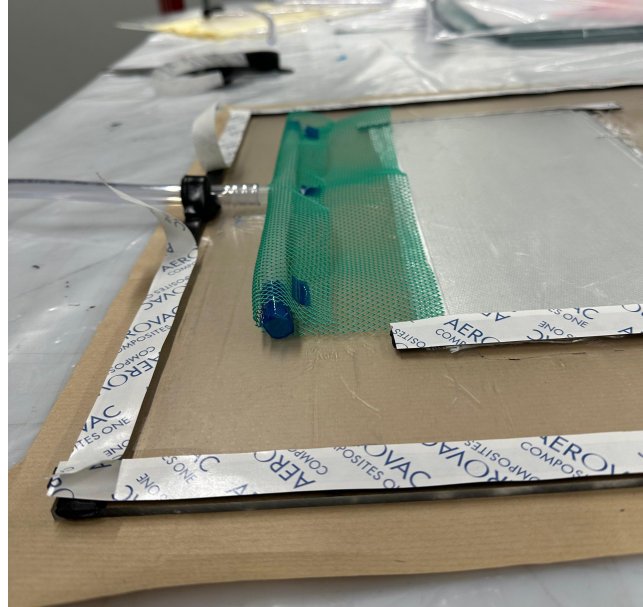


Figure A.2: Inlet tube assembly.

Afterward, place a sheet of breather fabric on the bottom side of the caul plate, overlapping the bottom edge of the glass fiber sheet. For the outlet tube, cut a piece of breather fabric into a trapezoid shape and place it with the short edge inside the flexible tube. Wrap this tube with three layers of tacky tape, similar to the inlet tube, and attach it to the bottom tacky tape of the larger plexiglass plate. The assembly at the end of phase 3 should resemble [Figure A.3](#).

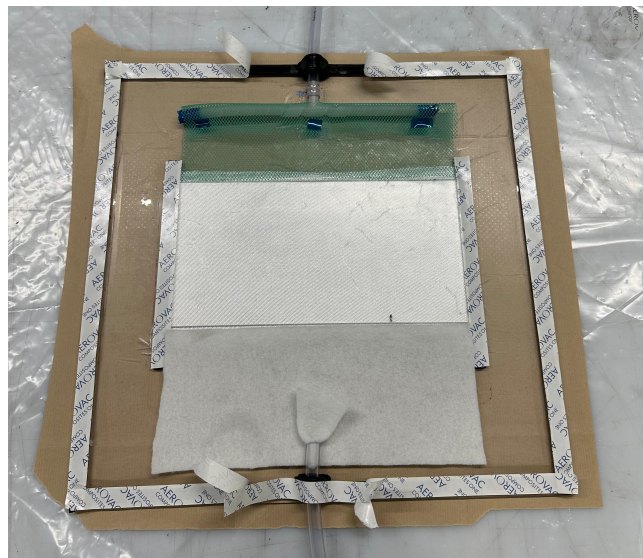


Figure A.3: Assembly with the outlet tube.

Next, place a sheet of perforated release film and a peel ply, covering almost the entire inner area surrounded by the tacky tape, except for the inlet tube assembly, as shown in [Figure A.4](#). This will

allow the assembly to be easily separated from the panel after curing.

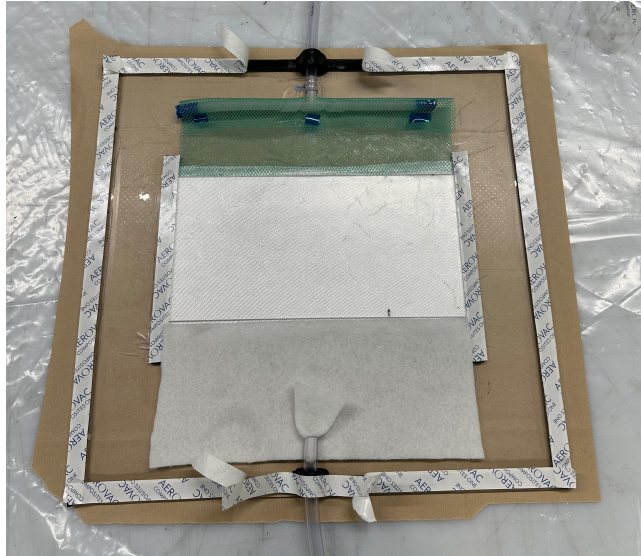
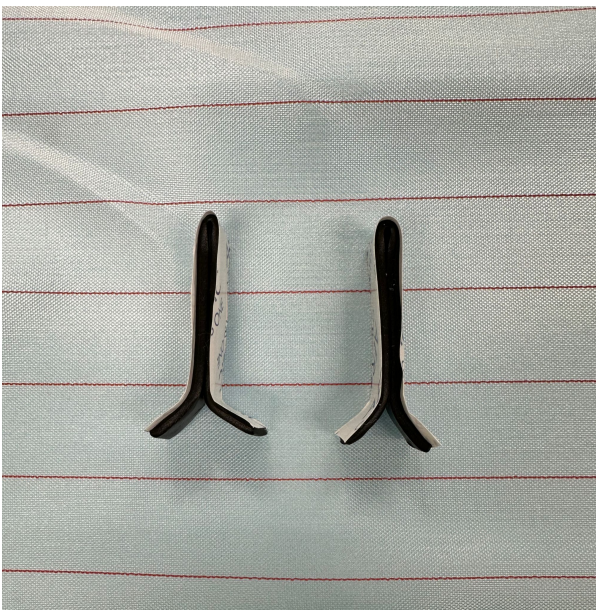


Figure A.4: Perforate flow mesh and peel ply covering the assembly.

Phase 4: Vacuum baging

In this phase, first cut a sheet of vacuum bag that is larger than the large plate in both length and width. Then, cut two pieces of tacky tape and fold each into a T-shape, as shown in [Figure A.5a](#). Place the T-shaped tacky tape next to the spiral tube on both side edges of the large plate. Next, place the vacuum bag on top and secure it to the tacky tape, ensuring that there are no gaps where air could enter. The easiest method is to start from the top edge of the large plate, followed by one of the side edges, then the bottom edge, and finally the other side edge. The assembly up to this point should resemble [Figure A.5b](#).



(a) T-shaped tacky tape.



(b) Final assembly before the leakage test.

Figure A.5: Phase 4 assembly

Phase 5: Leakage testing

Now that the assembly is ready, a leakage test is needed to ensure airtightness. For this purpose, wrap tacky tape around the end of a flexible piece of tubing and attach it to the vacuum pump. Then, turn on the vacuum pump and adjust the knob to draw maximum vacuum. After some time, the vacuum gauge should reach an equilibrium pressure.

Next, remove the test tube and connect the outlet tube of the assembly to the vacuum pump. Use a clamp to seal off the inlet of the assembly, making sure the clamp is positioned as close as possible to the end of the tube. This minimizes the amount of air trapped underneath the clamp, which could otherwise displace towards the glass fibers during the vacuum infusion process. Turn on the vacuum pump again.

If the vacuum gauge reaches the same equilibrium pressure as it did with the test tube, the leakage test is successful. If the test is not successful, ensure that the tacky tape under the vacuum bag is pressed down firmly or check for any punctures in the vacuum bag itself. The next step will be resin degassing and bucket preparation.

Phase 6: Resin degassing and bucket preparation

In this phase, the resin and hardener are mixed according to the manufacturer's specifications, which is a 3:1 weight ratio for Resin L and Hardener GL2 from R and G, respectively. The cup used for the resin/hardener mixture should be at least three times larger than its content to accommodate the degassing phase, as the mixture will start to bubble and rise. Mix the resin components together using a wooden stick for at least 2 minutes. Afterwards, place the bucket containing the mixture inside a vacuum pressure chamber to degas at 17 millibars for 30 minutes.

While the mixture is degassing, prepare the inlet and outlet tubes for the vacuum infusion process. Cut the end of the inlet tube at a slight angle and secure it to a wooden spatula using two pieces of blue adhesive tape, as shown in [Figure A.6](#). This prevents the end of the tube from making full contact with the bottom of the resin/hardener bucket during the infusion process, which could restrict the flow of resin.



Figure A.6: Preparation of the inlet tube.

After the degassing has completed, fill a bucket with water and place the bucket containing the resin

mixture on top of it. The bucket of water ensures that the mixture cools down in case of an exothermic reaction. Afterwards, place the inlet tube in the resin bucket and secure everything together using a clamp. The bucket assembly should resemble [Figure A.7](#).

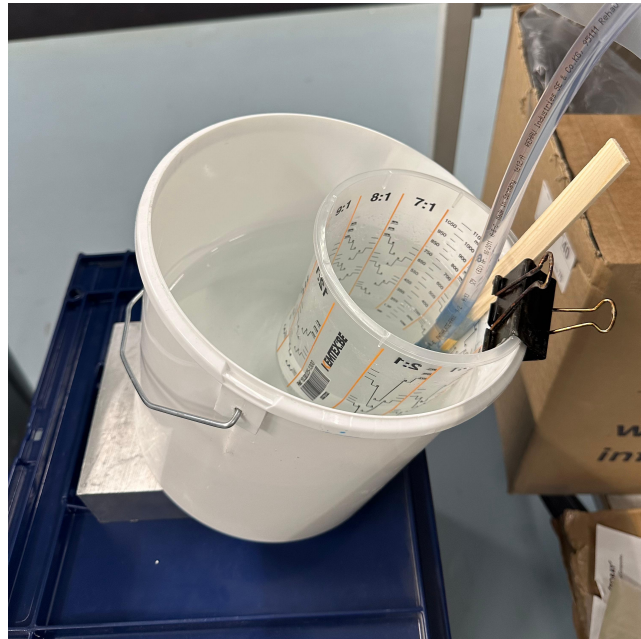


Figure A.7: Bucket assembly.

Phase 7: Vacuum infusion

The last phase is the infusion process of the glass fibers with the resin/hardener mixture. This is done by first setting the vacuum pressure to 50 mbar. If the pressure is too low, the resin will flow too fast, leading to entrapped air and dry fiber areas.

Afterwards, open the inlet clamp, from which the resin/hardener mixture will start flowing. When the resin fully reaches the inlet tube, wait until the resin has reached approximately 30 centimeters into the tube before closing the inlet tube using the clamp. This ensures that the air inside the vacuum bag has enough time to escape through the outlet tube, resulting in a fully infused composite panel without visible voids.

Finally, increase the pressure of the vacuum pump until the vacuum gauge indicates 500 mbar and let it cure for 24 hours at room temperature without turning off the vacuum pump. If MMA has been added, it is recommended to leave it to cure for 48 hours at room temperature. It has been observed that the addition of MMA increases the curing time of the resin. If the vacuum pressure is left at 50 mbar, the resin will be drawn out of the composite before gelation time, resulting in dry glass fiber areas where the resin has been drawn out.

Appendix B

Abbe Refractometer Sample Preparation and Measurement

This section provides the method for preparing samples and the measurement with the Abbe refractometer. The Abbe refractometer used is from Zeiss as seen in [Figure B.1](#), which can measure both liquid and solid materials with a refractive index between 1.3 and 1.7. Solid samples are limited to translucent and transparent materials such as plastic and glass. However, translucent samples may result in suboptimal measurements due to minimal light penetration.

The refractive indices are obtained using a monochromatic light source with a specific wavelength; in this case, a sodium lamp of 589 nm (yellow sodium spectral line). For solid samples, there is no need to ensure a constant temperature using a circulating water bath or to apply temperature correction factors, since temperature changes hardly affect the refractive indices.

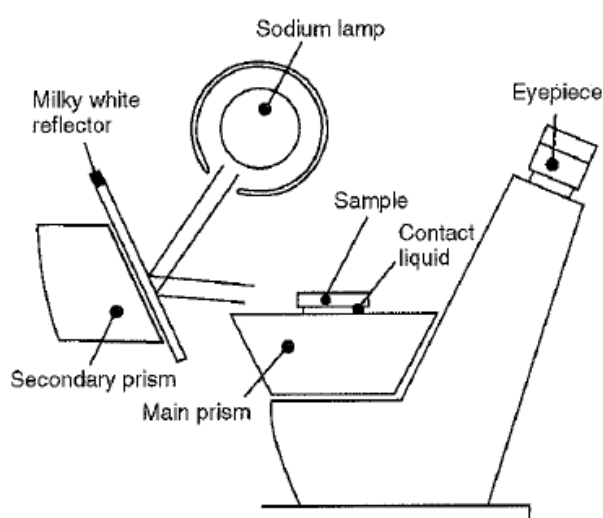


Figure 8-3

Figure B.1: Zeiss Abbe refractometer

B.1 Sample preparation

The main sample requirement for the Abbe refractometer is to have rectangular bodies with polished or shiny surfaces on the lighting side and the surface that is in contact with the measuring prism, as seen in [Figure B.2](#). In addition, the edge of the lighting side should be perpendicular to the contact surface. Lastly, the samples should have dimensions of approximately 30 x 20 x 3 mm (LxWxH), which have a smaller surface area compared to the main prism.

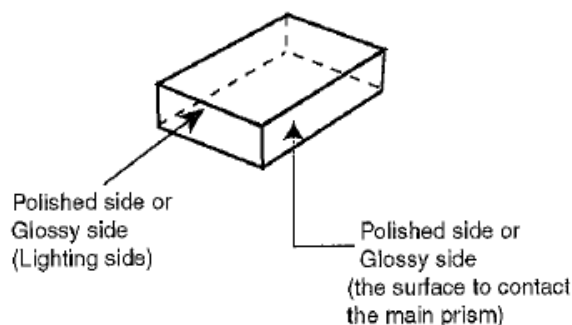


Figure B.2: Abbe refractometer sample requirements.

The fabrication of these samples can be divided into several steps. First, the desired dimensions and surface finish should be achieved. The chosen method to reach this goal is laser cutting plexiglass. Laser cutting of plexiglass ensures that multiple samples with consistent dimensions and shiny surfaces on all sides can be fabricated without requiring sanding or polishing. From these samples, a negative silicone mold can be made.

Once the silicone mold has been manufactured, the samples with the desired material compositions can be made. In this step, resin and hardener, along with different percentages of MMA, can be mixed, degassed for 30 minutes, and poured into the mold. After curing, the exposed surface of the sample may have an irregular surface. Sanding can be done to achieve a more homogeneous and perpendicular surface to the lighting side of the sample.

B.2 Measurement

The principle for measuring solid samples is based on reflected light. Compared to liquid samples, only the measurement prism is used for solid samples, while the upper illuminating prism is either swung upwards or left to the side. The first step of the measurement is to clean the surface of the main prism using ethanol.

For measuring solid samples, a contact liquid with a higher refractive index than the sample is required. Some commonly used contact liquids are listed in [Table B.1](#). Since it is expected that the cured resin samples have a refractive index between 1.54 and 1.60, monobromonaphthalene can be used as the contact liquid for the measurements.

Table B.1: Contact liquids and their respective refractive indices at 20°C.

Contact liquids	n_D^{20}
Methyl salicylate	1.53
Monobromoaphthalene	1.63
Methylene iodide	1.74
Methylene iodide with sulfur solution	1.74-1.78

Once the surface of the main prism has been cleaned, place a droplet of contact liquid in the center of the prism. Note that the contact surface of the samples should be free of burrs; otherwise, full contact between the sample surface and the prism will be obstructed. Applying very light pressure to the sample will ensure that the contact liquid spreads evenly across its contact surface.

Next, adjust the measurement knob until the contrast line aligns with the center of the cross as seen in the eyepiece. Once the measurement is complete, thoroughly clean the surface with ethanol. Contact liquids such as monobromonaphthalene are corrosive and may stain the prism surface if left for an extended period, potentially affecting the measurement accuracy of the equipment.

Appendix C

Tensile Testing Preparations

C.1 Materials and equipment

All required materials, equipment, and quantities can be seen below:

- Black permanent marker
- 120-grit sandpaper
- Plastic squeegee
- Small clamps
- FM 94 blue adhesive tape
- Loctite EA 3430 epoxy adhesive
- 100 μm glass beads
- Aluminum tabs (50 x 25 x 1 mm) (l x b x h)

First, the tensile test samples and the tabs are prepared by sanding down the contact surfaces using 180-grit sandpaper. For the tensile specimen, mark a line 5 cm away from the ends on both sides. Apply blue tape just before these surfaces to ensure that the untabbed region does not get scratched during sanding, as this will diminish the transparency of the samples.

To ensure adequate sanding of the surfaces, a pattern can be drawn on the sanding surfaces using a black permanent marker as seen in [Figure C.1](#). For the tabs, only one surface of each tab needs to be sanded down. This surface will be attached to the tensile specimen using adhesive. After proper sanding, this pattern should be gone. Then thoroughly wash, clean, and dry the surfaces to ensure no sanding particles remain.

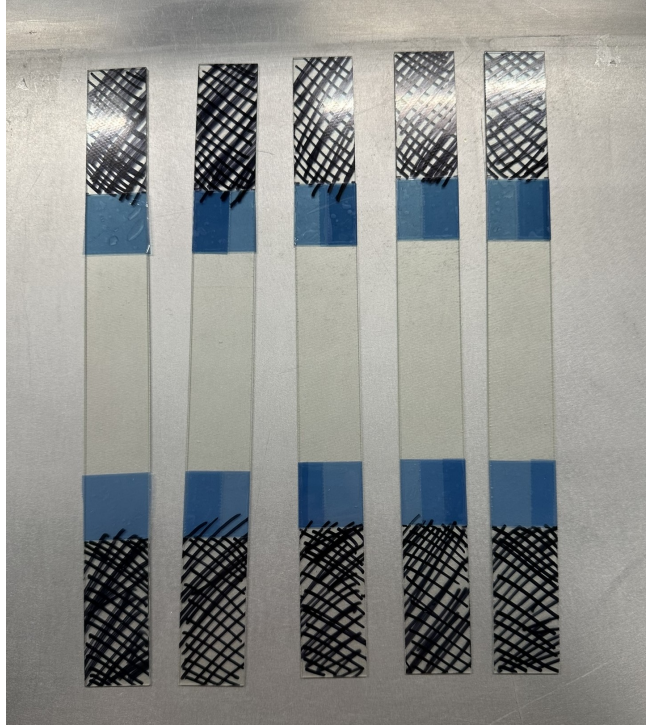


Figure C.1: Tensile test samples with tape and pattern before sanding.

Next, prepare the surfaces by cleaning them with isopropanol. After surface preparation, place the tabs on top of the samples and secure them using blue adhesive tape, ensuring that all surfaces and edges are fully in contact with the tape. This blue tape will aid in alignment during the adhesive application. The progress up to this point should resemble [Figure C.2](#).

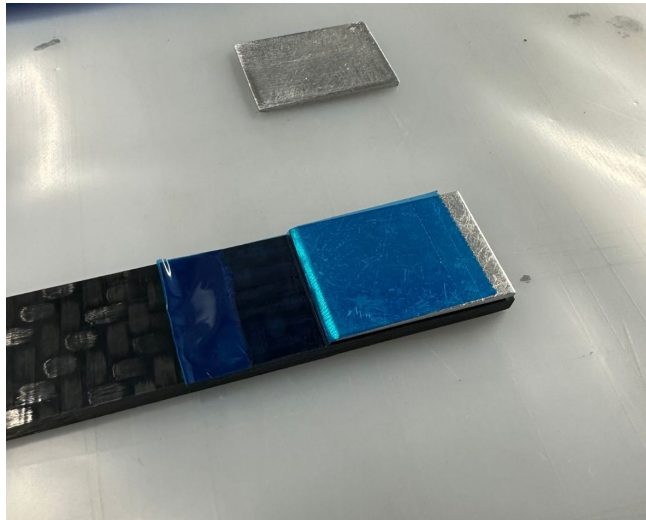
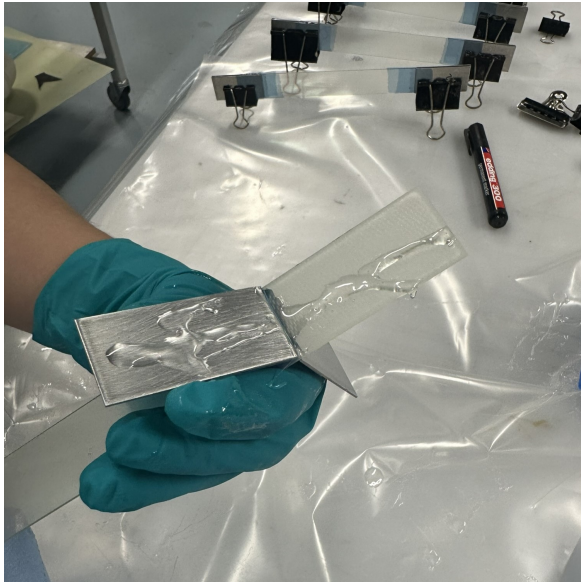
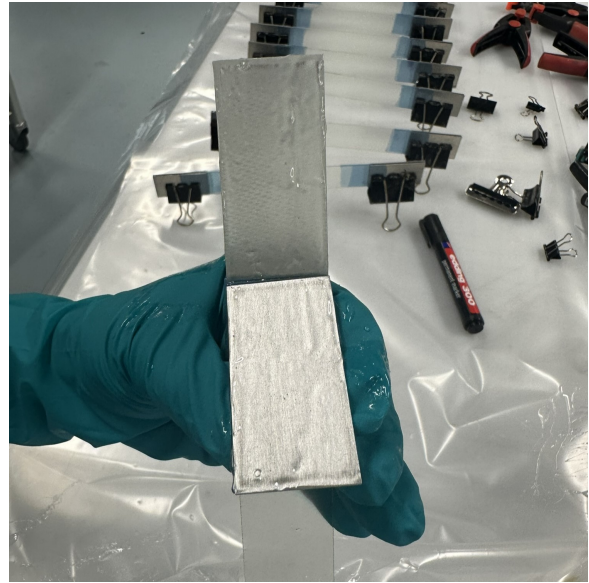


Figure C.2: Aluminum tabs secured to the test sample using blue adhesive tape.

To apply the adhesive, swing the tabs upwards and apply it to all surfaces. Then, spread the adhesive evenly using a plastic squeegee, as shown in [Figure C.3b](#). Before closing the tabs on the specimen, sprinkle a pinch of glass beads onto the adhesive surface. These glass beads help ensure a uniform adhesive thickness between the tab and the tensile specimen. Next, swing the tab back onto the surface of the tensile test specimen and apply pressure using clamps on each side. Finally, clean any excess epoxy resin from the sides of the specimen using the plastic squeegee.



(a) Applied adhesive.



(b) Adhesive spread out.

Figure C.3: Adhesive application on the tabbing material and the specimen.

Finally, the specimens should be left to cure for at least 24 hours, as shown in [Figure C.4](#). Curing the specimens at elevated temperatures can reduce the curing time and improve adhesive properties, but it may also reduce transparency. This is because the refractive index of the epoxy resin depends on the degree of cure, which is influenced by temperature.

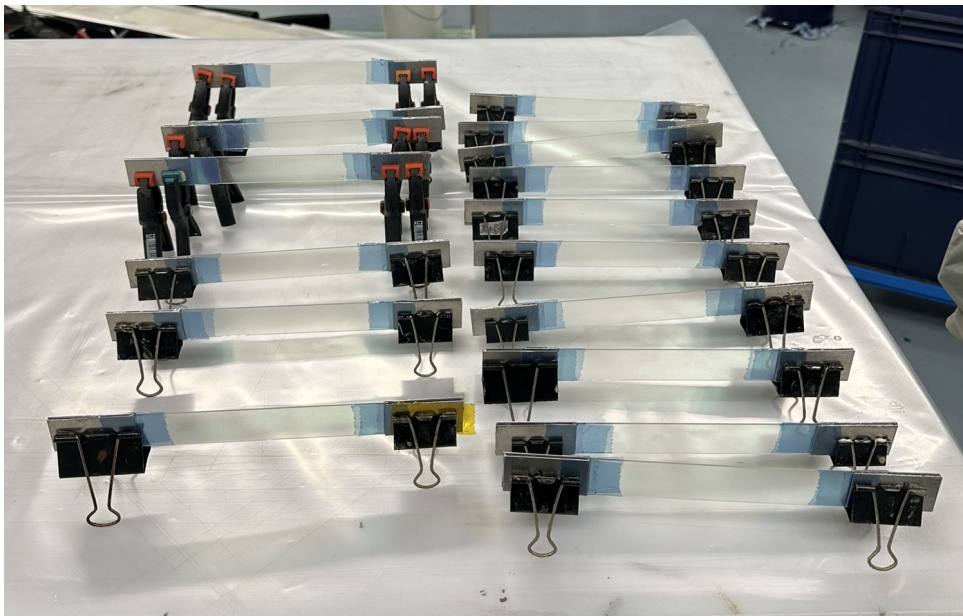


Figure C.4: Clamped specimens with aluminum tabbing material.

Appendix D

All Transmission Data

D.1 Transmission data - varying MMA percentages by weight (pure resin samples)

Light transmittance as a function of wavelength (MMA = 0%, N = 20)

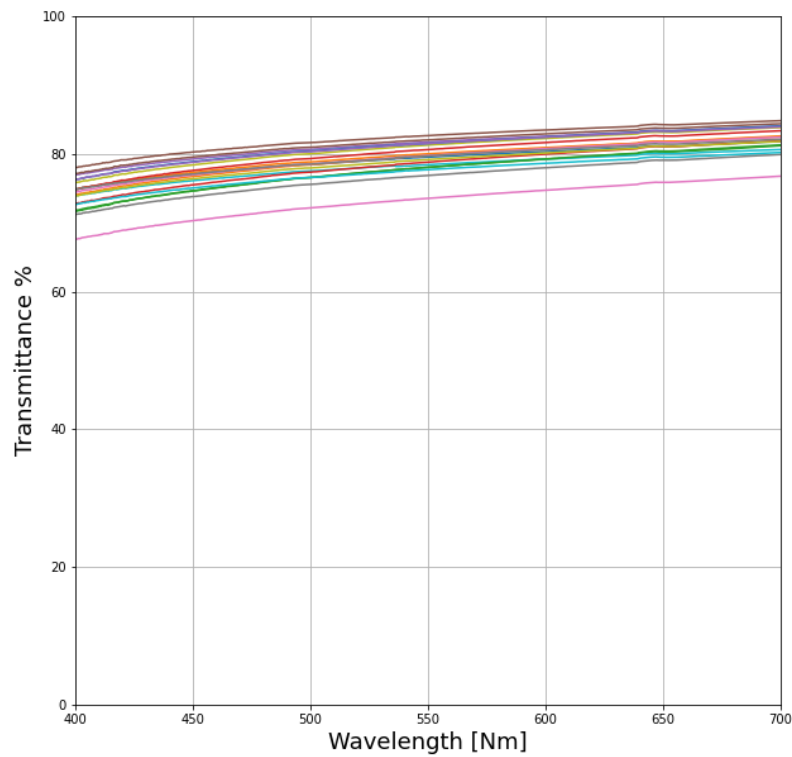


Figure D.1: Light transmittance curves for all 20 specimens with 0% MMA by weight.

Light transmittance as a function of wavelength (MMA = 1%, N = 20)

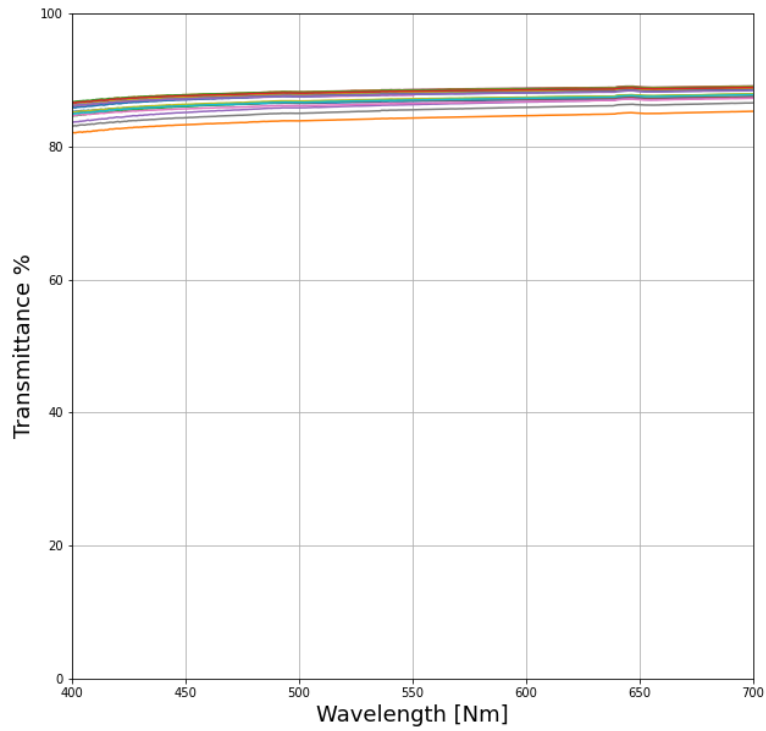


Figure D.2: Light transmittance curves for all 20 samples with 1% MMA by weight.

Light transmittance as a function of wavelength (MMA = 2.5%, N = 20)

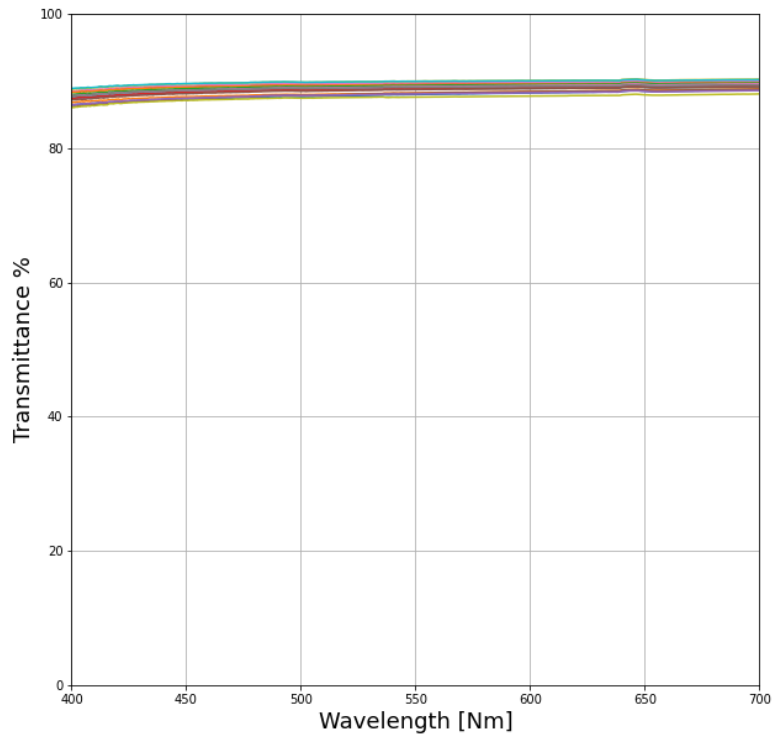


Figure D.3: Light transmittance curves for all 20 samples with 2.5% MMA by weight.

D.2 Transmission data - varying MMA percentages by weight (TGFRP samples)

Light transmittance as a function of wavelength (0% MMA, N = 38)

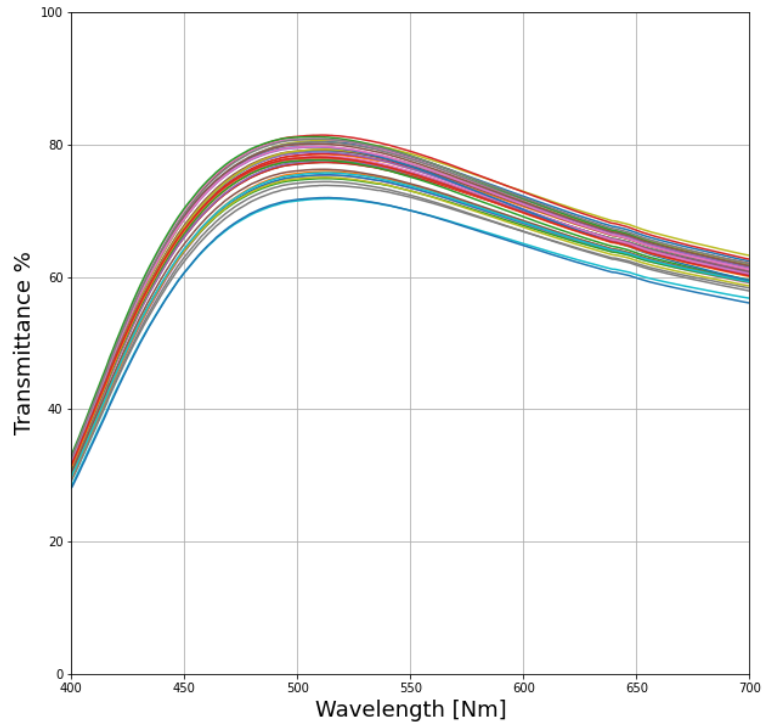


Figure D.4: Light transmittance curves for all 38 samples with 0% MMA by weight

Light transmittance as a function of wavelength (0.5% MMA, N = 40)

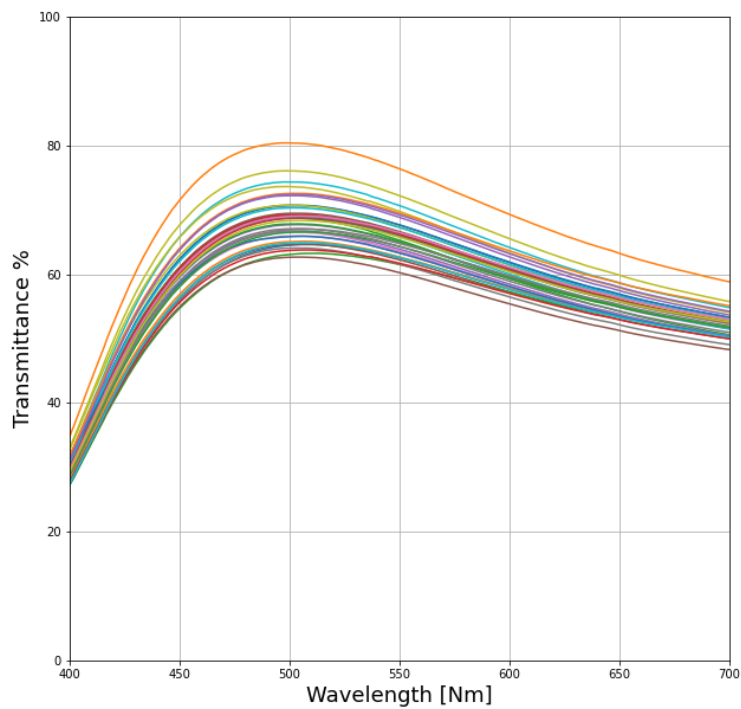


Figure D.5: Light transmittance curves for all 40 samples with 0.5% MMA by weight

Light transmittance as a function of wavelength (1% MMA, N = 40)

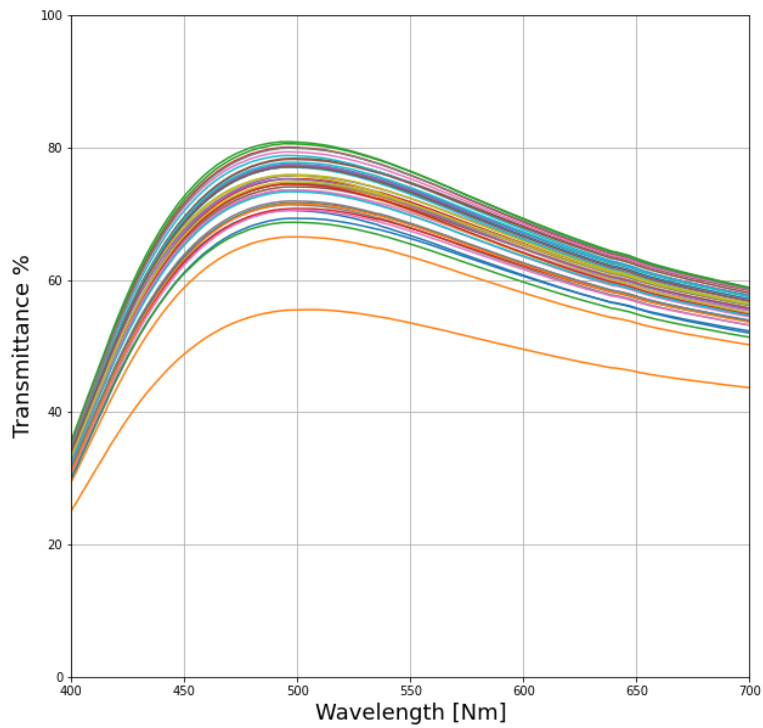


Figure D.6: Light transmittance curves for all 40 samples with 1% MMA by weight

Light transmittance as a function of wavelength (2.5% MMA, N = 36)

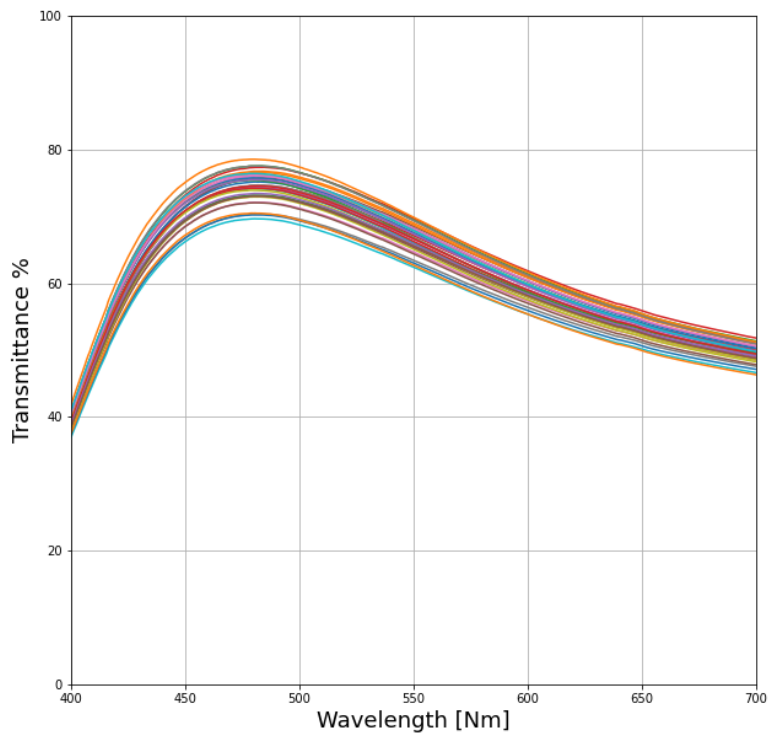


Figure D.7: Light transmittance curves for all 36 samples with 2.5% MMA by weight

D.3 Transmission data - layers

Light transmittance as a function of wavelength (5 layers, N = 38)

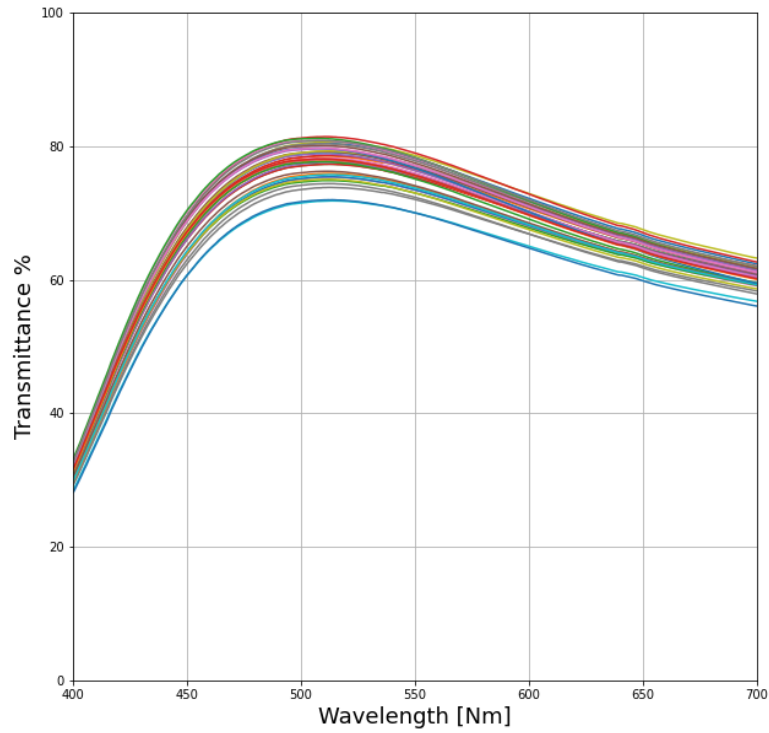


Figure D.8: Light transmittance curves for all 38 samples with 5 layers of glass fiber fabric.

Light transmittance as a function of wavelength (10 layers [0/90], N = 40)

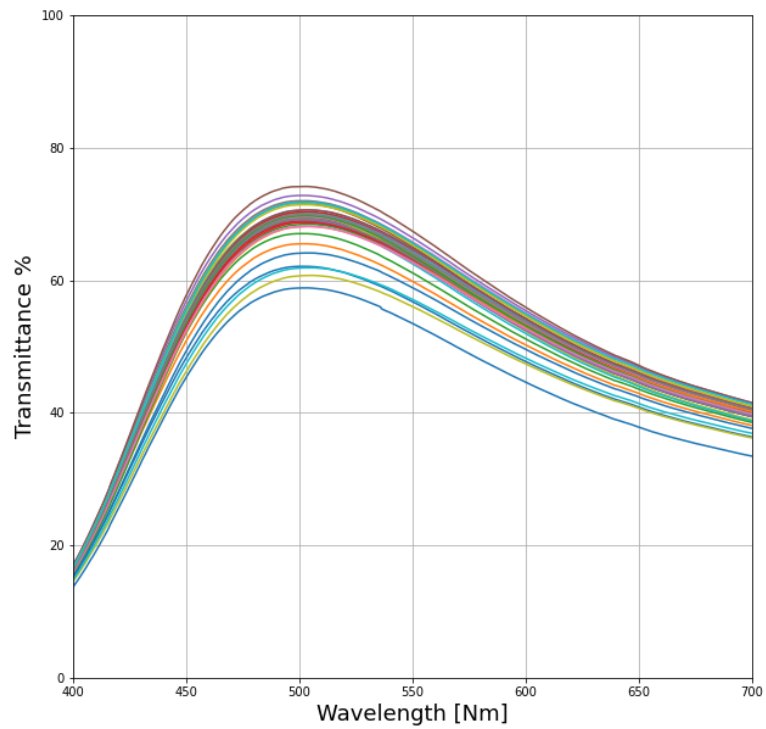


Figure D.9: Light transmittance curves for all 40 samples with 10 layers of glass fiber fabric.

Light transmittance as a function of wavelength (15 layers [0/90], N = 40)

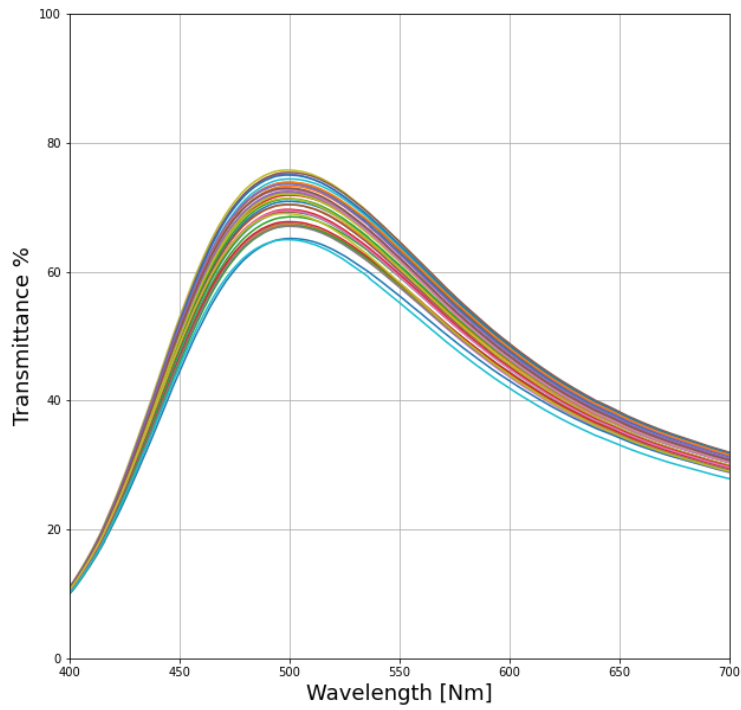


Figure D.10: Light transmittance curves for all 40 samples with 15 layers of glass fiber fabric.

D.4 Transmission data - post-curing

Light transmittance as a function of wavelength (No post curing, N = 38)

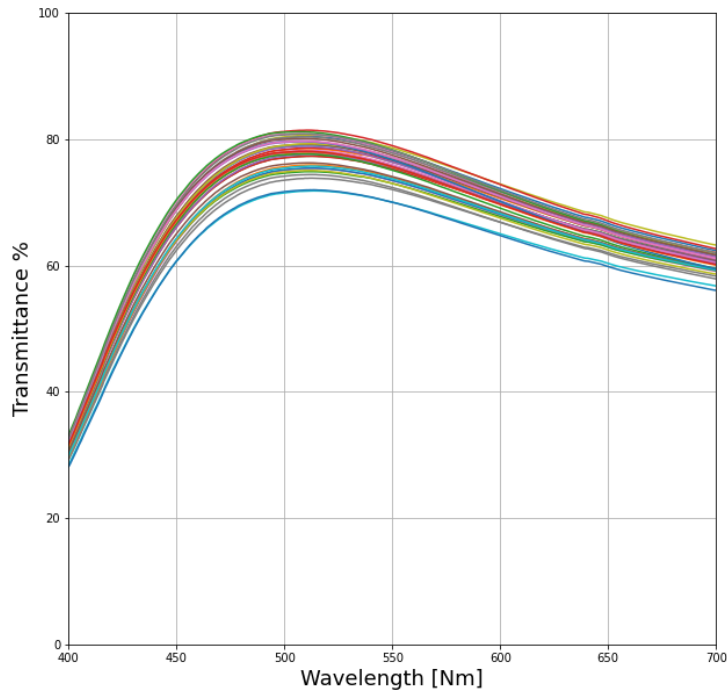


Figure D.11: Light transmittance curves for all 38 samples with no post-curing.

Light transmittance as a function of wavelength (Temperature = 40 °C, N = 24)

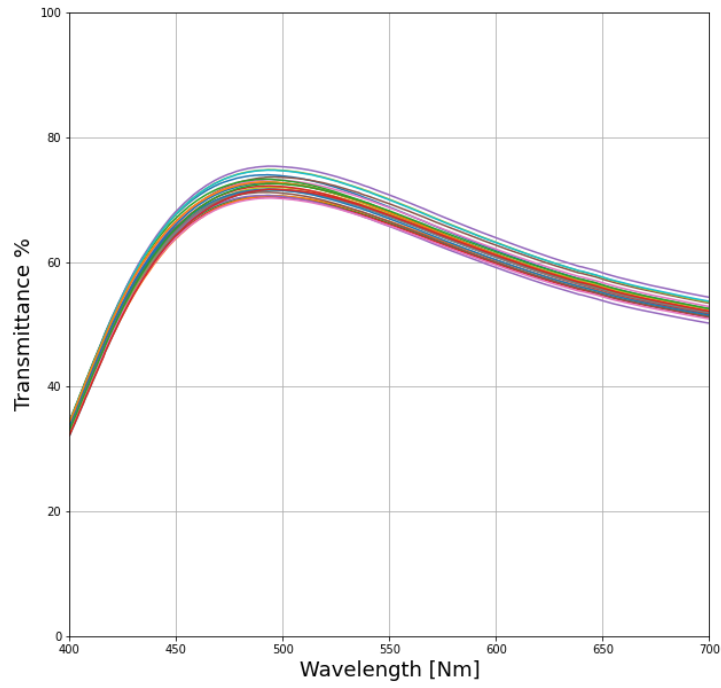


Figure D.12: Light transmittance curves for all 24 samples with post-curing at 40°C.

Light transmittance as a function of wavelength (Temperature = 60 °C, N = 24)

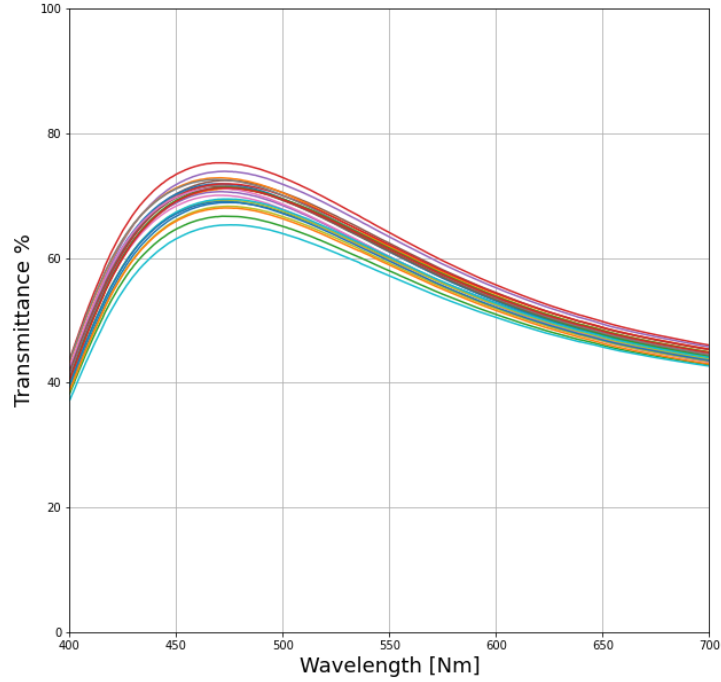


Figure D.13: Light transmittance curves for all 24 samples with post-curing at 60°C.

D.5 Transmission data - crack density

Light transmittance as a function of wavelength (5 layers, N = 12)

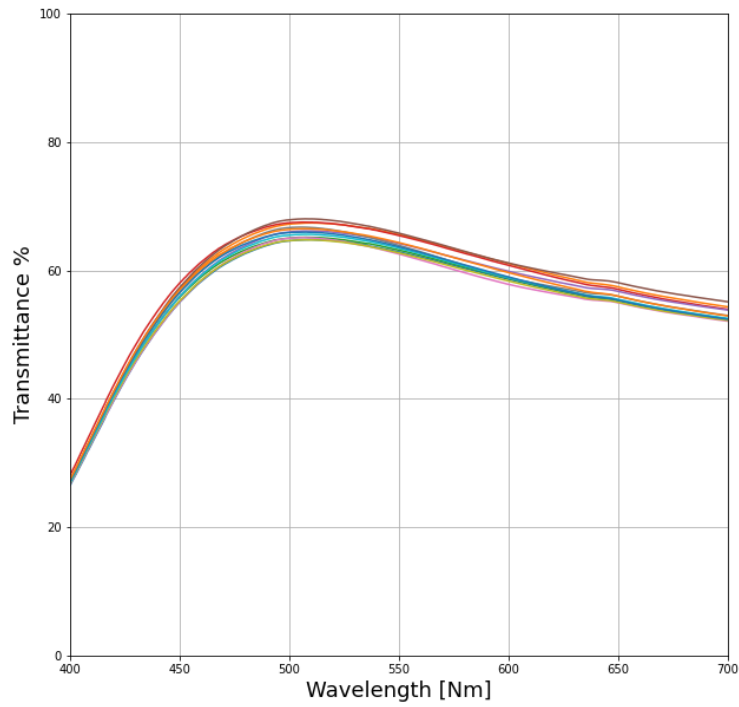


Figure D.14: Light transmittance curves for all 12 samples tensile tested at 60% of the ultimate tensile strength.

Light transmittance as a function of wavelength (5 layers, N = 12)

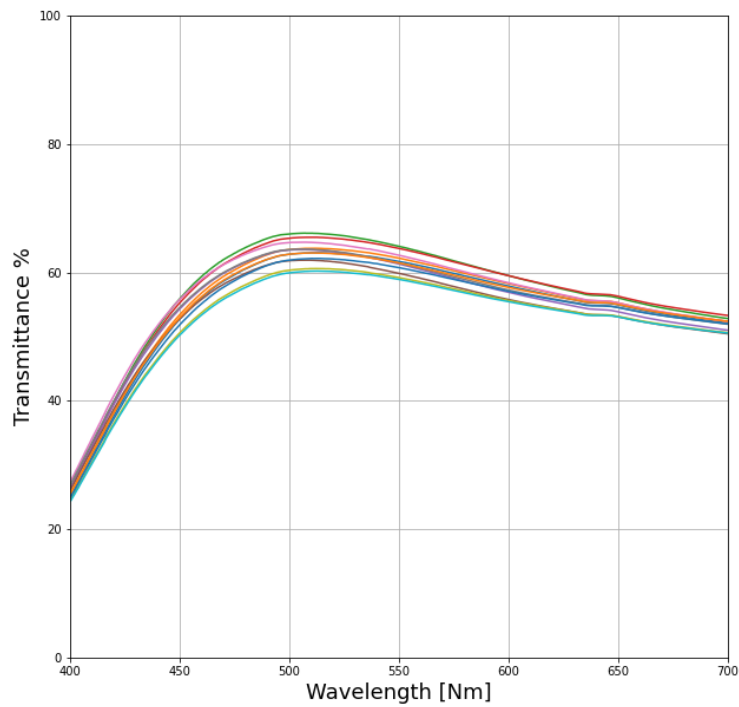


Figure D.15: Light transmittance curves for all 12 samples tensile tested at 70% of the ultimate tensile strength.

Light transmittance as a function of wavelength (5 layers, N = 12)

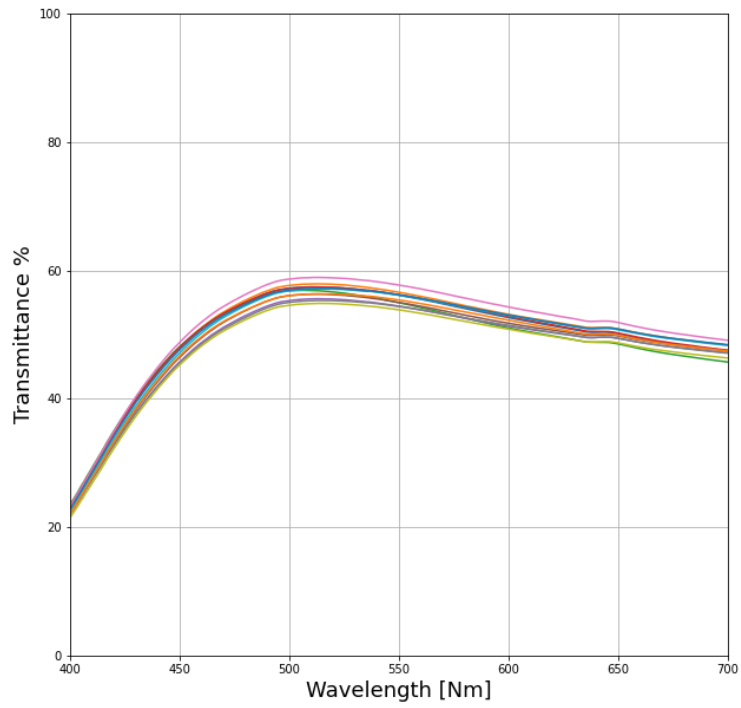


Figure D.16: Light transmittance curves for all 12 samples tensile tested at 80% of the ultimate tensile strength.